LOW NOISE, NARROW OPTICAL LINEWIDTH SEMICONDUCTOR-BASED OPTICAL COMB SOURCE AND LOW NOISE RF SIGNAL GENERATION

by

IBRAHIM TUNA OZDUR
M.S. University of Central Florida, 2008
B.S. Middle East Technical University,2002

A dissertation submitted in partial fulfillment of the requirements
for the degree of Doctor of Philosophy
in CREOL, The College of Optics and Photonics
at the University of Central Florida
Orlando, Florida

Spring Term
2011

Major Professor: Peter J. Delfyett, Jr.

©2011 Ibrahim T. Ozdur

ABSTRACT

Recently optical frequency combs and low noise RF tones are drawing increased attention due to applications in spectroscopy, metrology, arbitrary waveform generation, optical signal processing etc. This thesis focuses on the generation of low noise RF tones and stabilized optical frequency combs. The optical frequency combs are generated by a semiconductor based external cavity mode-locked laser with a high finesse intracavity etalon. In order to get the lowest noise and broadest bandwidth from the mode-locked laser, it is critical to know the free spectral range (FSR) of the etalon precisely. First the etalon FSR is measured by using the modified Pound-Drever-Hall (PDH) based method and obtained a resolution of 1 part in 10^6, which is 2 order of magnitude better than the standard PDH based method. After optimizing the cavity length, RF driving frequency and PDH cavity locking point, the mode-locked laser had an integrated timing jitter of 3 fs (1 Hz- 100 MHz) which is, to the best of our knowledge, the lowest jitter ever reported from a semiconductor based multigigahertz comb source. The mode-locked laser produces ~ 100 comb lines with 10 GHz spacing, a linewidth of ~500 Hz and 75 dB optical signal-to-noise ratio. The same system can also be driven as a regeneratively mode-locked laser with greatly improved noise performance.

Another way of generating a low noise RF tone is using an opto-electronic oscillator which uses an optical cavity as a high Q element. Due to the harmonic nature of OEOs, a mode selection element is necessary. Standard OEOs use an RF filter having drawbacks such as broad pass band, high loss, and high thermal noise. In our work, a novel optoelectronic scheme which uses an optical filter (Fabry-Perot etalon) as the mode filter instead of an RF filter is demonstrated. This method has the advantage of having ultra-narrow filtering bandwidths (~ 10

kHz for a 10 GHz FSR and 10^6 finesse) and an extremely low noise RF signal. Experimental demonstration of the proposed method resulted in a 5-10 dB decrease of the OEO noise compared to the conventional OEO setup. Also, by modifying the etalon-based OEO, and using single side band modulation, an optically tunable optoelectronic oscillator is achieved with 10-20 dB lower noise than dual side band modulation. Noise properties of the OEO as a function of optical frequency detuning is also analyzed theoretically and the results are in agreement with experimental results.

The thesis concludes with comments on future work and directions.

ACKNOWLEDGMENTS

First and foremost I want to thank to my advisor Dr. Peter Delfyett. It has been an honor to be his PhD student. I appreciate all his contributions of time, ideas and support. The joy and enthusiasm he has for research was contagious and motivational for me. I am also thankful for him being an excellent example of a successful professor.

I would also like to thank to the Ultrafast Photonics Group members Dr. Sarper Ozharar, Dr. Franklyn Quinlan, Dr. Sangyun Gee, Dr. Wangkuen Lee, Dr. Mehmetcan Akbulut, Dr. Shinwook Lee, Dr. Ji-Myoung Kim, Mohammad Umar Piracha, Dimitrios Mandridis, Charles Williams, Sharad Bhooplapur, Abhijeet Ardey, Dat Nguyen, Nazanin Hoghooghi, Josue Davila-Rodriguez, Marcus Bagnell, Edris Sarailou and Anthony Klee for their help and support during my graduate studies.

LIST OF ACRONYMS/ABBREVIATIONS

ADC	Analog-to-Digital Conversion
AM	Amplitude Modulation
A	Ampere
BW	Band Width
Cir	Circulator
COEO	Coupled Opto-Electronic Oscillator
CW	Continuous Wave
dB	Decibel
dBm	The power ratio in decibels (dB) of the measured power referenced to one milliwatt (mW)
dBc	Decibels relative to the carrier
DER	Dynamic Extinction Ratio
DFB	Distributed Feedback
EDFA	Erbium-Doped Fiber Amplifier
EOM	Electro-Optic Modulator
Eq.	Equation
FSR	Free Spectral Range
Fig.	Figure

FSC	Free Space Coupler
f_{osc}	Oscillation Frequency
fs	femtosecond
FWHM	Full Width at Half Maximum
GHz	Giga-Hertz
HEM	High Extinction Modulator
Hz	Hertz
IM	Intensity Modulator
kHz	kilo-Hertz
K	Kelvin
LPF	Low Pass Filter
MLL	Mode-Locked Laser
MHz	Mega-Hertz
Mix	Mixer
N	Integer
OEO	Opto-electronic Oscillator
OSNR	Optical Signal-to-Noise Ratio
OPS	Optical Phase Shifter
OSA	Optical Spectrum Analyzer
PDH	Pound-Drever-Hall
PD	Photo Detector

PSD	Power Spectral Density
PM	Phase Modulation
PZT	Piezo-electric Transducer
PSK	Phase-Shift Keying
PC	Polarization Controller
ppb	part per billion
PID	Proportional–Integral–Derivative
PS	Phase Shifter
PBS	Polarization Beam Splitter
QAM	Quadrature Amplitude Modulation
RF	Radio Frequency
RF Osc.	RF Oscillator
RFSA	Radio Frequency Spectrum Analyzer
RT-RFSA	Real Time – Radio Frequency Spectrum Analyzer
SG	Signal Generator
SOA	Semiconductor Optical Amplifier
SNR	Signal-to-Noise Ratio
SSB	Single Sideband
τ	Cavity total round trip time
ULE	Ultra-Low Expansion
V	Voltage

VOD	Variable Optical Delay
W	Watt
WDM	Wavelength Division Multiplexing
WPE	Wall-Plug Efficiency

TABLE OF CONTENTS

LIST OF FIGURES

CHAPTER 1: INTRODUCTION

Optical frequency combs and low noise RF tone generation have drawn considerable attention for applications in high speed photonic analog to digital conversion [1-2], arbitrary electrical waveform generation[3], optical arbitrary waveform generation[4] and coherent communication[5]. Optical frequency combs can be generated by various methods including direct modulation of CW light [6-7], using a monolithic microresonator [8] and from a mode-locked laser [9-10]. This work mainly focuses on the generation of optical comb lines from mode-locked lasers.

Optical frequency combs generated from a mode-locked laser can be represented as in Fig. 1.

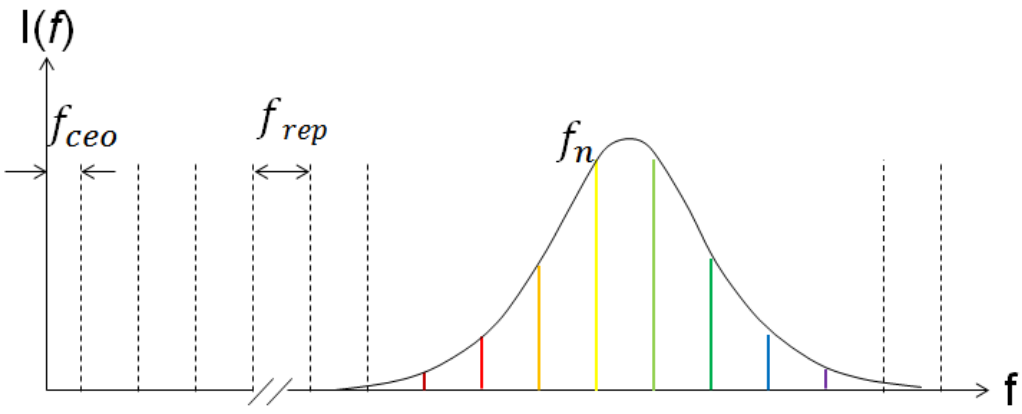

Figure 1: Optical frequency combs from a mode-locked laser.

Any optical comb line frequency can be expressed as:

$$f_n = f_{ceo} + (n-1)f_{rep} \quad (1)$$

Where, f_{ceo} is the carrier envelope offset frequency, f_{rep} is the repetition rate of the laser and n is the mode number.

One of the frequency domain applications of optical frequency comb is optical arbitrary waveform generation (OAWG). The ability to generate phase locked optical comb makes mode-locked lasers an excellent source for optical arbitrary waveform generation. An example of OAWG is shown in Fig. 2. The wavelength division multiplexing filter separates different comb lines. The separated optical comb lines can be amplitude and phase modulated independently and then recombined again to create an optical arbitrary waveform. The WDM filter requires a high optical frequency stability of the comb lines to match the comb lines with the peak of the filter which a mode-locked laser can provide easily.

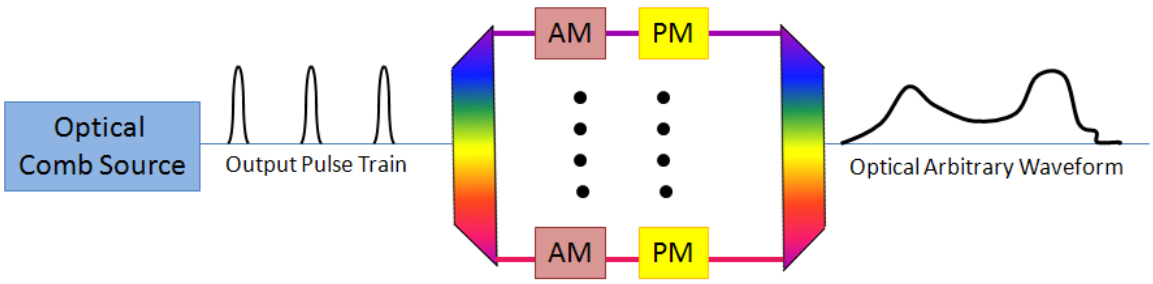

Figure 2: An example of a frequency domain application. AM, amplitude modulator; PM, phase modulator.

Another example of phase locked comb lines is from astronomical measurements. A multi-gigahertz separated comb lines are used to calibrate the spectrographs and this can lead to radial velocity measurements with <1 cm/s precision [11].

One of the time domain applications of mode locked lasers is high speed analog to digital conversion. Fig. 3 shows a representation of photonic analog to digital conversion (ADC) [2].

The photonic high speed ADC uses a time demultiplexer to separate the subsequent pulses of the optical pulse train into different channels. By using a lower bandwidth photodetector and electronics the signal is analyzed and then combined. The overall performance of a ADC system rely on the master clock performance which is the mode-locked laser, for example 10 gigasample/sec ADC requires a pulse train with an rms timing jitter of 30 fs and amplitude noise under 0.049% to achieve 10 bits of resolution.

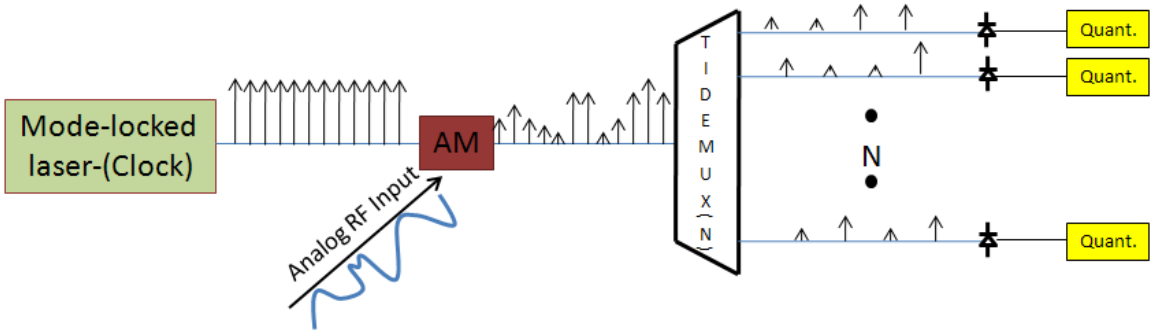

Figure 3: Representation of photonic analog to digital conversion. AM. Amplitude modulator.

There are different methods for optical frequency stabilization of the mode-locked lasers. One approach is the self-referencing technique [12] that requires an octave spanning optical bandwith, which is difficult to obtain at high repetition rates. Another method is to stabilize the optical comb lines is to an intracavity etalon [13]. In this technique the optical frequency is stabilized reference to the resonance of a Fabry-Perot etalon.

Semiconductor lasers can be fundamentally mode-locked at multi-gigahertz repetition rates [14]. However, because of the short cavity length, these lasers have a very broad linewidth. In order to decrease the linewidth of the mode-locked laser long cavities are necessary.

In order to maintain the high repetition rate with a longer cavity, harmonic mode-locking is necessary. In active mode-locking, the modulation frequency is not equal to the laser cavity

fundamental frequency (f_c) but it's an integer multiple of it ($N*f_c$). When the laser is mode-locked at the N^{th} harmonic, there are N different independent pulses inside the cavity, Fig.4. Each pulse has its own interleaved phase locked optical spectrum, or super-modes, with optical comb separation of $N*f_c$. The simultaneous lasing of independent optical super-modes causes random fluctuations in timing and amplitude of the pulse train. This noise is called super-mode noise in timing jitter and pulse to pulse amplitude noise. The noise spurs occur at the multiples of the cavity fundamental.

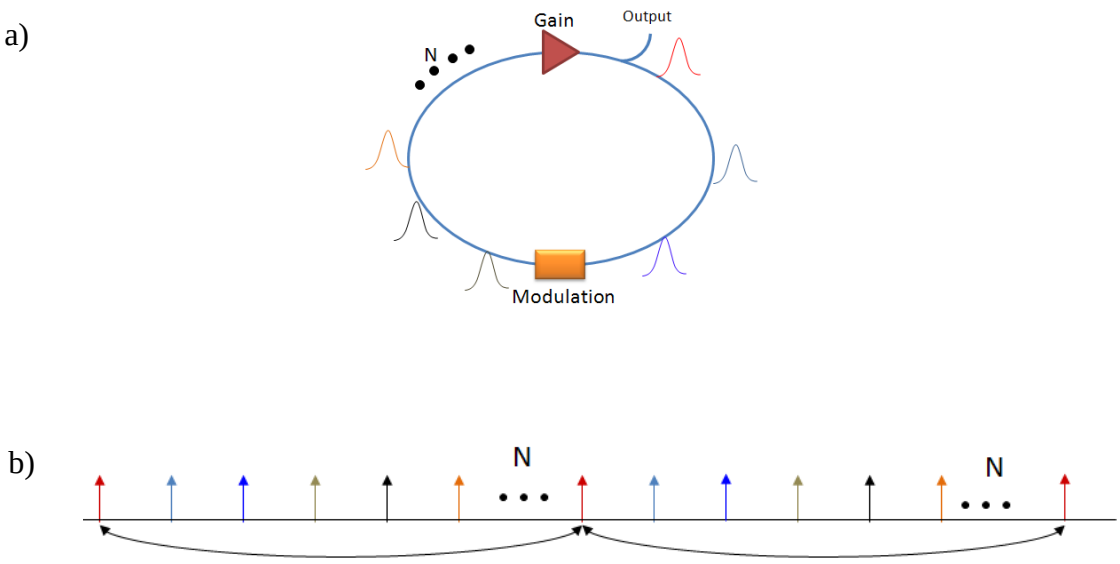

Figure 4: Harmonic mode-locking in time (a) and frequency (b) domain. The time domain picture shows multiple pulses in the cavity, and the frequency domain picture shows interleaved super-mode sets of phase locked frequencies.

There are different methods to suppress the supermode-noise. One of them is injecting a narrow linewidth laser in to the cavity [15]. In this method a CW laser light is injected in to the cavity. The supermode group created by the narrow linewidth injected light becomes dominant and suppresses the other supermode groups. Another method to suppress the super-mode noise is to use an intracavity etalon. The etalon inside a laser cavity removes all but one optical super-mode by the periodic filtering thereby eliminating the super-mode noise and lowering the timing jitter (Fig. 5).

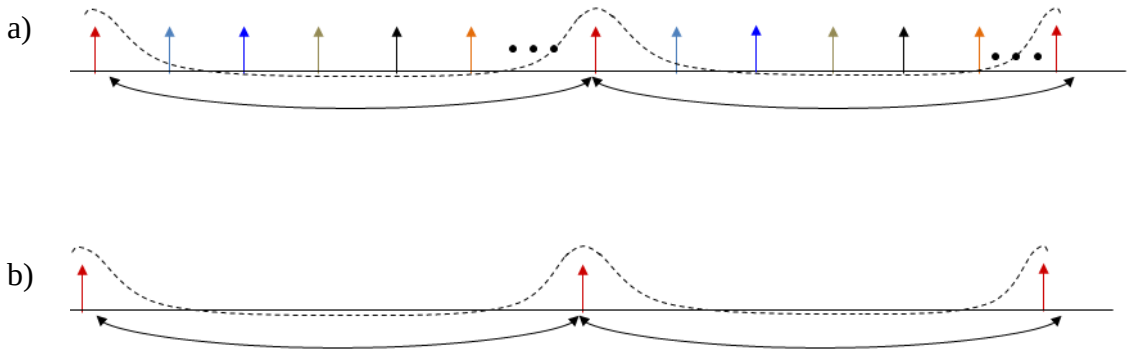

Figure 5: The periodic filtering of the Fabry-Perot etalon eliminates all but one longitudinal phase locked mode set.

By using an etalon inside a cavity, one can get a long cavity length and hence narrow linewidth while maintaining the high repetition rate. However, the width of the etalon transmission window limits the length of the laser cavity. If the cavity is too long, then more than one supermode set will fit inside the transmission window and hence the elimination cannot be done. One way to increase the cavity length is simply to use an etalon with a narrower transmission

peak or higher finesse. The performance of a actively mode locked laser with a 100-finesse etalon was shown [16,17]. The pulse-to-pulse timing jitter and amplitude noise measurements can be performed by examining the RF phase and amplitude noise sidebands of the photodetected carrier tone at the laser repetition rate frequency[18]. The timing jitter can be calculated from the phase noise sidebands by:

$$\sigma_J = \frac{1}{2\pi f_{ML}} \sqrt{2\int L(f)df} \tag{2}$$

where σ_J is the root-mean-squared jitter, f_{ML} is the laser repetition rate and $L(f)$ is the relative power of the phase noise side band in one Hertz bandwidth to the carrier power. In order to obtain the total root-mean-squared jitter, the upper limit of the integral should be one-half of the repetition rate (Nyquist frequency). For a laser with multi-gigahertz repetition rate, it is difficult to measure the jitter up to Nyquist frequency with the commercially available equipment. Thus instead, assumptions about the noise spectrum and extrapolations are made [19].

The pulse-to-pulse amplitude fluctuations can be calculated from the amplitude noise sidebands as [18]

$$\frac{\Delta E}{E} = \sqrt{2\int M(f)df} \tag{3}$$

where $\Delta E/E$ is the fractional of the pulse amplitude and $M(f)$ is the power the relative power of the amplitude noise side band in one Hertz bandwidth to the carrier power.

CHAPTER 2: HIGH PRECISION FREE SPECTRAL RANGE MEASUREMENT OF A FABRY-PEROT ETALON

Introduction

When an etalon inserted to the laser cavity it's critical to know the free spectral range (FSR) of the etalon because the laser will be driven by the FSR frequency. Any mismatch between the FSR, synthesizer frequency and laser mode spacing will result in a poor mode-locking and narrower optical bandwidth.

Most of the reported methods for measuring the FSR of an etalon are based on mapping out the etalon transmission peaks with an optical spectrum analyzer [20-22]. However because of the limited resolution of an optical spectrum analyzer (OSA), the precision of these methods is reduced when the FSR is relatively small. In order to measure the FSR precisely without relying on the limited resolution of an OSA, a method based on the Pound-Drever-Hall (PDH) technique [23] was introduced with a precision 1 part in 10^4 [24]. The precision of this technique was limited by an unwanted static modulation of the background signal which reduces the signal to noise ratio.

In this work, we eliminate this static modulation by introducing an additional dynamic (time varying) modulation followed by time averaging to the measurement setup resulting in the elimination of the unwanted background component in the error signal. The increase in the signal-to-noise ratio leads to an improvement in the precision of the FSR measurement by 2 orders of magnitude. The FSR of a ~10GHz etalon with 100 finesse was measured with 10 kHz precision which represents 1 part in 10^6 precision.

Experiments and Results:

The measurement technique relies on the PDH frequency stabilization error signal. The modified set-up of the PDH scheme for the FSR measurement is shown in Fig. 6.

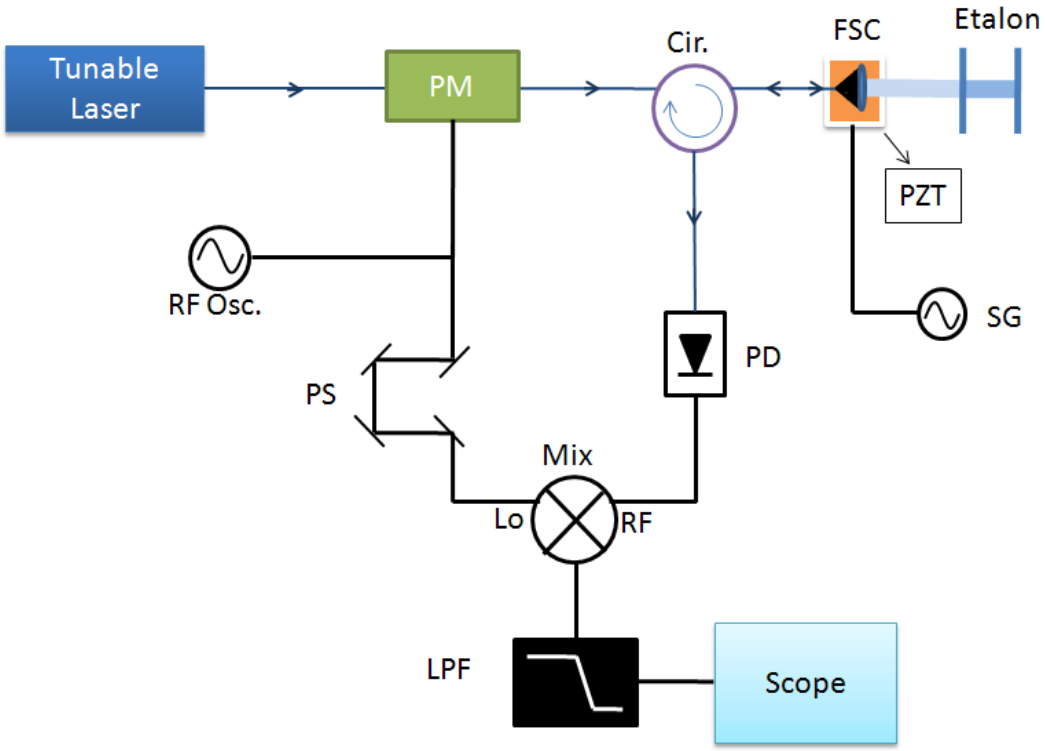

Figure 6: Modified setup of PDH error signal (RF Osc: RF Oscillator, PM: Phase Modulator, PS: Phase Shifter, Cir: Circulator, FSC: Free Space Coupler, PZT: Piezoelectric transducer SG: Signal Generator, PD: Photo detector, Mix: Mixer, LPF: Low Pass Filter).

The PDH error signal amplitude after the low pass filter (LPF) is given by:

$$V_{mix}(\upsilon) = V_o \,\mathrm{Re}\left\{\left[r(\upsilon)r^*(\upsilon+\Omega) - r^*(\upsilon)r(\upsilon-\Omega)\right]e^{i\Delta\phi}\right\} \qquad (4)$$

where, υ is the optical frequency, Ω is the phase modulation frequency, $V_o = I\beta\eta RM/2$ (I is the injected optical power, β is the modulation depth, η is the photo detector efficiency, R is the

impedance (50 ohm), *M* is the mixer conversion gain,), $\Delta\Phi$ is the phase difference between mixer LO and RF inputs and $r(\upsilon)$ is the is the etalon reflectivity which is given by:

$$r(\upsilon) = \frac{r(\exp(i2\pi\upsilon/f_{FSR}) - 1)}{1 - r^2\exp(i2\pi\upsilon/f_{FSR})} \tag{5}$$

where *r* is the mirror reflectivity and f_{FSR} is the FSR.

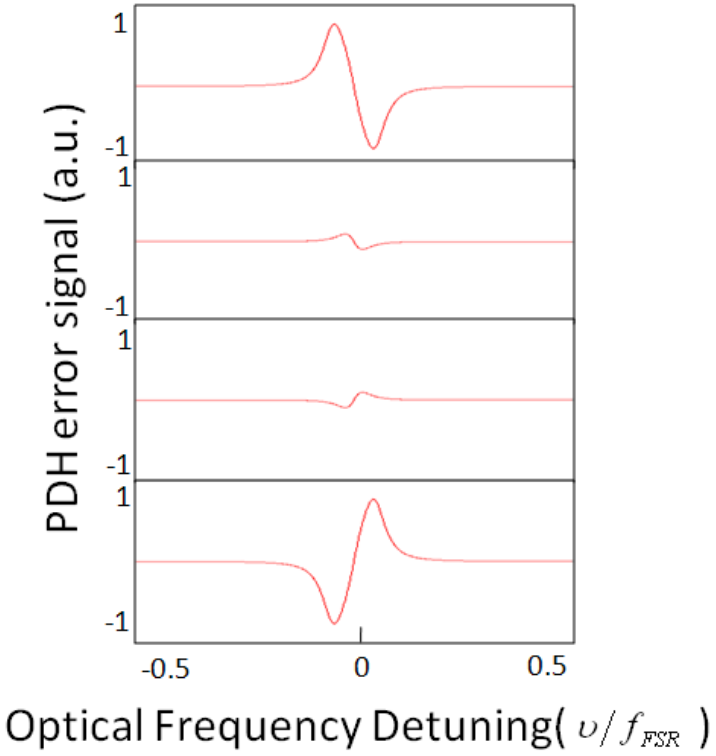

Figure 7: Simulation of error signal with frequencies: 0.95.0.995,1.005,and 1.05 of υ/f_{FSR} from top to bottom for $\Delta\phi = 0$.

The simulation of the signal at different modulation frequencies, when $\Delta\Phi$=0 is shown in Fig. 7. Note that this phase difference is different from the normal 90^o phase for conventional PDH locking schemes, and serves as the basis for this technique [24]. In this case, the PDH error

signal becomes very weak as Ω approaches the f_{FSR}, but the sign of the signal changes as Ω is tuned across the etalon resonance. In our improved technique, this property is used to measure the FSR precisely.

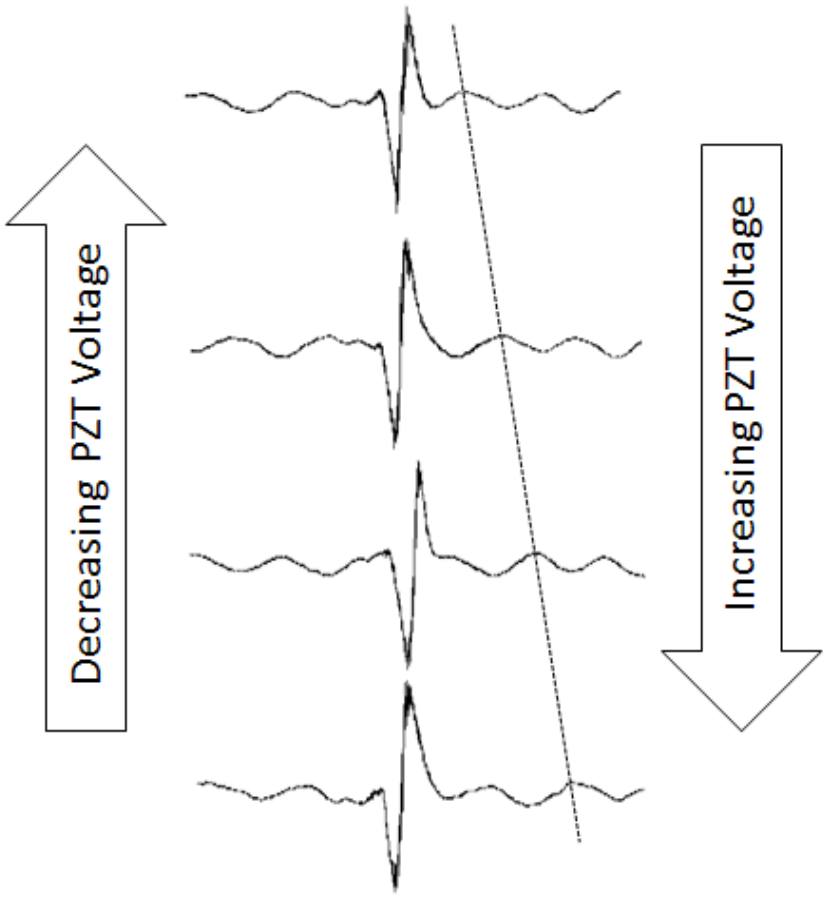

Figure 8: The shift of ripples as a function of distance between the fiber coupler and etalon. Note that the error signal is stationary.

Experimental results shown in Fig. 8 display a static modulation (not present in the simulated results), which limit the measurement precision. An important characteristic of this signal is that, as the distance between the fiber free space coupler and etalon changes, the static modulation

shifts but the PDH error signal remains fixed. Fig. 8 shows the shifts of the static modulation when the distance between the free space coupler and etalon changes slightly. In order to change the distance between the free space coupler and etalon, a piezoelectric transducer (PZT) is placed under the free space coupler. Modulation of the voltage applied to the PZT by a sine wave results in a periodic displacement of the static modulation rapidly. During data acquisition, the error signal can then be electronically time averaged. As this modulation has a sinusoidal shape and is dynamically changed, after averaging the modulation is eliminated but the error signal remains unchanged. In Fig. 9, the signal is shown with the previous PDH based measurement technique and in Fig. 10 with the modified PDH based technique.

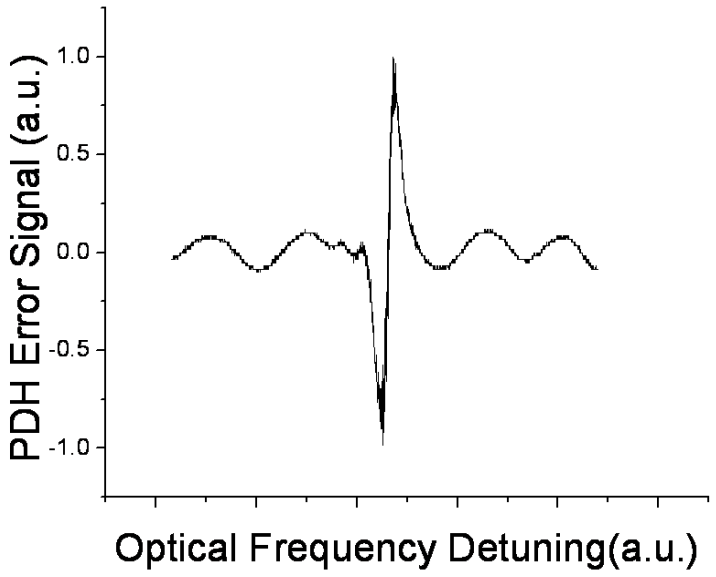

Figure 9: Error signal with ripples (modulation frequency ~ 0.999 f_{FSR}).

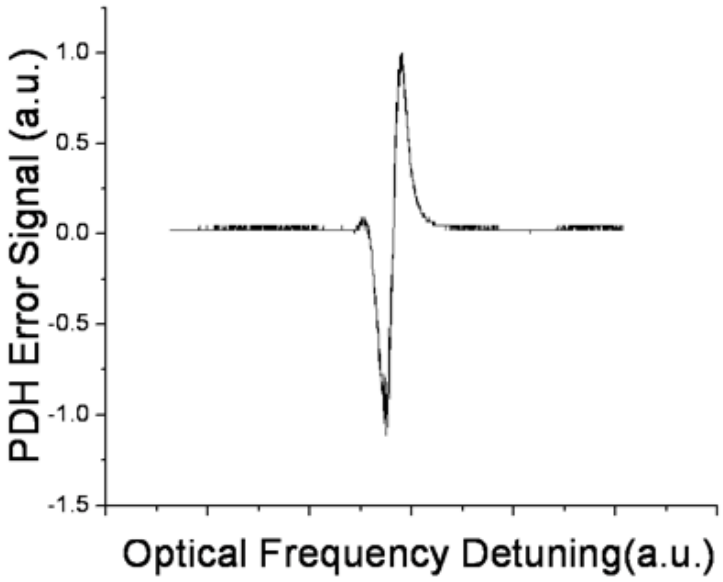

Figure 10: Error signal without ripples (modulation frequency ~ 0.999 f_{FSR})

First, the PDH error signal peak to peak difference against RF modulation frequency is plotted in Fig. 11. As it can be seen from the graph the zero crossing (or FSR value) is between 10.2425GHz and 10.2426GHz. This gives the FSR of the etalon with 100 kHz precision, or 1 part in 10^5, which means the precision of the measurement is improved by one order of magnitude due to the signal-to-noise ratio (SNR) improvement of the error signal in Fig. 10.

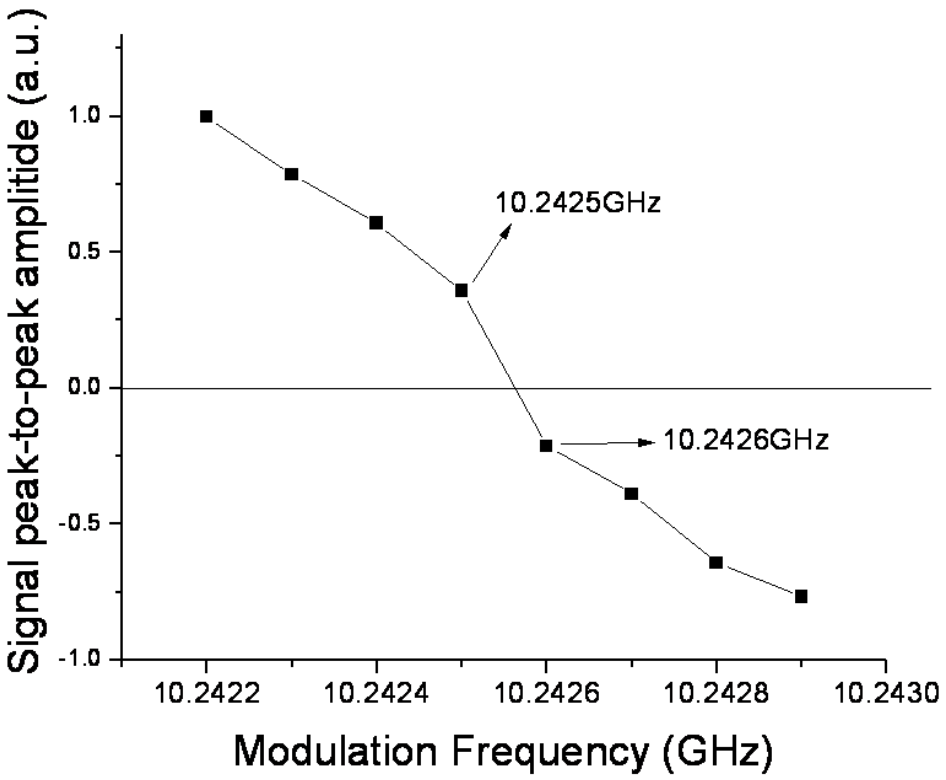

Figure 11: PDH error signal peak-to-peak difference against RF modulation frequency.

As the signal amplitude is very small near the zero crossing, amplitude differences in the PDH error signal peak-to-peak voltage between 10.2425GHz and 10.2426GHz are difficult to measure. Instead of measuring the peak-to-peak voltage, the shape of the PDH error signal was analysed. It can be seen from Fig. 7 that the error signal changes sign (slope) when the modulation frequency passes the FSR. As the error signal changes sign above and below the FSR, instead of measuring the peak to peak amplitude, the shape of the PDH error signal is analysed with 10 kHz steps between 10.2425GHz and 10.2426GHz.

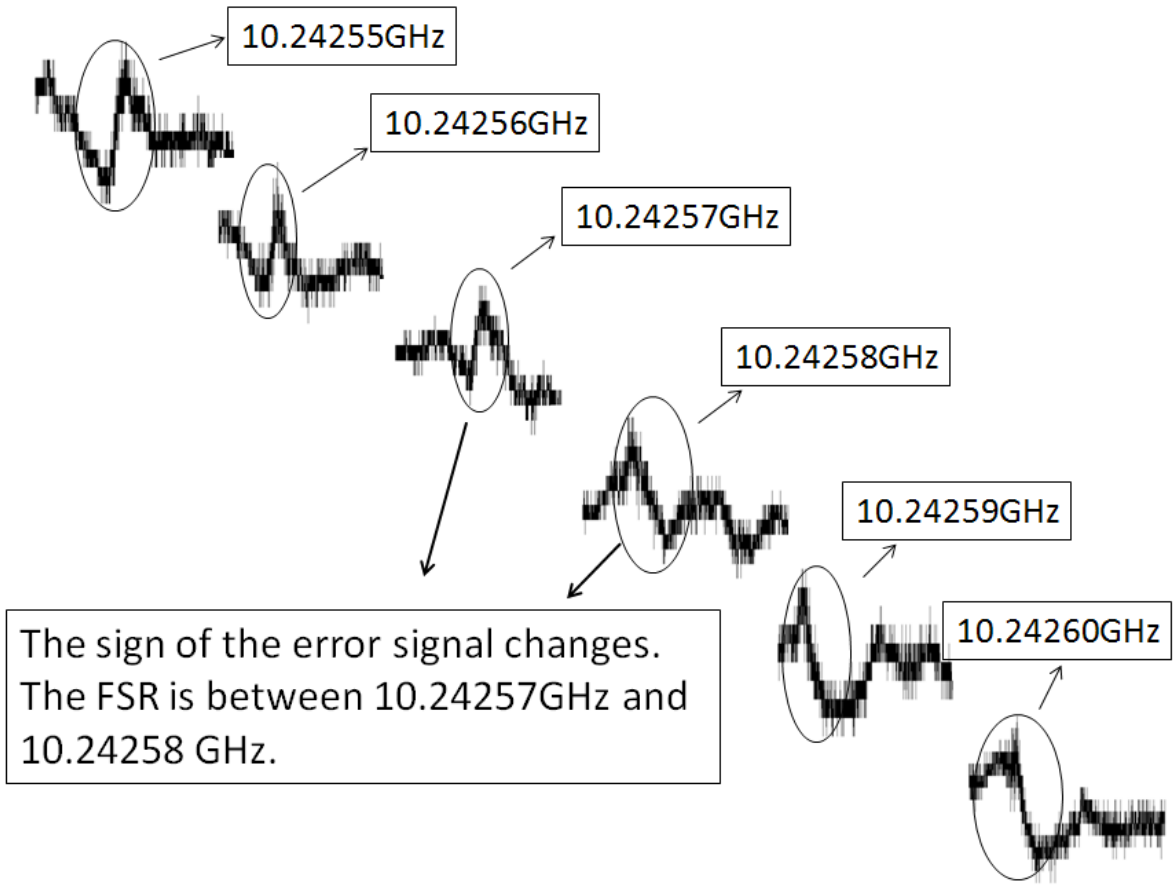

Figure 12: PDH error signals with 10 kHz step modulation frequency increase.

From Fig. 12 it can be clearly seen that, the PDH error signal changes sign between 10.24257GHz and 10.24258GHz. Without the unwanted modulation the accuracy is improved to 100 kHz and the fine analysis of the error signal sign increases the accuracy to 10 kHz or 1 part in 10^6 precision.

Conclusion:

A previously novel PDH based technique for FSR measurement is limited by the static modulation in the error signal. In this paper we improved the PDH based technique by dynamically changing the static modulation and averaging electronically during data acquisition. The elimination of the modulation realizes a 10 kHz accuracy with a 10GHz etalon, which implies a 1 part in 10^6 precision. To our knowledge this is the most precise measurement of FSR.

CHAPTER 3: A SEMICONDUCTOR BASED 10-GHZ OPTICAL COMB SOURCE

Introduction

A semiconductor based 10 GHz mode-locked laser with 1000 finesse intracavity etalon is implemented and characterized.

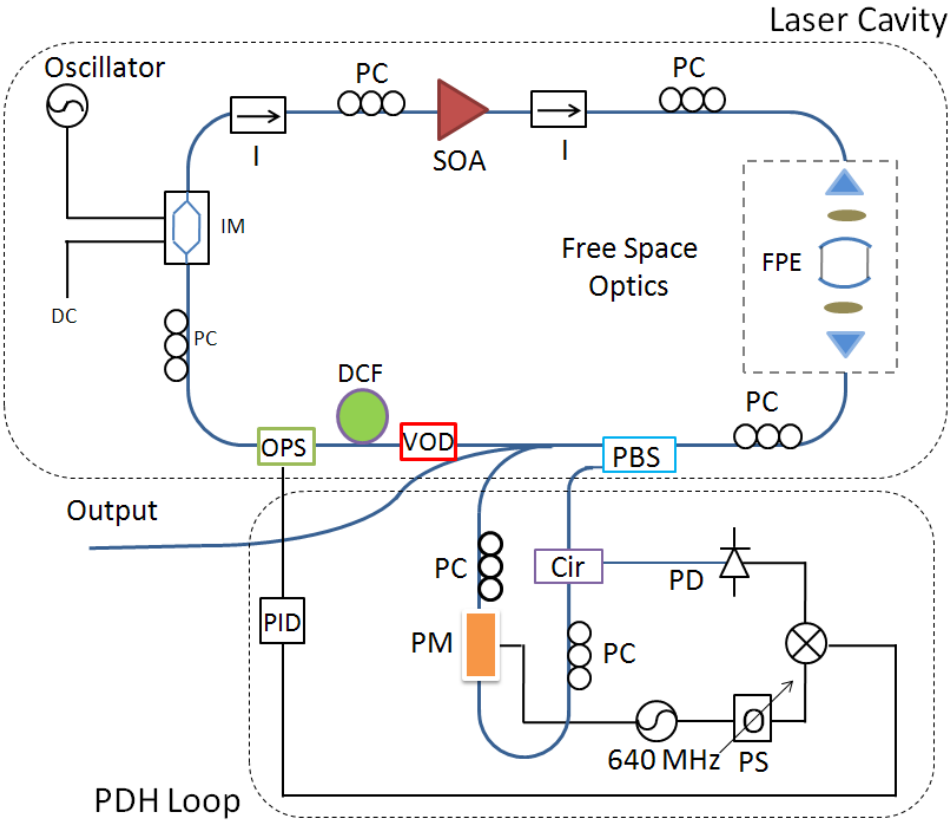

Figure 13: Laser cavity and optical frequency stabilization schematic. I: Isolator, SOA: Semiconductor Optical Amplifier, PS: Phase Shifter, PD: Photodetector, PC: Polarization Controller, IM: Intensity Modulator, PBS: Polarization Beam Splitter, DCF: Dispersion Compensating Fiber, FPE: Fabry-Perot Etalon, PID: PID controller, PM: Phase Modulator, Cir: Optical Circulator, OPS: Optical Phase Shifter, VOD: Variable Optical Delay.

The experimental setup is shown in Fig. 13. The setup has two main parts, the laser cavity and PDH loop. The cavity is ~ 35 meter which corresponds to ~ 5.6MHz cavity fundamental frequency. The cavity consists of a semiconductor optical amplifier (SOA) as the gain medium. The SOA was biased at 600 mA, resulting in an average output power of 8 mW. The mode-locking is done by loss modulation by using an intensity modulator (IM). The intensity modulator is driven by an ultra-low noise oscillator at 10.287 GHz. Two isolators maintain the unidirectionality of the lasing and also they block some of the unwanted reflection from the etalon to the SOA. The etalon has two curved mirrors with 50 cm of radius, a free spectral range of 10.287GHz and finesse of 1000. The resonance of the etalon at full width at half maximum is ~10 MHz. In order to increase the stability of the etalon which is the reference of the MLL, the etalon is sealed and made of ultra-low expansion quartz. The polarization beam splitter (PBS) separetes the two orthogonal polarization states one is coming from the laser cavity and the other one is coming from the PDH loop. Variable optical delay (VOD) and optical phase shifter (OPS) are used for the coarse and the fine tuning of the cavity length. In order to control the dispersion of the cavity 3.5 meter of dispersion compensating fiber (DCF) is added.

Part of the output signal is sent to the Pound-Drever-Hall (PDH) loop. It is phase modulated at 640 MHz and then sent back to the cavity by the orthogonal polarization state. The reflected beam from etalon is again sent back to the PDH loop. The signal is then photodetected and mixed with the local oscillator. The obtained error signal is send to an analog proportional-integral-differential (PID) feedback control circuit, which adjusts the cavity length by using a piezoelectric optical phase shifter. Without the active control of the cavity length, optical cavity length changes owing to the environmental effects, such as temperature changes and mechanical

vibrations. The fluctuations in the optical cavity length will result in fluctuations in the optical frequency change and finally the mode-locking will be destroyed.

Experimental Results

The optical frequency stabilized mode-locked laser with 1000 finesse intracavity etalon has a square spectrum with 10dB optical bandwidth of 8.3nm (Fig. 14). The visibility of the comb lines is limited by the resolution of the optical spectrum analyzer, ~ 0.01nm.

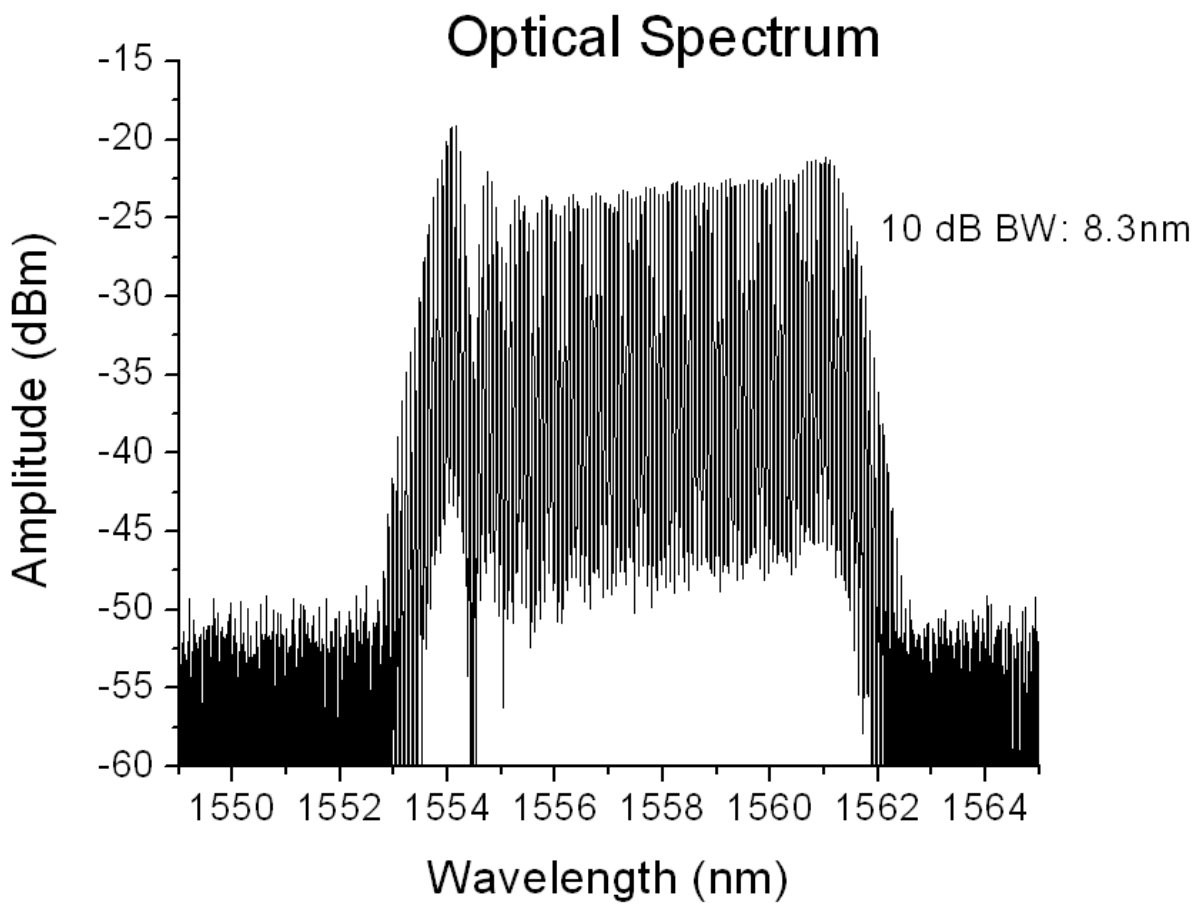

Figure 14: Optical spectrum analyzer.

In order to obtain the optical signal-to noise ratio (OSNR), the optical frequency is down converted by using a narrow linewidth (< 1kHz) CW laser and observed by an RF spectrum analyzer. The down converted single optical tone shows an OSNR of > 75 dB as seen in Fig. 15. It should be noted here that the other optical supermodes are suppressed below the measurement noise floor.

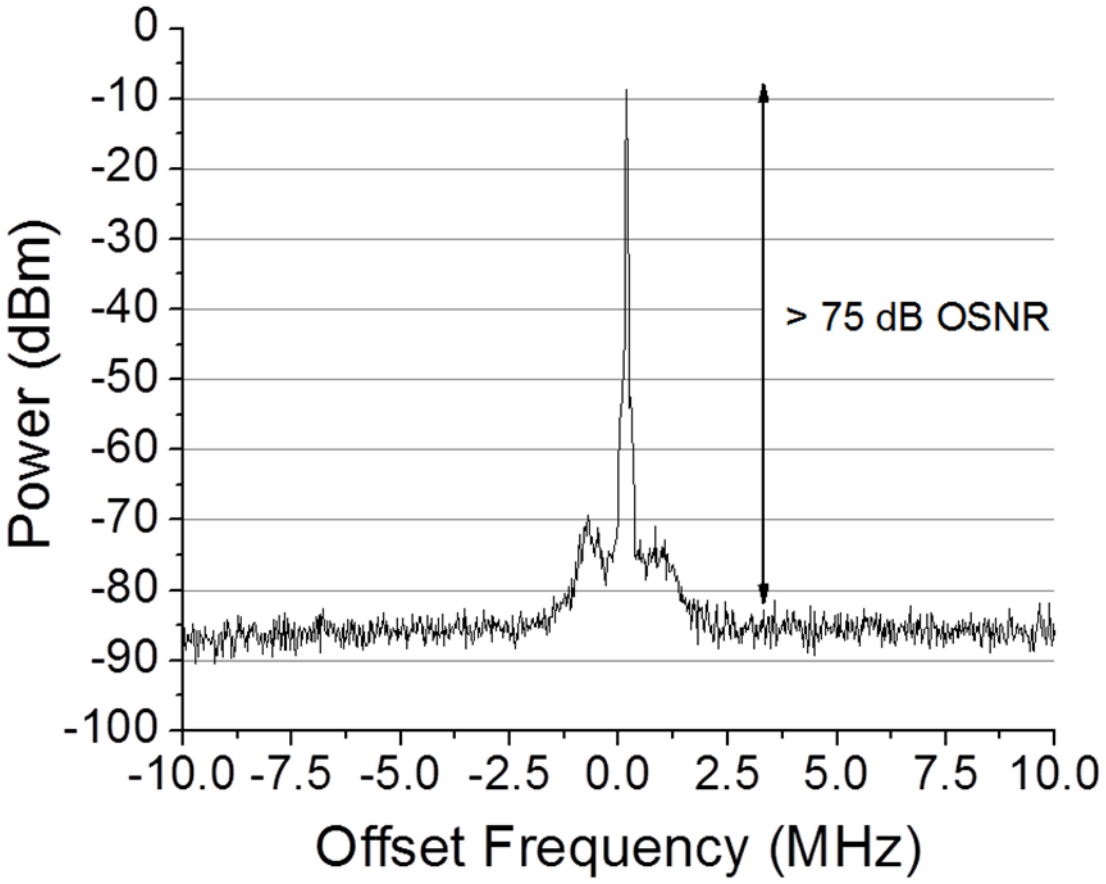

Figure 15: Down converted single optical tone.

The sampling scope trace of the pulse train is shown (without averaging) in Fig. 16. The autocorrelation trace shows a pulsewidth of ~16 ps directly from the mode-locked laser. The pulses are compressed by using a dual grating compressor to 1.1 ps, Fig. 17.

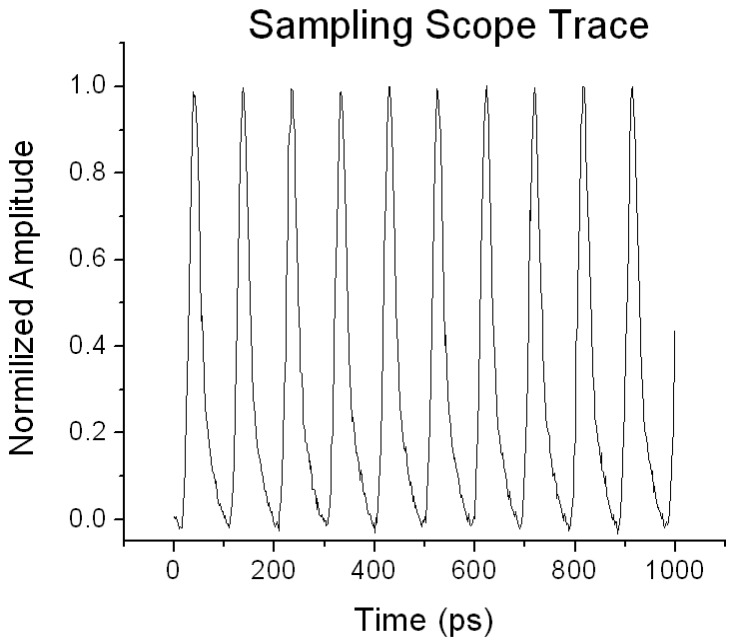

Figure 16: Sampling scope trace.

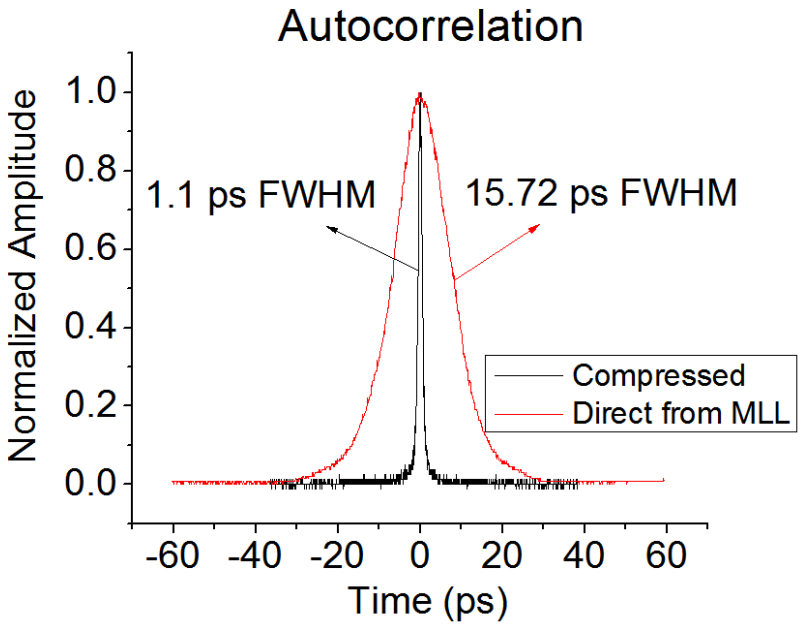

Figure 17: Autocorrelation trace directly from MLL and after compressed by using a dual grating compressor.

The optical linewidth and optical frequency stabilization of the mode-locked laser was measured by beating one of the comb lines with a narrow linewidth CW laser. As the linewidth of the CW laser is narrow (~1 kHz), the linewidth of the mode-locked laser can be estimated from the width of the beat tone. The linewidth of the optical comb line is measured to be < 1 kHz, Fig. 18.

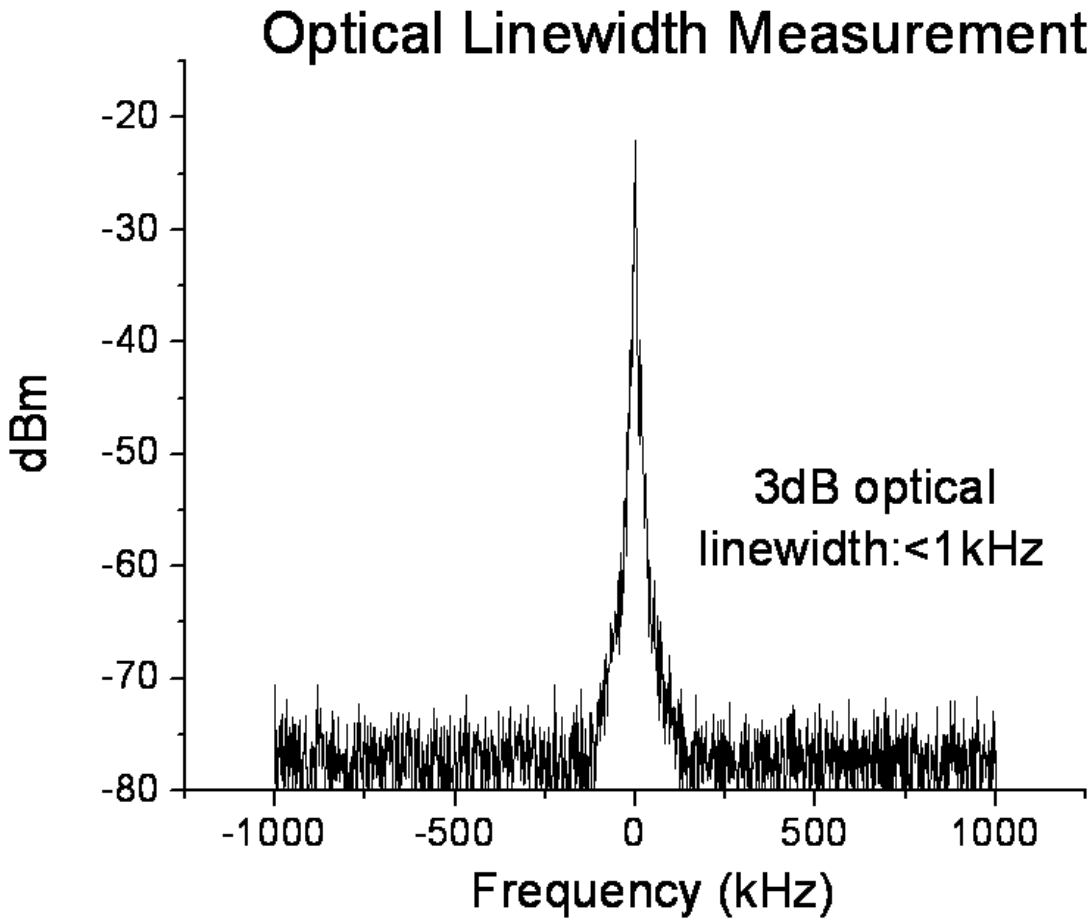

Figure 18: Optical linewidth measurement.

The stability of the optical spectrum of the mode-locked laser is also measured by observing the maximum deviation of the beat signal. The maximum deviation of the beat tone demonstrates the optical stability of the mode-locked laser which is ~ 150 kHz over 30 sec, Fig 19. Note that both the optical linewidth and the optical frequency stability measurements are limited by the linewidth and stability of the CW laser.

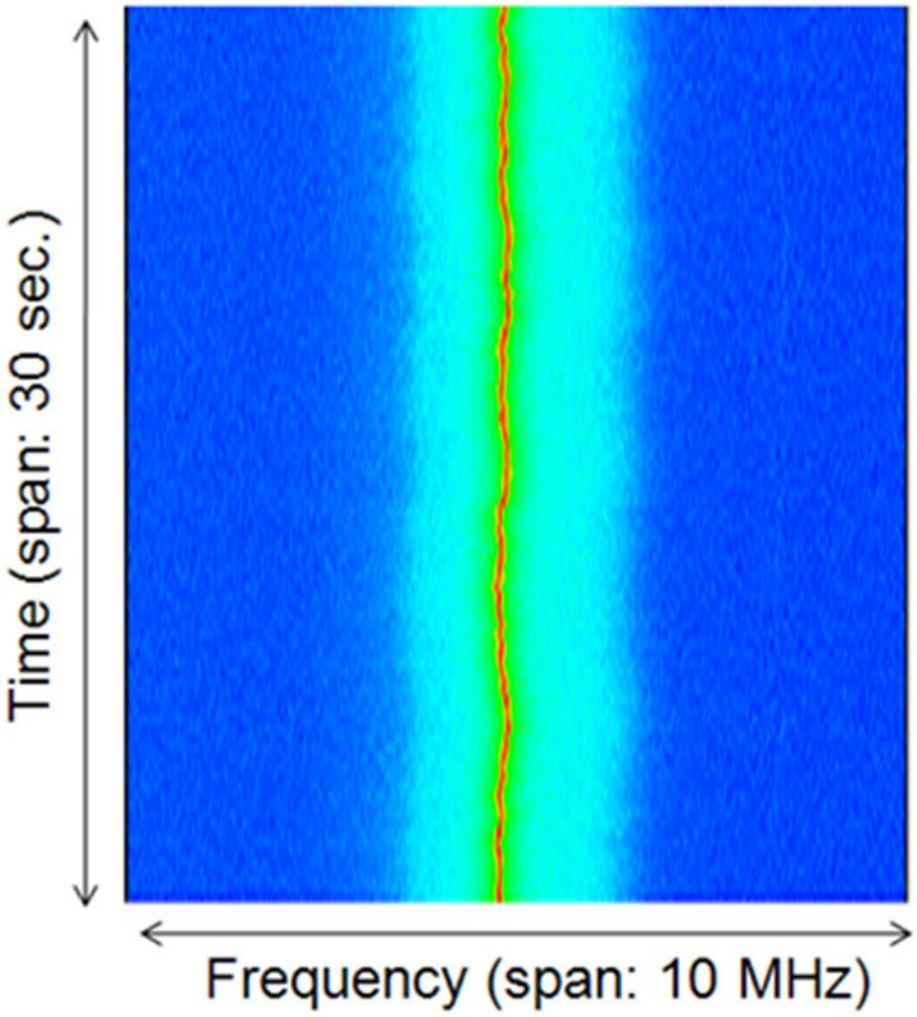

Figure 19: Optical frequency fluctuation over 30 sec.

The optical frequency noise spectrum of the comb lines was also measured referenced to the ULE quartz etalon, shown in Fig. 20. The optical comb lines have a frequency noise of 10 Hz/√Hz at 10 Hz offset frequency.

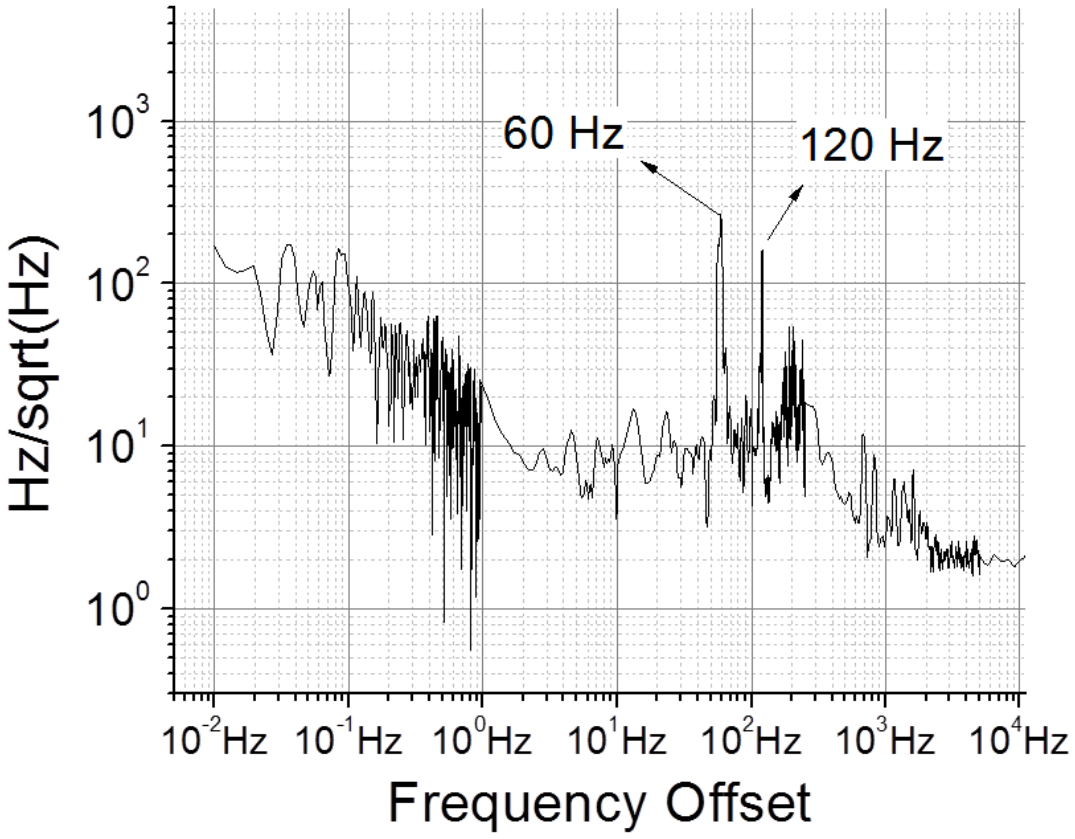

Figure 20: Optical frequency noise spectrum.

The phase and amplitude noise of the photo-detected carrier at 10.287 GHz was also measured. The relative phase noise shown in Fig. 21 starts with ~-100dBc/Hz at 1 Hz and decrease linearly to ~-140dBc/Hz at 1 kHz. After a flat noise spectrum form 1 kHz to 200 kHz, the noise decreases to ~-160dBc/Hz around 10 MHz. The peak of the first supernode noise spur is suppressed below -150dBc/Hz. A timing jitter of 3 fs was obtained via integration of the phase noise spectrum from 1 Hz to 100 MHz, the limit of our measurement capability. By extrapolating to Nyquist

frequency (~5.14GHz), the jitter upto Nyquist is estimated as ~14 fs. The amplitude noise is shown in Fig. 22. The amplitude noise is mostly limited by the noise floor. The integrated amplitude noise is ~0.023% over 1 Hz to 100 MHz.

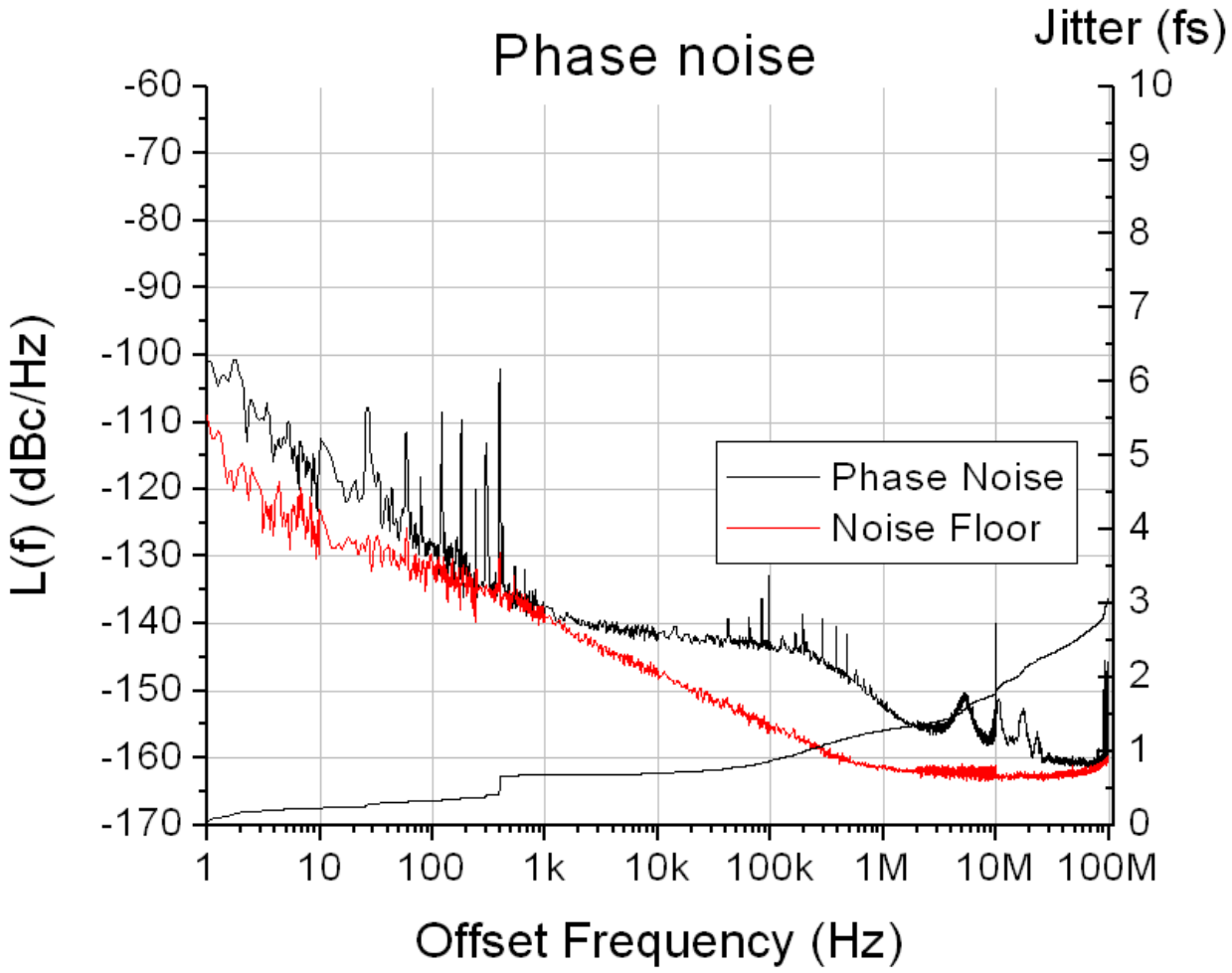

Figure 21: Relative phase noise, noise floor, and integrated timing jitter.

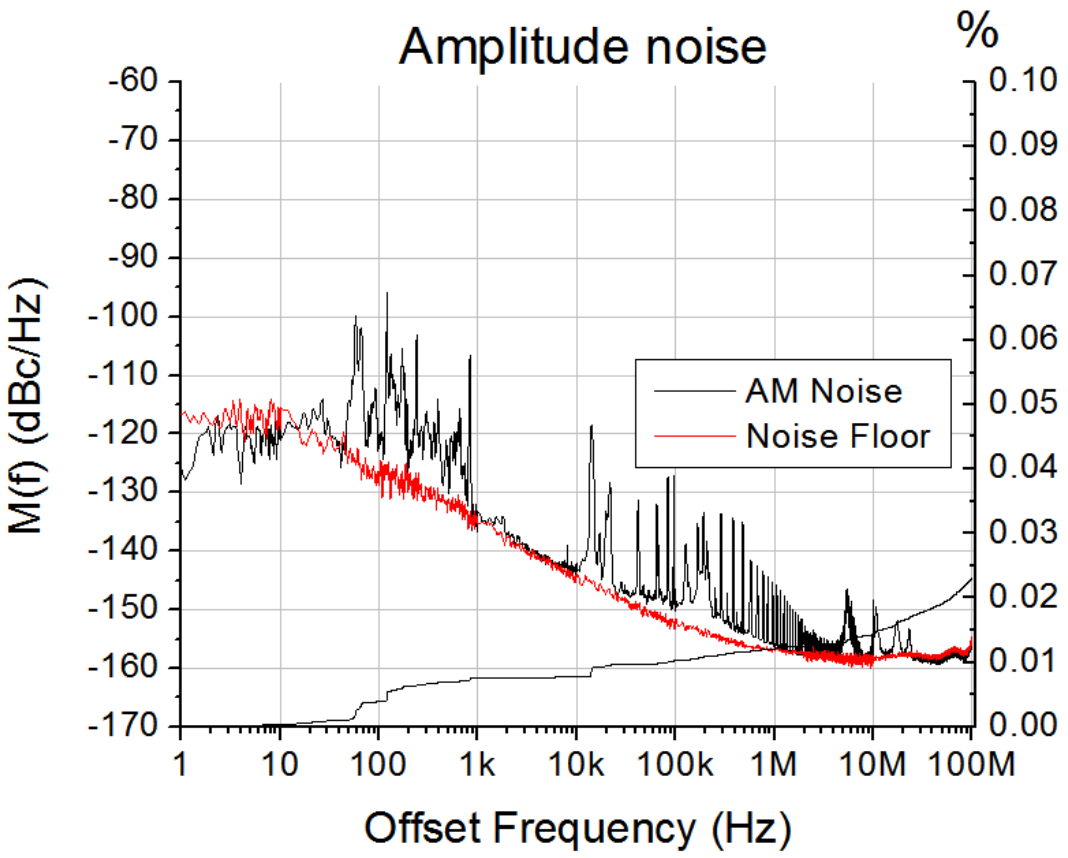

Figure 22: Amplitude noise, noise floor, and integrated amplitude fluctuation.

Conclusion

A 10 GHz mode locked laser with 1000 finesse intracavity etalon is demonstrated. A factor of 10 increase of the finesse allows us to increase the cavity length by a factor of 10 and hence get a lower timing jitter. The timing jitter integrated over 1Hz-100MHz was measured to be 3 fs, the extrapolated timing jitter up to Nyquist is only 14 fs. The integrated amplitude noise of the MLL over 1Hz-100MHz is 0.023%. Optical frequency fluctuations were less than 150 kHz and the

optical comb linewidth is measured as <1kHz. Owing to its well defined stable optical comb and low phase noise this laser has applications in photonic analog to digital conversion, coherent communication, arbitrary waveform generation and optical clock distribution.

CHAPTER 4: REGENARETIVELY MODE-LOCKED LASER

Introduction and experimental setup

High repetition rate, frequency stabilized mode-locked lasers have applications in coherent communication and signal processing such as dense wavelength division multiplexing, optical code division multiple access and optical arbitrary waveform generation [25]. Such systems require low pulse to pulse timing jitter and high optical frequency stability. In order to get low pulse to pulse timing jitter an ultra-low noise RF oscillator is necessary. Such RF oscillators are expensive, heavy and consume too much power. The elimination of the ultra-low noise RF oscillator is possible by using a coupled optoelectronic oscillator (COEO) design [26]. It also has been shown that mode-locked lasers with longer cavities have lower timing jitter owing to higher quality factors [27]. In order to achieve high repetition rates with long cavity, harmonic mode-locking is necessary. Harmonic mode-locking leads to interleaved optical super-modes, competition among which leads to super-mode noise and increased timing jitter. One of the most effective methods to suppress the super-mode noise is to use an intracavity Fabry-Perot etalon. The etalon removes all but one optical super-mode by the periodic filtering thereby eliminating the super-mode noise and lowering the timing jitter. It is important to note that the width of the transmission peaks of the etalon puts a practical upper limit on the laser cavity length. If the cavity length is too long, more than one super-mode set fits within the etalon transmission resonance which will prevent effective elimination of the neighboring super-modes. The optoelectronic loop is formed by a high speed photodetector, an RF amplifier and a phase shifter. Part of the laser output is photodetected, amplified and send to the intensity modulator. Note that

unlike conventional COEO this optoelectronic loop does not consist of an RF filter as the harmonic mode selection is done by the etalon inside the cavity.

Cavity stabilization is necessary in such systems because optical frequency fluctuations may result in a detuning between the etalon transmission peak and optical comb lines, leading to a destabilization of modelocking. There are different methods for optical frequency stabilization but the preferred method for such systems is the Pound-Drever-Hall (PDH) technique [23] as the laser itself contains the optical reference required in the PDH technique.

In this work, a 10.287 GHz semiconductor based coupled optoelectronic oscillator (COEO) with 1000 finesse intracavity etalon is demonstrated. The factor 10 increase in the finesse over previous work [28,29] allows for an increase in the laser cavity length, leading to an increased quality factor and decreased optical linewidth as well as an increase in the optical frequency stability.

The laser schematic is shown in Fig. 23.

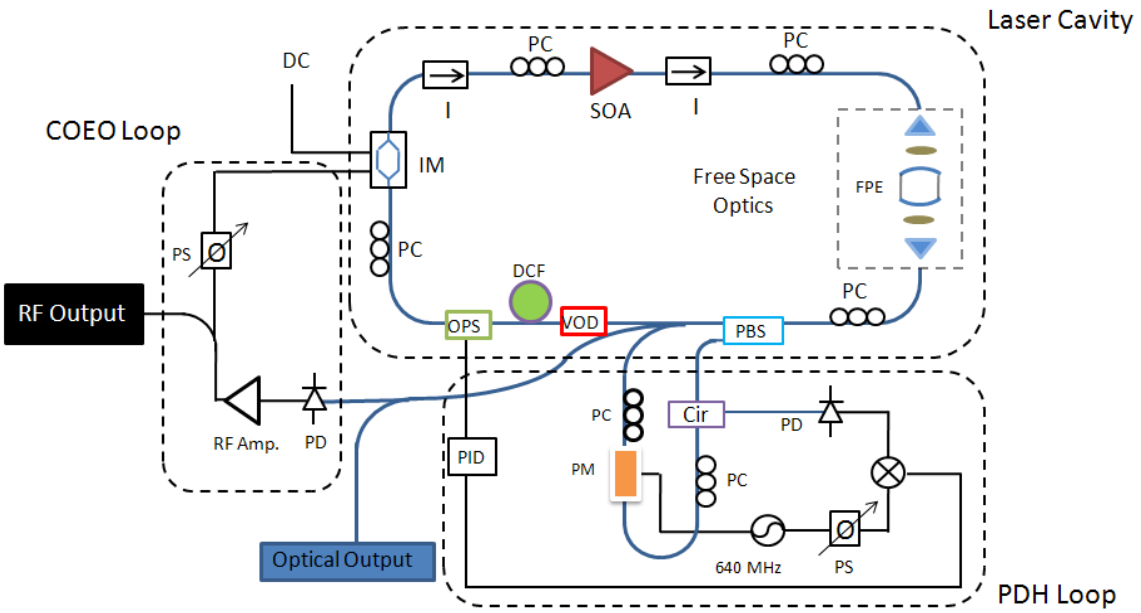

Figure 23: Laser cavity and optical frequency stabilization schematic. I: Isolator, SOA: Semiconductor Optical Amplifier, PS: Phase Shifter, PD: Photodetector, PC: Polarization Controller, IM: Intensity Modulator, PBS: Polarization Beam Splitter, DCF: Dispersion Compensating Fiber, FPE: Fabry-Perot Etalon, PID: PID controller, PM: Phase Modulator, Cir: Optical Circulator, OPS: Optical Phase Shifter, VOD: Variable Optical Delay, RF Amp: RF Amplifier.

Results

In Fig 24, the sampling scope trace of the pulse train is shown. The pulse autocorrelation is shown in Fig. 25. The pulses generated by the COEO has an intensity autocorrelation full-width at half maximum (FWHM) of 25ps. After compressing the pulses by using a dual grating compressor, the pulse FWHM intensity autocorrelation is measured to be 1.5ps. Fig. 26 shows

the RF spectrum view of the pulse train. The first supermode spurs of the cavity are suppressed below 121 dBc/Hz.

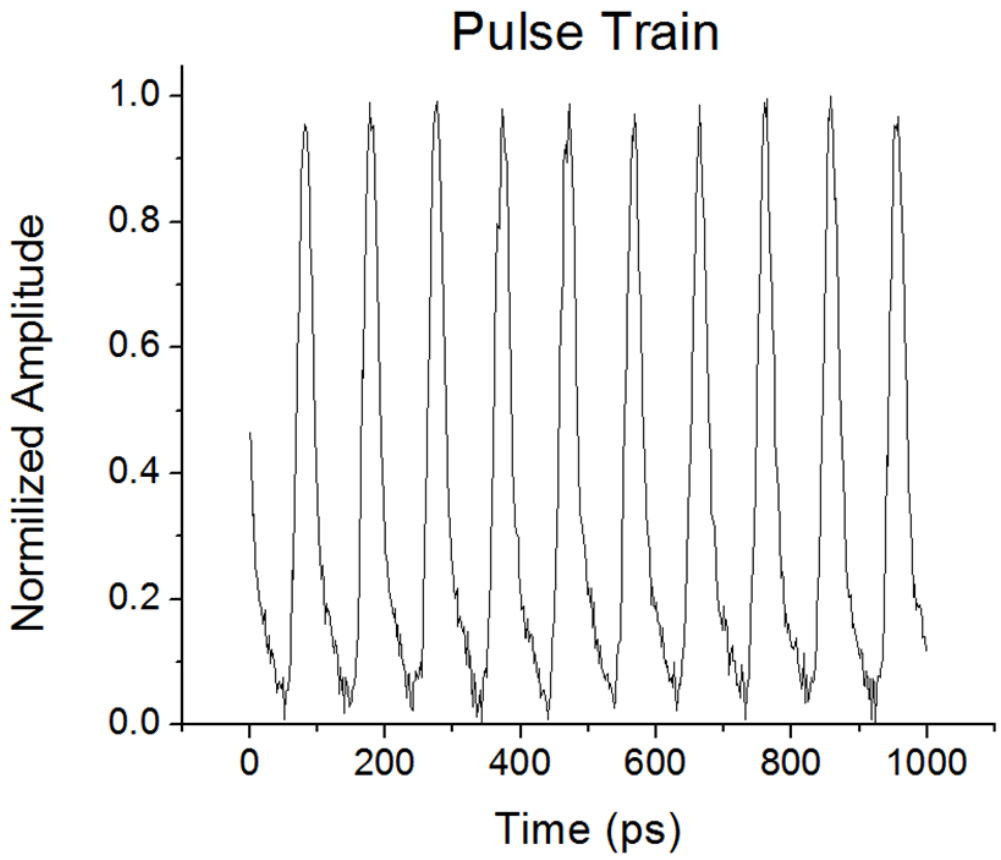

Figure 24: Sampling scope trace of the pulse train.

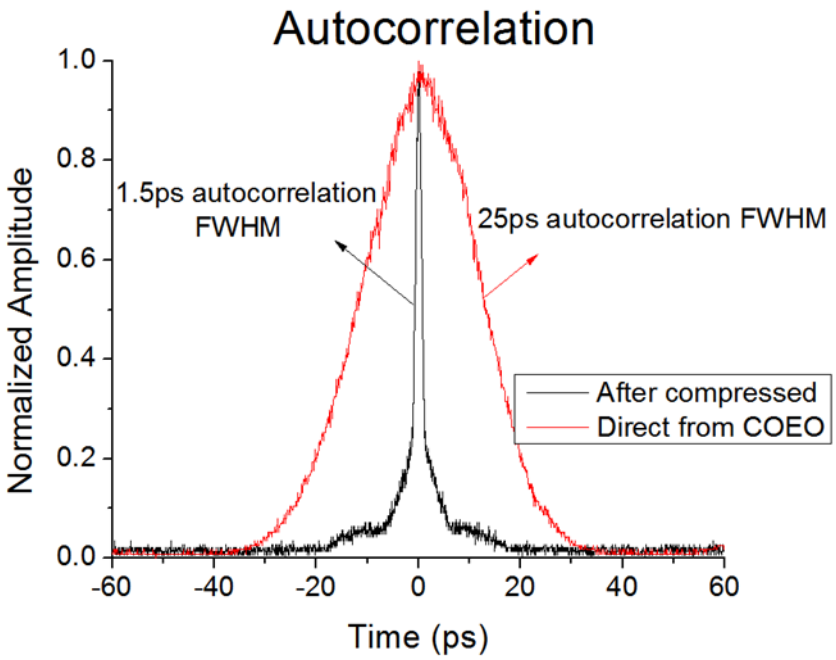

Figure 25: Autocorrelation trace.

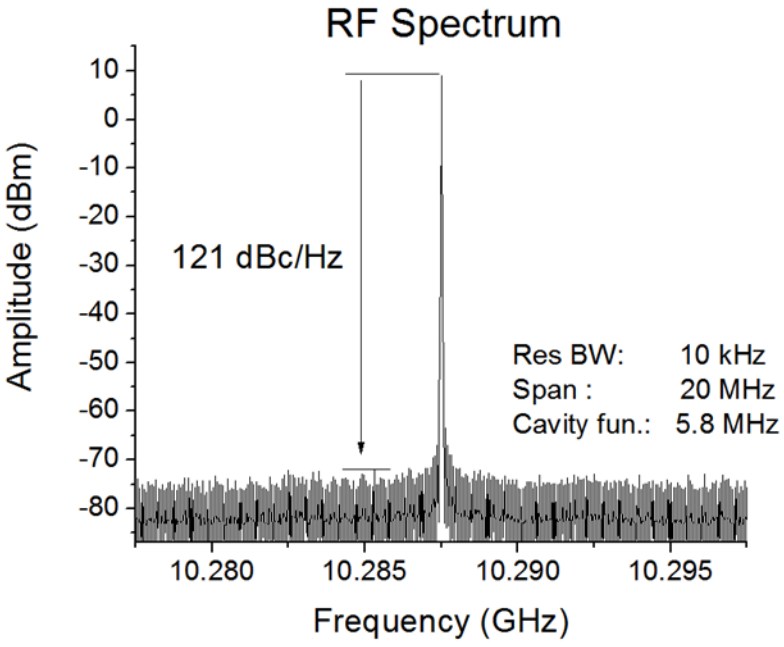

Figure 26: The RF spectrum of photo-detected pulse train.

The laser optical spectrum is shown in Fig. 27. The spectrum has a -10 dB bandwidth of >5 nm. The visibility of the comb lines is limited by the resolution of the optical spectrum analyzer. The high resolution optical spectrum analyzer shows ~47 dB signal-to-noise ratio (Fig 28).

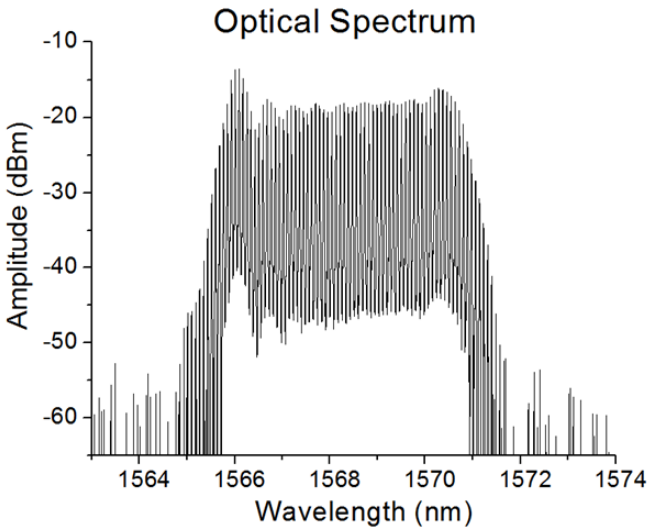

Figure 27: Optical spectrum

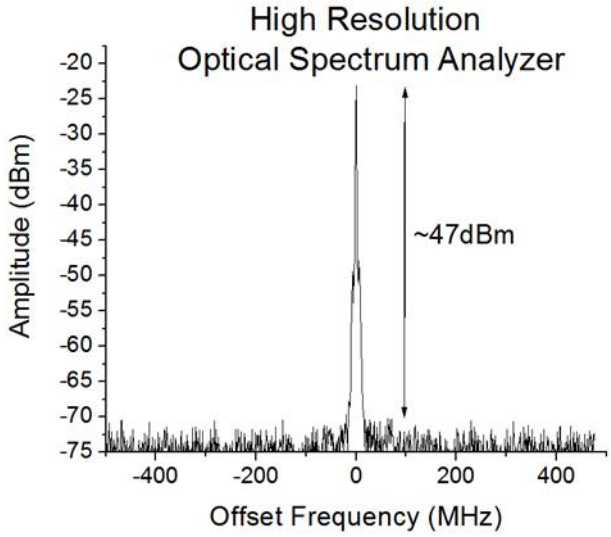

Figure 28: High resolution optical spectrum

The optical linewidth and optical frequency stability of the COEO is measured by mixing one of the opticsl comb lines with a narrow linewidth CW laser. As the linewidth of the CW laser is narrow (~1 kHz), the linewidth of the mode-locked laser can be estimated from the width of the beat tone.

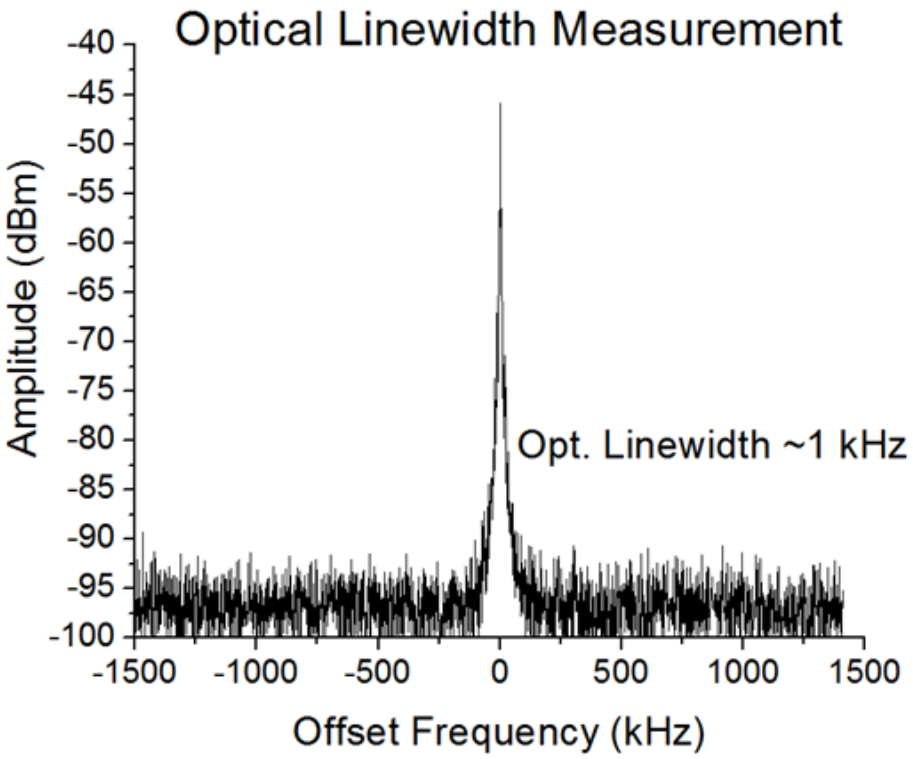

Figure 29: Optical linewidth measurement

The stability of the optical spectrum of the mode-locked laser is also measured by observing the maximum deviation of the beat signal. The linewidth of the optical comb line is measured to be < 1 kHz (Fig. 29), and the maximum deviation of the beat tone demonstrates the optical

stability of the mode-locked laser which is ~ 150 kHz over 30 sec (Fig 30). Note that both the optical linewidth and the optical frequency stability measurements are limited by the linewidth and stability of the CW laser.

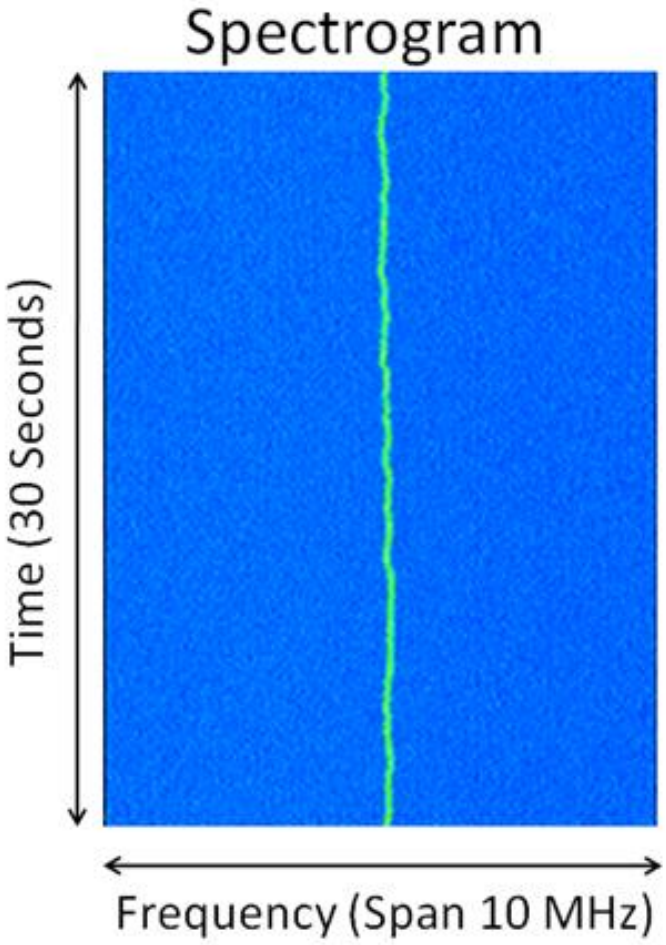

Figure 30: Spectrogram of the beat tone over 30 sec.

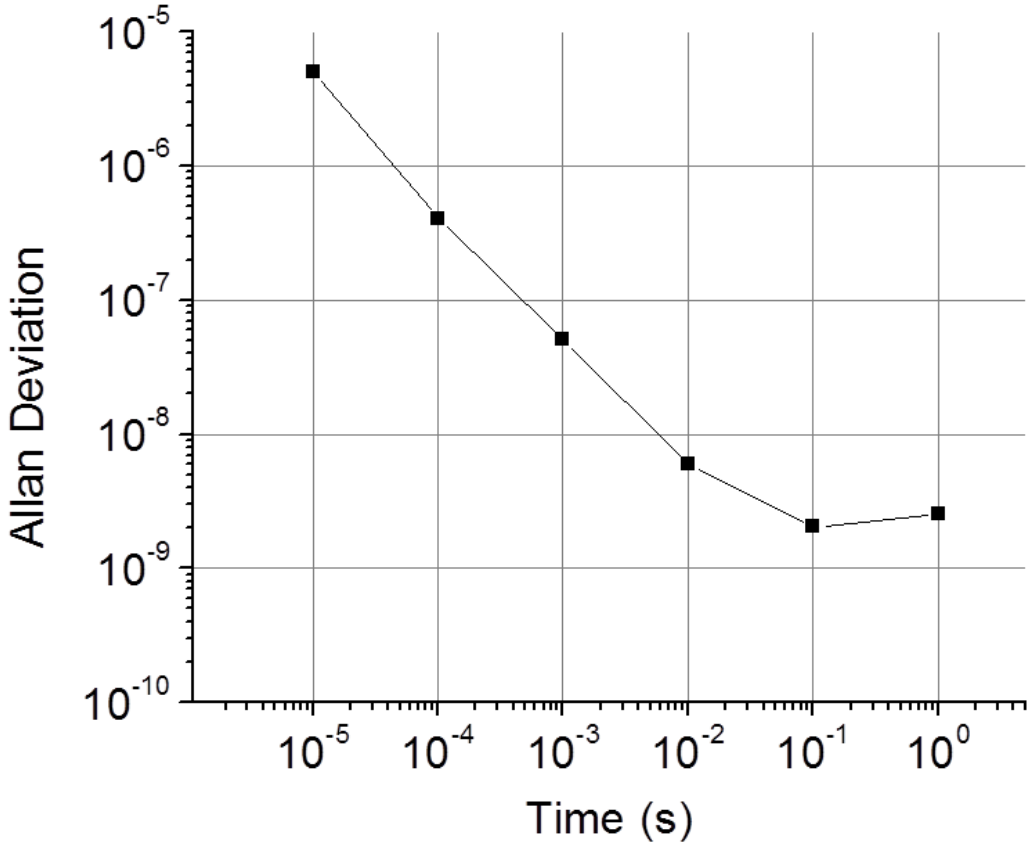

Figure 31: Allan deviation measurement of the COEO.

Allan deviation measurement of the COEO is also done and resulted in an RF frequency stability of ~ 10^{-9} in 0.1 seconds (Fig. 31).

Conclusion

A 10.287 GHz semiconductor based coupled optoelectronic oscillator with 1000 finesse intracavity etalon is demonstrated with, < 1kHz optical linewidth and ~150 kHz optical frequency instability and >121dBc/Hz RF supermode noise spur suppression.

CHAPTER 5: AN INTERFEROMETRIC METHOD FOR HIGH EXTINCTION RATIO MEASUREMENTS

Pulse picking for the generation of low repetition rate pulses from a high repetition rate pulse source has applications in chirped pulse amplification, eXtreme chirped pulse amplification [30-32], and time division demultiplexing [33-35]. The figure of merit of a temporally demultiplexed pulse train is the dynamic extinction ratio (DER). The DER is the extinction ratio of the modulator when it is driven at high speeds as compared to measuring the extinction ratio under DC bias conditions. Developments in device technology have led to very high dynamic extinction ratios [36]. As the dynamic extinction ratio improves, direct measurement methods, such as using a sampling oscilloscope, high dynamic range intensity autocorrelation methods [37] start to fail due to the limited dynamic range, typically ~30dB. Optical spectrum analyzer (OSA) based techniques rely on high modulation rates and will fail for pulse picking applications where the pulse repetition rate is smaller than the OSA resolution [38]. A novel interferometric method for measuring the dynamic extinction ratio is reported with a dynamic range of 60dB and the DER of the temporally demultiplexed pulse train is measured with the introduced method and found to be 44 dB which is 14dB higher than previously reported [39].

Temporally demultiplexing of pulses

The experimental setup for temporally demultiplexing a pulse train is shown in Fig. 32. The incoming pulses from a mode-locked laser at 5 GHz (Fig. 33) is sent to the HEM where the pulses are temporally demultiplexed to 150 MHz (Fig 34). The pulse width of the optical pulses is 40 ps. The HEM is optimized to minimum transmission by a DC power supply. By using a

bias-T, the HEM is driven by an electrical pulse generator producing pulses with 100ps full width half maximum (FWHM) at a repetition rate of 150 MHz. When observed with a sampling scope the electrical signal has a ringing following to the signal which is mapped to the picked pulses in Fig. 34.The amplitude of the electrical pulse signal is 5V whereas the Vpi of the HEM is 7V.

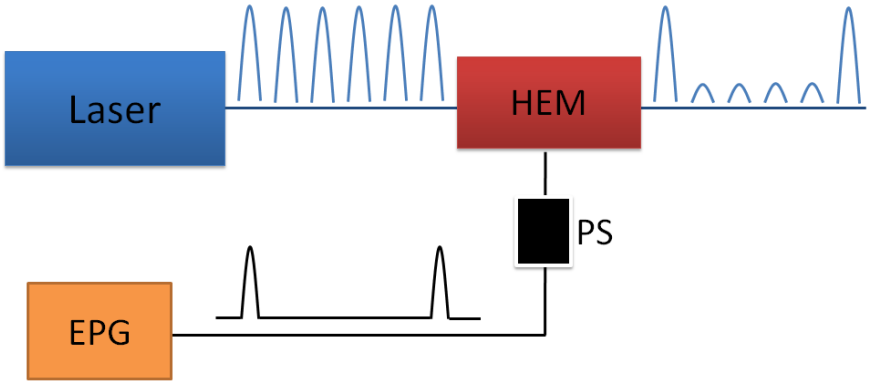

Figure 32: Experimental setup. EPG, Electrical Pulse Generator; PS, Phase Shifter; and HEM, High Extinction Modulator.

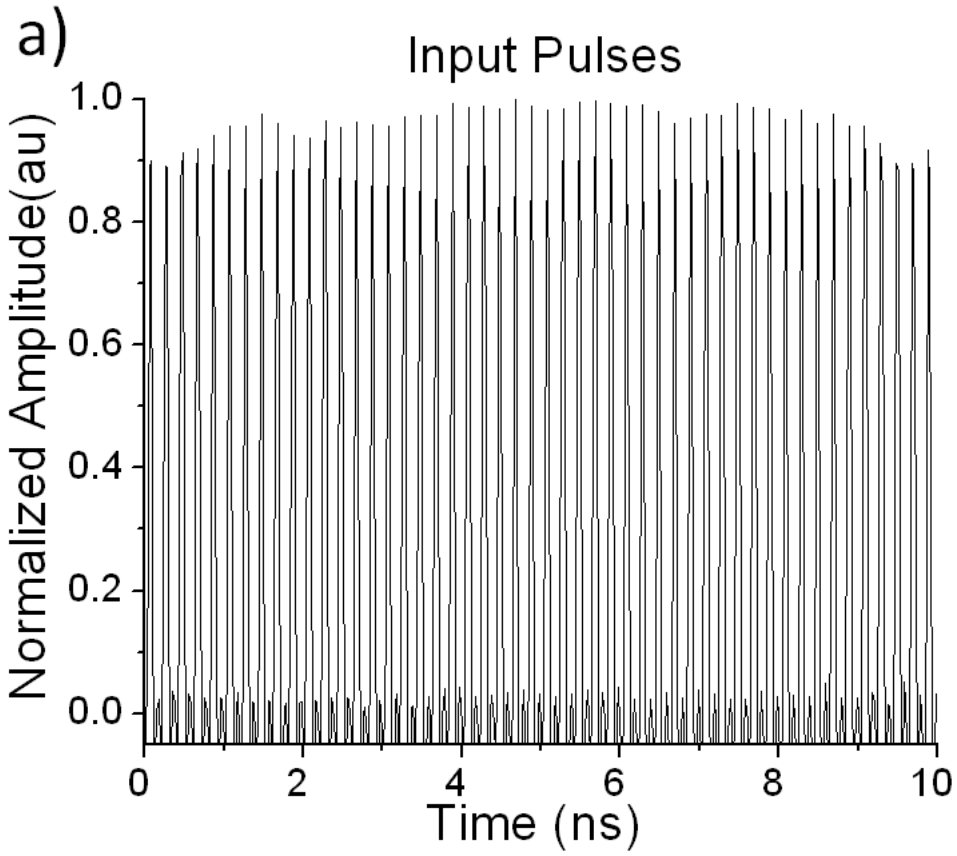

Figure 33: The input pulses form a mode-locked laser (nonuniformity of pulse amplitudes is due to aliasing).

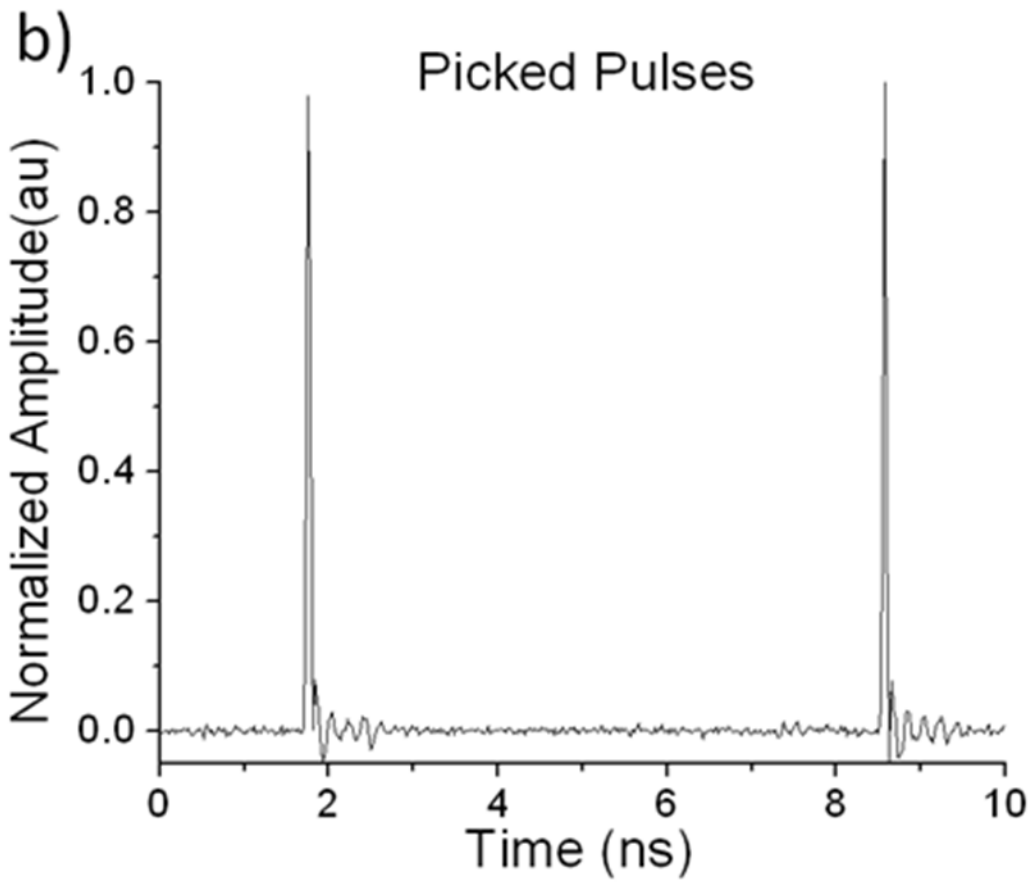

Figure 34: The demultiplexed pulse train at 150 MHz..

The input and output pulses are detected by using a high speed photo detector and observed with a sampling scope. The ringing following the temporally demultiplexed pulses is due to the ringing in the electrical signal.

The dynamic extinction ratio of the temporally demultiplexed pulses is sufficiently high that it could not be measured with any direct measurement method. As a result, the temporally selected pulses are sent to the interferometric setup for the dynamic extinction ratio measurement.

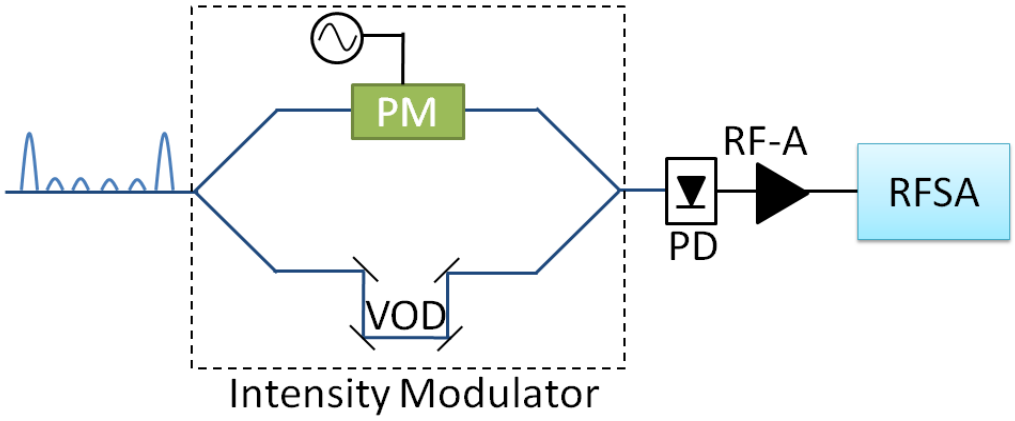

Figure 35: Experimental setup of the extinction ratio measurement setup. PM, phase modulator; VOD, variable optical delay; PD, photo detector, RF-A, RF amplifier; RFSA, RF spectrum analyzer.

The measurement setup shown in Fig. 35 consists of an interferometer which has a phase modulator (PM) in one arm and a variable optical delay (VOD) in the other arm. During the experiment the PM is driven with a sine wave. This interferometric setup can be considered as an intensity modulator with a variable optical delay in one arm. The phase modulation imposes an intensity modulation on the pulses. The combined pulses are photo-detected, amplified with an RF amplifier, and the power at the phase modulation frequency is measured with a RF spectrum analyzer (a lock-in-amplifier can also be used).

The amplitude of the photo-detected RF signal due to this intensity modulation depends on the relative delay between the arms. By using the VOD, two different delay configurations are analyzed. The first case is for two selected pulses overlapping in time (Fig. 36(a)) and the second case is for one selected pulse from one arm overlapping with the extinguished pulse from the

second arm (Fig. 36(b)). As the first configuration interferes two selected pulses, it gives higher RF signal power than the second case. The dynamic extinction ratio of the temporally demultiplexed pulse train can then be determined by comparing the RF signal power difference of these two configurations.

It should be noted that the measurement method requires high pulse to pulse correlation. In this experiment a harmonically mode-locked laser is used as the pulse train source. Harmonically mode locked lasers do not necessarily have high pulse to pulse correlation [40-41]. The pulse to pulse correlation of the pulse train is verified by comparing the RF signal powers of the interfering pulses for the two different cases. The incoming pulses from the MLL are sent to the interferometric setup without pulse picking. The combined pulses are photo-detected, amplified with an RF amplifier, and the power at the repetition rate is measured with a RF spectrum analyzer. The resulting RF powers of the combined pulses are nearly the same for the two pulse positions, thus insuring that the pulses are highly correlated for the inserted time delay.

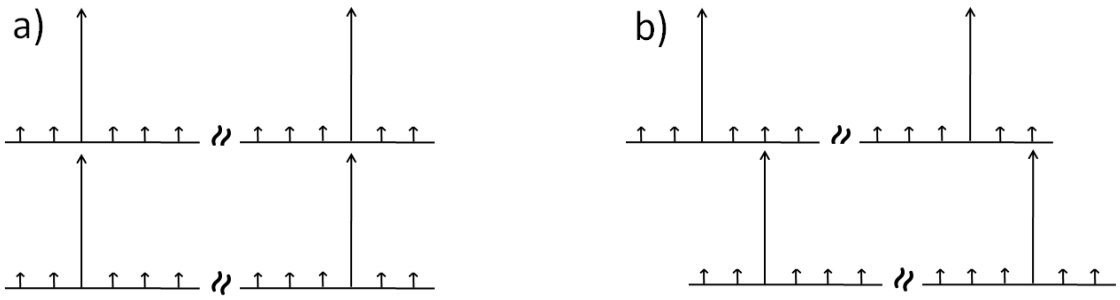

Figure 36: Relative pulse position that results in maximum RF power (a); and minimum RF power(b).

We define the intensity of the selected pulse as I_1 with electric field E_1 and the intensity of extinguished pulses as I_2 with electric field E_2. When the selected pulses overlap in time, the average intensity of the pulses shown in Fig 36(a) can be written as:

$$I_{avg-A} = \left|E_1 + E_1 e^{i\varphi}\right|^2 + \left|\sum (E_2 + E_2 e^{i\varphi})\right|^2 \tag{6}$$

where φ is the phase shift due to the phase modulation. As the E_2 is very small when compared to E_1, ${E_2}^2$ terms are ignored. The average intensity is given as:

$$I_{avg-A} \approx 2 \cdot I_1 + 2 \cdot I_1 \cos(\varphi) \tag{7}$$

As the RF power is proportional to the square of the intensity, the power of the RF signal is given by:

$$P_{A-RF} = A \cdot 4 \cdot I_1^2 \cdot \cos^2(\varphi) \tag{8}$$

where A is a constant.

When the selected pulses overlap with extinguished pulses, the average intensity of the pulses that are in Fig. 36(b) is given as:

$$I_{avg-B} = \left|E_1 + E_2 e^{i\varphi}\right|^2 + \left|E_1 e^{i\varphi} + E_2\right|^2 + \left|\sum (E_2 + E_2 e^{i\varphi})\right|^2 \tag{9}$$

After ignoring the ${E_2}^2$ terms and simplifying we get:

$$I_{avg-B} = 2I_1 + 4\sqrt{I_1 I_2}\cos(\varphi) \tag{10}$$

and the corresponding RF signal power becomes:

$$P_{B-RF} = A \cdot 16 \cdot I_1 \cdot I_2 \cos^2(\varphi) \tag{11}$$

The dynamic extinction ratio is the intensity ratio of the selected pulses to the extinguished ones, which is I_1/I_2 .

From the ratio of the RF signals the dynamic extinction ratio can be written as:

$$DER = I_1 / I_2 = 4 \cdot P_{A-RF} / P_{B-RF} \tag{12}$$

or in dB scale:

$$DER = P_{A-RF} - P_{B-RF} + 6 \tag{13}$$

As a result, the change in the RF signal is a direct measure of the dynamic pulse extinction ratio, quantitatively showing the quality of pulse picking.

Measurement Results and Discussion

As mentioned above, the input pulses at 5GHz are temporally demultiplexed to 150 MHz by selecting every 34th pulse (Fig. 34). The selected pulses are then sent to the DER measurement setup (Fig. 35). As a result of the phase modulation at 5 MHz, the output pulses are intensity modulated at 5 MHz. The intensity modulated pulses are first photo detected and after amplification measured at the RF spectrum analyzer.

When the interfering pulses overlap as in Fig. 36 (a), the resulting RF power is -46dBm as shown in Fig. 37. The RF spectrum in Fig. 38 corresponds to the case shown in Fig. 36 (b), and the RF power is-78dBm.

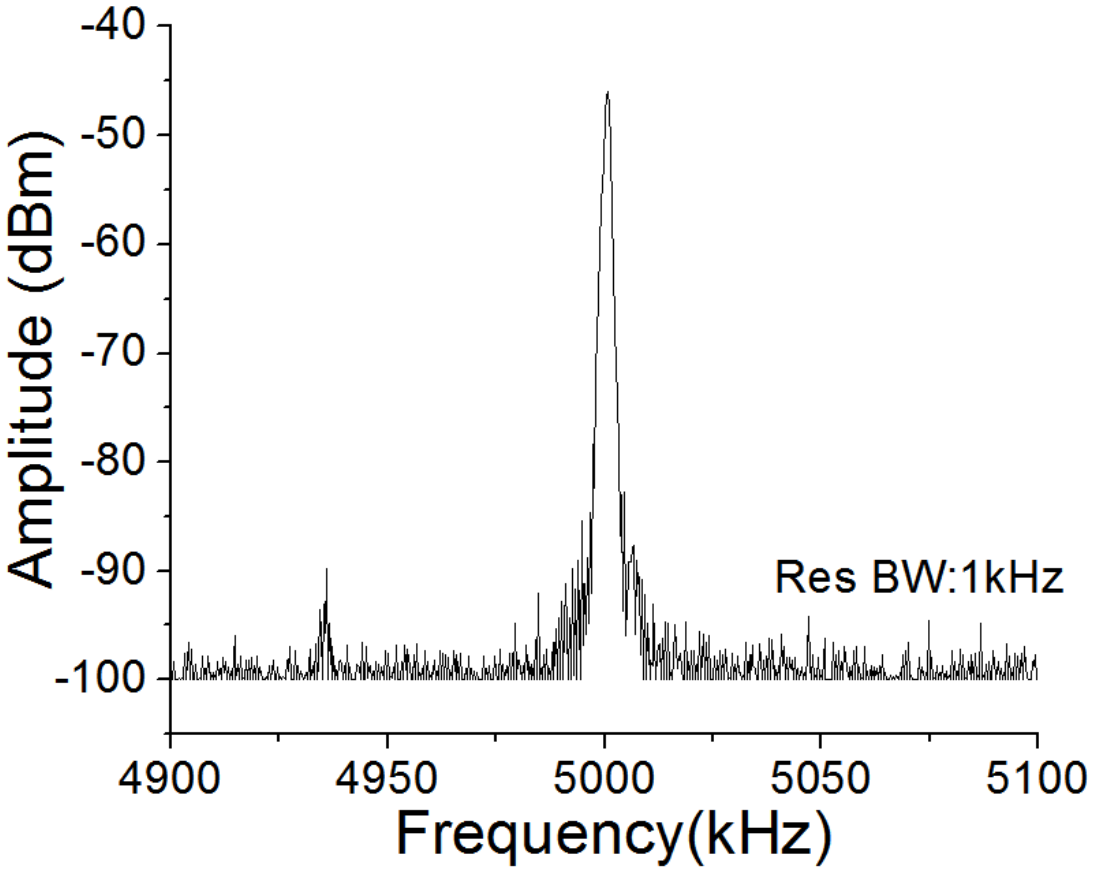

Figure 37: RF Signal, (a) when two picked pulses are overlap, (b) when the picked pulse is overlap with the eliminated pulse.

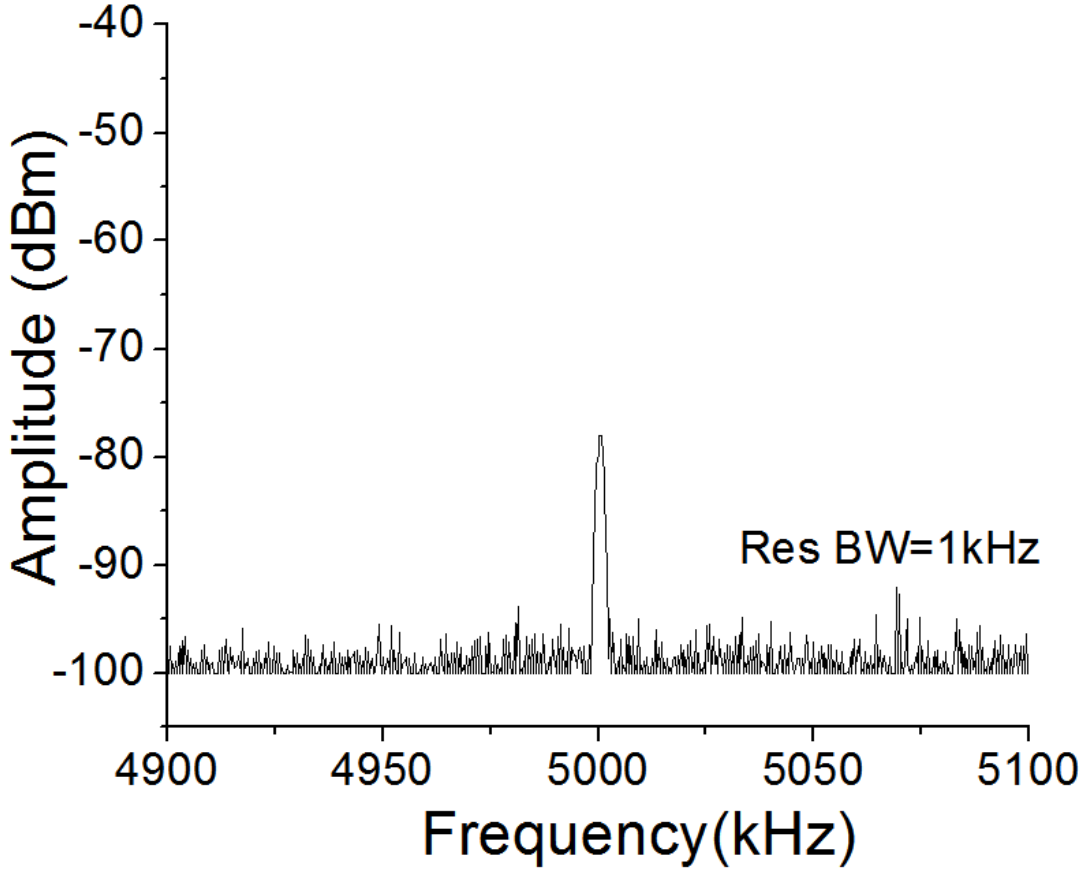

Figure 38: RF Signal, when the picked pulse is overlap with the eliminated pulse.

The RF power difference, normalized to the nonlinear amplification of the RF amplifier, is 38 dB. By adding 6dB, from equation (13), the extinction ratio is found to be 44dB. The dynamic range of the measurement method is limited by the signal to noise ratio (SNR). Therefore it can be improved by increasing the SNR (increasing the input optical power and photodetector responsivity, using a higher gain RF amplifier or lower loss modulator etc…). Under the test

conditions the SNR is found to be ~54 dB. After adding 6 dB according to equation (13), the dynamic range is found to be ~60 dB.

Conclusion

A novel method for measuring the dynamic extinction ratio is demonstrated for cases where the extinction ratio is very large and cannot be measured with conventional methods. Our approach is based on a comparison of the RF signal powers of interfering the various combinations of selected pulses and extinguished pulses. The measured extinction ratio, of the HEM is found to be 44 dB. This method has a dynamic range of ~60dB. To our knowledge, this is the highest dynamic extinction ratio measurement method for high speed optical modulators.

CHAPTER 6: LOW NOISE OPTICALLY TUNABLE OPTO-ELECTRONIC OSCILLATOR WITH FABRY-PEROT ETALON

The use of photonic based techniques for the generation of low noise, high repetition rate microwave signals has recently received significant attention in the research community due to the extraordinary spectral purity and low phase noise of the microwave signal that can be generated from a simple setup. Preliminary work in this area showed the potential for the development of multi gigahertz RF sources using photonics by Neyer and the others [42,43]. However the opto-electronic oscillator did not receive great attention until Yao and Maleki used an optical fiber as the high Q element to obtain extraordinary high spectral purity and low phase noise [44,45]. Since then, several different types of OEO designs have been demonstrated successfully such as the multi-loop OEO architecture, OEO with direct modulation of the laser source, electro absorption modulator and OEO with photonic filters which use atomic cells [46-52]. Also a coupled opto-electronic oscillator scheme is used to generate both mode-locked optical frequency comb lines and a low noise RF tone [53,54].

The standard OEO design consists of a seed laser source followed by an intensity modulator. After passing through an optical delay line, the signal is photodetected, filtered by an RF filter, amplified, and then sent back to the modulator to complete the loop. There are some drawbacks of the standard OEO design: a high gain RF amplifier is needed in order to compensate for losses in the RF loop, and it is costly to make an ultra-narrow bandwidth RF filter which is required when the optical delay line is long. Moreover, the additional loss from the RF filter decreases the cavity Q and hence increases the phase noise. Another drawback of the RF filter is its temperature dependency; small fluctuations in temperature result in fluctuations of

the resonance frequency, and hence the phase induced by RF filter changes. This phase change affects the total round trip time of the microwave signal, thus changing the oscillation frequency.

A new optoelectronic loop design which uses a high finesse Fabry-Perot etalon as the mode selector instead of an RF filter is introduced. The effect of Fabry-Perot etalon transmission phase is analyzed and experimentally demonstrated. The inclusion of the Fabry-Perot etalon instead of the RF filter results in lower phase noise due to the higher Q, and also results in higher RF frequency stability due to the ultralow temperature dependency of the Fabry-Perot etalon. The results of the OEO with a Fabry-Perot etalon are compared with a conventional OEO with an RF filter. When the same laser source, intensity modulator, optical delay, and RF amplifier are used, the OEO with the Fabry-Perot etalon results in lower phase noise and higher RF frequency stability. In the last part of the paper, an opto-electronic oscillator based on single side band modulation technique is presented and the results are compared with the etalon based OEO technique that uses double side band modulation.

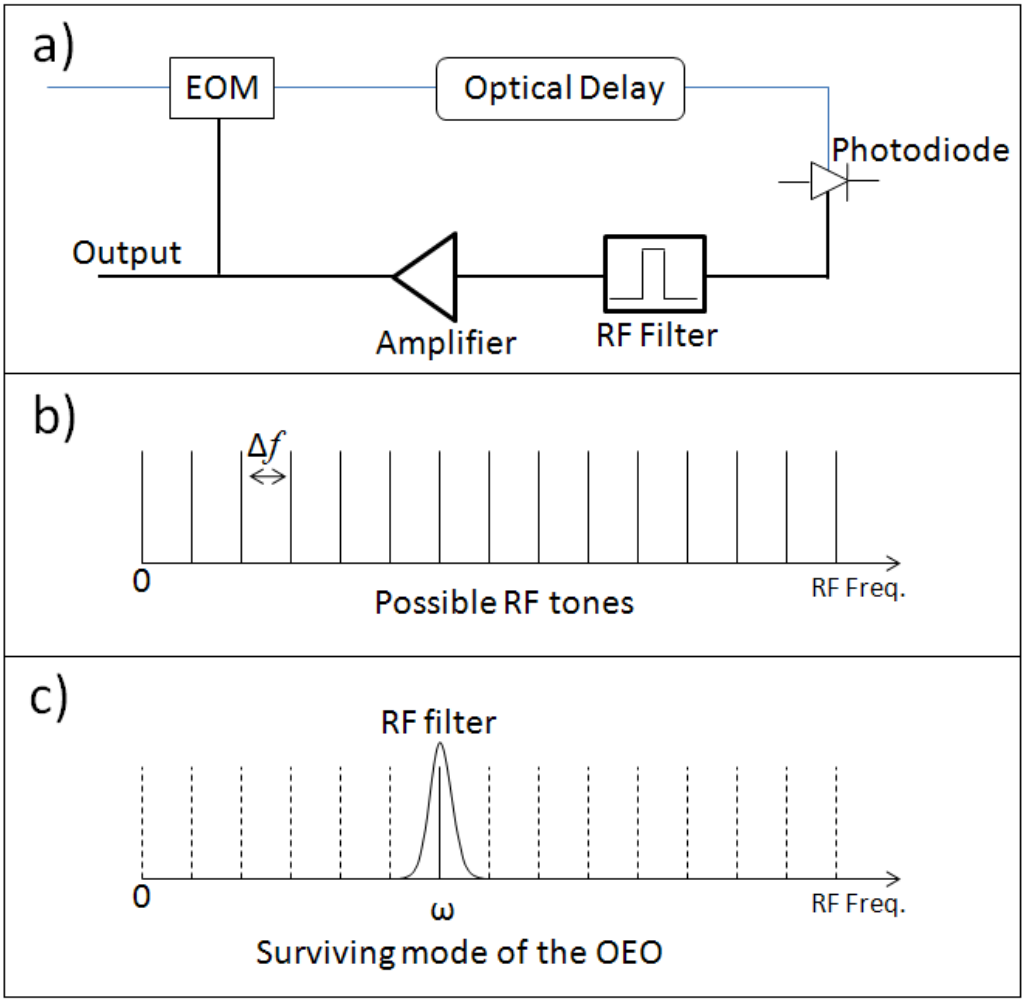

Figure 39: a: standard OEO scheme with RF filter, b: supported RF modes (Δf is the beat tone of the adjacent optical modes) by the cavity, c: filtering of one of the RF modes by using an RF filter.

Theory

The standard OEO design shown in Fig.39(a), has an electro-optic modulator (EOM), an optical delay, a photodiode, an RF filter and an RF amplifier. The microwave signal is imposed on the optical beam and the optical delay acts as a microwave energy storage device. Long delay lines are required in order to achieve a high microwave Q, which results in many closely separated

microwave modes. Only frequencies which constructively interfere with themselves after each round trip can oscillate in a cavity. In other words, the total round trip phase has to be modulo 2π.

$$2\pi N = 2\pi f_{mod}\tau \tag{14}$$

where N is an integer, f_{mod} is the oscillation frequency and τ is the total round trip time. The allowed frequencies can be expressed as:

$$f_{osc}(\tau) = \frac{N}{\tau} \tag{15}$$

Fig. 39(b) shows all the supported RF modes where Δf is the supported RF mode separation. A narrow-band RF filter is necessary to filter out the closely separated RF modes in order to obtain stable oscillation. In Fig 39(c), ω is the oscillation frequency which is determined by the RF filter bandpass frequency.

The proposed OEO design with a Fabry-Perot etalon is shown in Fig 40(a). The OEO has an EOM, an etalon as the resonant mode selector, an optical delay line, photodiode and RF amplifier. The supported optical modes are shown in Fig. 40(b). The periodic transmission function of the etalon only allows optical frequencies which are separated by the free spectral range (FSR) of the etalon to oscillate and eliminates the frequencies outside the resonance width.

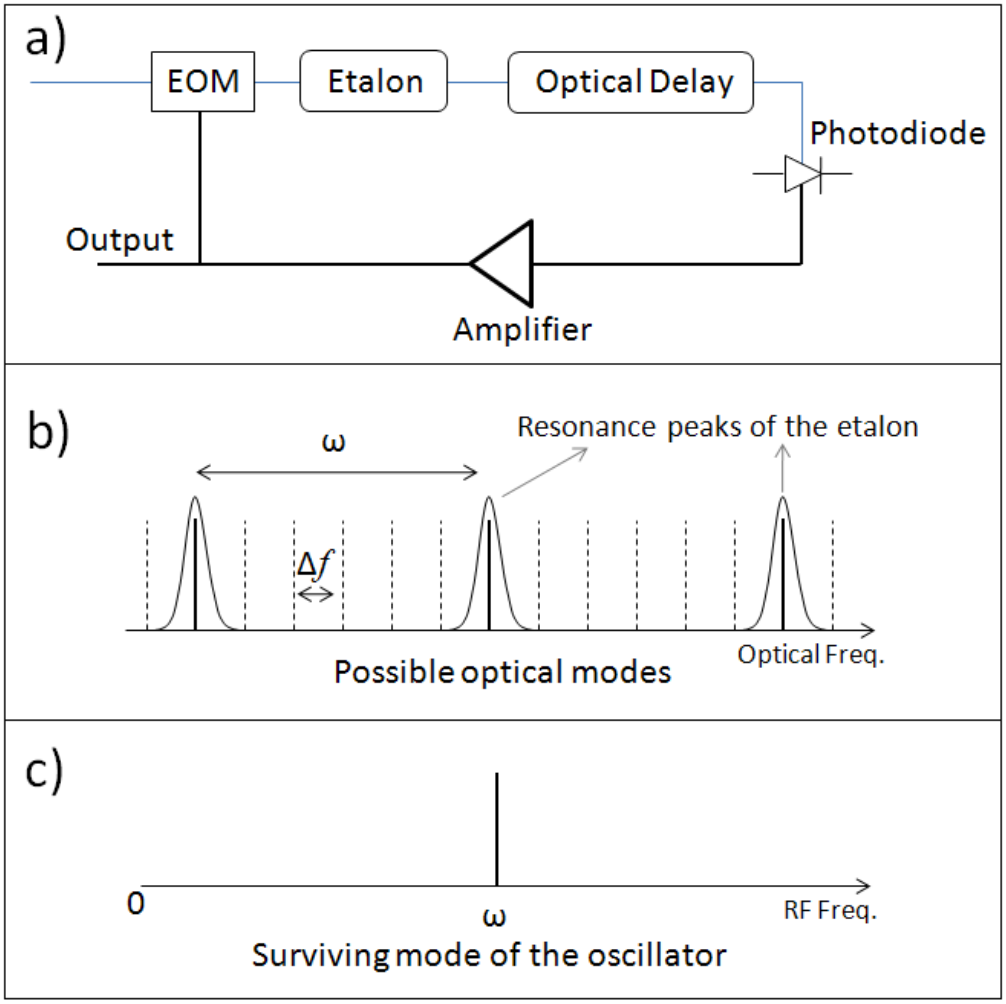

Figure 40: a: OEO scheme with Fabry-Perot etalon, b: filtering of the optical modes with the etalon transmission function, c: beat tone of the optical modes which are separated by ω or free spectral range (FSR) of the etalon.

In this technique, the microwave oscillation frequency is determined by the FSR of the etalon. In Fig. 40(b), Δf represents the optical mode separation and ω is the FSR of the etalon. Since the RF domain signal results from the beating of the optical modes which are separated by ω, only one microwave oscillation mode is allowed in the RF domain and the RF filter is no longer required, as shown in Fig. 40(c).

The difference of the optical frequencies and the optical phases determines the frequency and phase of the RF tone. As there are no optical frequency selective elements inside the standard OEO, the phase-oscillation frequency relationship can be written in a simple form, as given in Eq. 14. But the proposed OEO uses an etalon which has a characteristic phase response therefore an additional term is added to the phase-oscillation frequency relation.

$$2\pi N = 2\pi f_{osc}(\nu, \tau)\tau + \phi(\nu) \tag{16}$$

where ϕ is the additional RF phase from the etalon and ν is the optical frequency. The allowed RF frequencies of the etalon based OEO are a function of the optical frequency and can also be expressed as:

$$f_{osc}(\nu, \tau) = \frac{2\pi N - \phi(\nu)}{2\pi\tau} \tag{17}$$

The phase information of a Fabry-Perot etalon can be extracted from its transmission coefficient which is given by:

$$t(\nu) = \frac{1 - r^2}{1 - r^2 \cdot e^{-i\delta(\nu)}} \tag{18}$$

where r is the amplitude reflection coefficient and δ is the round trip phase shift inside the etalon where $\delta(\nu) = 2\pi\nu/FSR$. The transmission coefficient of the etalon can also be written as

$t(\nu) = |t(\nu)|e^{-i\psi(\nu)}$, where $\psi(\nu)$ is the additional optical phase from the etalon which can be written as:

$$\psi(\nu) = \frac{\delta(\nu)}{2} + \tan^{-1}\left(\frac{r^2 \sin(\delta(\nu))}{1 - r^2 \cos(\delta(\nu))}\right) \tag{19}$$

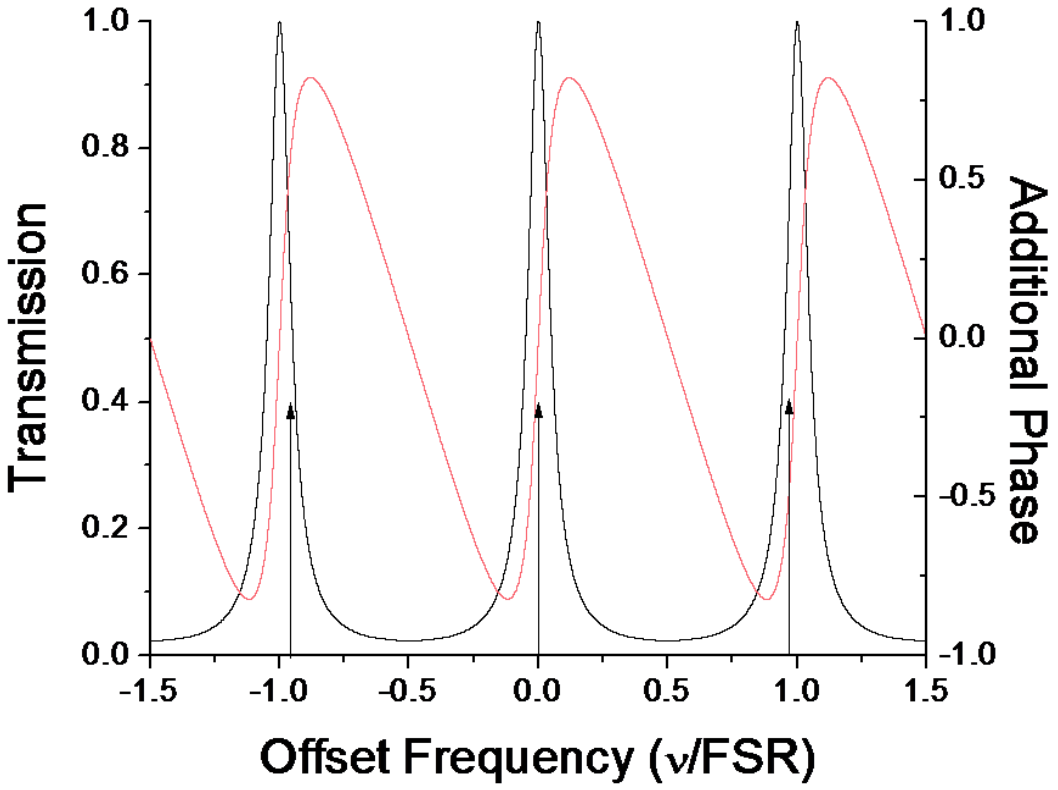

Figure 41: Etalon transmission and phase response characteristics for a 10 Finesse etalon. In the experiments a 1000 Finesse etalon is used, but a Finesse of 10 is used in this figure to illustrate the concept.

Fig. 41 shows the transmission of the etalon which is $t(\nu) \cdot \overline{t(\nu)}$ and the additional transmission phase as a function of input light frequency. The center arrow represents the input light frequency and the left and right arrows are the generated side bands after the intensity modulation.

The frequency of the CW laser (ν) which lies inside the resonance window of the etalon is modulated with the oscillation frequency ($f_{osc} \sim FSR$), resulting in two side bands with frequencies $\nu + f_{osc}$ and $\nu - f_{osc}$, assuming weak modulation. The input CW light can be expressed as:

$$E_{in}(t) = E_{in} \cos(2\pi\nu t) \tag{20}$$

where E_{in} is the amplitude of the input electric field and the static phase is 0. After intensity modulation the total electric field becomes:

$$E_t(t) = E_{-1} \cos(2\pi(\nu - f_{osc}(\nu, \tau))t) + E_o \cos(2\pi\nu t) + E_{+1} \cos(2\pi(\nu + f_{osc}(\nu, \tau))t) \tag{21}$$

assuming absolute phase of the optical and RF signal is 0. As the input light frequency lies within one of the resonance windows of the etalon, and modulation frequency is close to the *FSR*, the side bands are also inside the resonance windows and they experience an additional phase shift as shown in Fig. 41. Mathematically this can be expressed as:

$$E_t^I(t) = E_{-1}^I \cos\big(2\pi(\nu - f_{osc}(\nu,\tau))t + \psi(\nu - f_{osc}(\nu,\tau))\big) \quad (22)$$
$$+ E_o^I \cos\big(2\pi\nu t + \psi(\nu)\big)$$
$$+ E_{+1}^I \cos(2\pi\big(\nu + f_{osc}(\nu,\tau)\big)t + \psi(\nu + f_{osc}(\nu,\tau)))$$

When the optical frequencies are detected with a photodiode, the modulation frequency is regenerated but with an additional phase term from the etalon. The regenerated RF signal can be expressed as:

$$E_{RF}(t,\nu) = E_{RF^1} \cos\Big(2\pi f_{osc}(\nu,\tau)t + \psi(\nu) - \psi\big(\nu - f_{osc}(\nu,\tau)\big)\Big) \quad (23)$$
$$+ E_{RF^2} \cos(2\pi f_{osc}(\nu,\tau)t + \psi(\nu) - \psi(\nu + f_{osc}\,(\nu,\tau)))$$

The above expression consists of two different RF signals with different phases. In Fig. 42, the properties of additional RF phases with respect to the optical frequency are shown for three different cases. The first one is when the total round time (τ) is tuned so that $f_{osc}(\nu,\tau)$ is less than FSR, in the second case, τ is adjusted so that $f_{osc}(\nu,\tau)$ is equal to FSR and in the third case $f_{osc}(\nu,\tau)$ is bigger than FSR. The y-axis represents the optical frequency centered at one of the resonance peaks of the etalon. In the calculations a Fabry-Perot etalon with a FSR of 10.287 GHz and finesse of 1000 is used. The oscillation frequency is detuned $\pm$4 MHz.

When the total round trip time is set to FSR, all the optical tones experiences the same optical phase shift so the additional RF phase shift is 0. But when the total round trip time is detuned form the FSR, all optical tones experiences different optical phases which results in an additional RF phase. The optical tones shown in Fig. 41 have a separation of less than FSR to illustrate the different additional optical phase change.

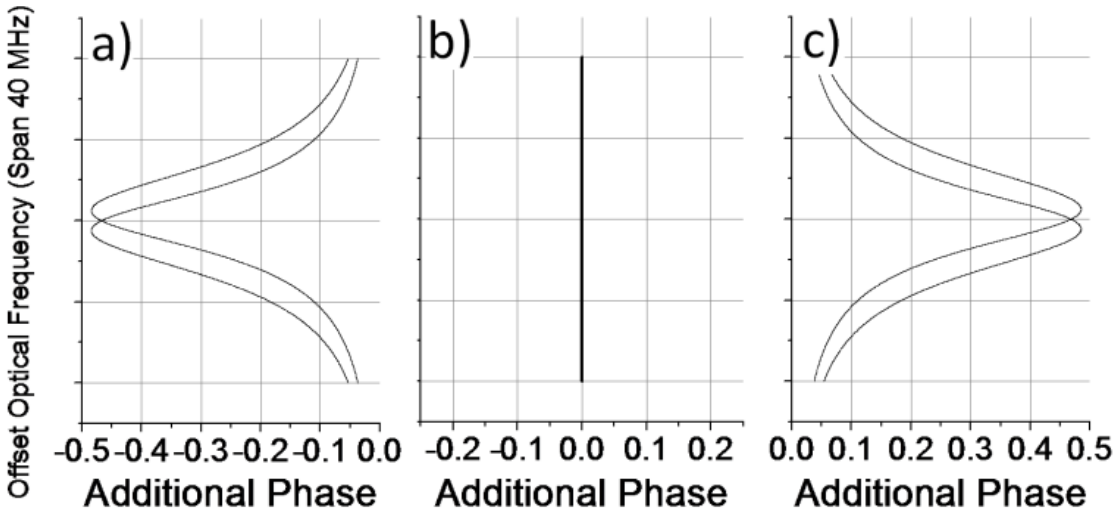

Figure 42: Additional phase from the two RF components, note to the frequency offset. a) when the oscillation frequency, f_{osc}, is less than FSR ($f_{osc} = FSR - 4MHz$), b) the f_{osc} is equal to FSR , c) f_{osc} is bigger than FSR ($f_{osc} = FSR + 4MHz$).

The two RF tones with different phases can be expressed in the form of a single term as:

$$E_{RF}(t,\nu) = E_{RF}\cos\big(2\pi f_{osc}(\nu,\tau)t + \phi(\nu)\big)\cdot\cos\big(\varphi(\nu)\big) \qquad (24)$$

where $\phi(\nu)$ is the additional RF phase shift due to the etalon,

$\phi(\nu) = \psi(\nu) - (\psi\big(\nu - f_{osc}(\nu,\tau)\big) - \psi\big(\nu + f_{osc}(\nu,\tau)\big))/2$, $\cos(\varphi(\nu))$ is the RF power cancelation factor, and $\varphi(\nu) = (\psi\big(\nu + f_{osc}(\nu,\tau)\big) - \psi\big(\nu - f_{osc}(\nu,\tau)\big))/2$, assuming no dispersion. The additional phase of the total electric field is shown in Fig. 42.

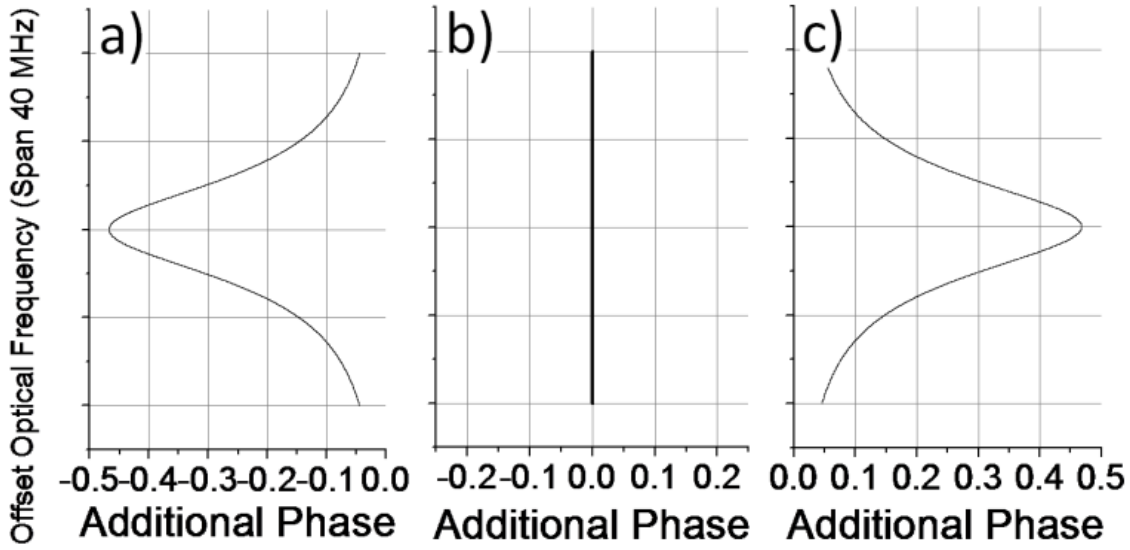

Figure 43: Additional phase from the total RF field ($\phi(\nu)$). a) $f_{osc} = FSR - 4\ MHz$, b) $f_{osc} = FSR$, c) $f_{osc} = FSR + 4\ MHz$

The RF power cancellation factor due to the interference is also shown in Fig. 44 with different detuning frequencies.

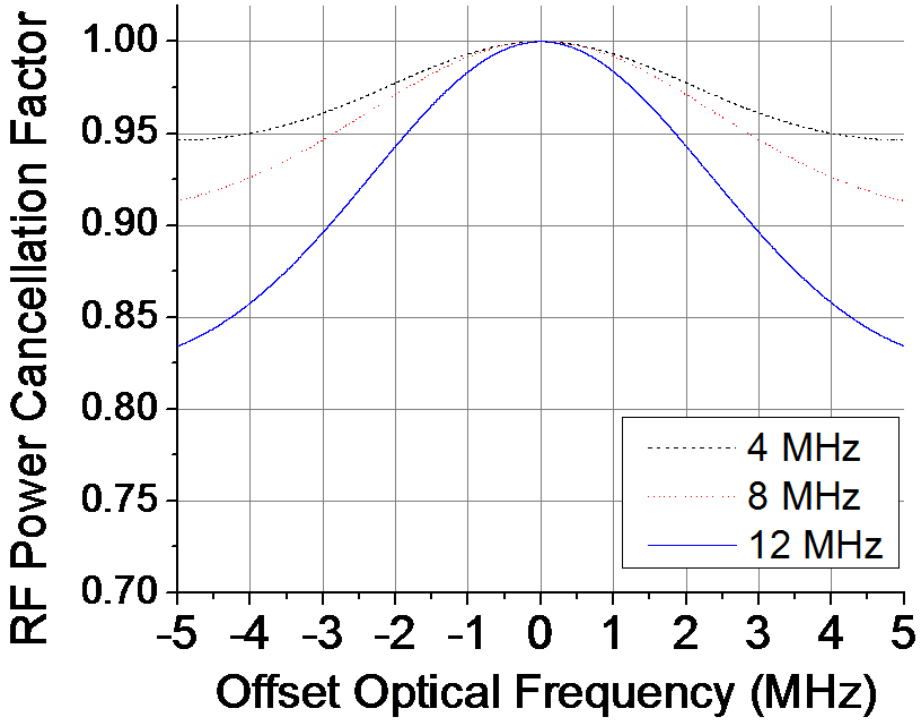

Figure 44: The RF power cancellation factor due to the phase difference of the two RF tones inside the cavity for three different detuning frequencies.

When we insert the additional RF phase from the etalon ($\phi(\nu)$) to the Eq. 17 we get the condition for oscillation frequency:

$$f_{osc}(\nu,\tau) = \frac{2\pi N - \psi(\nu) + \frac{\psi\left(\nu - f_{osc}(\nu,\tau)\right) + \psi\left(\nu + f_{osc}(\nu,\tau)\right)}{2}}{2\pi\tau} \qquad (25)$$

While the oscillator frequency of a standard OEO depends only on the total round trip time, the oscillation frequency of an OEO with etalon depends on both the round trip time and the input

laser frequency. Fig. 45 shows how the oscillation frequency changes with optical frequency and with different total round trip times.

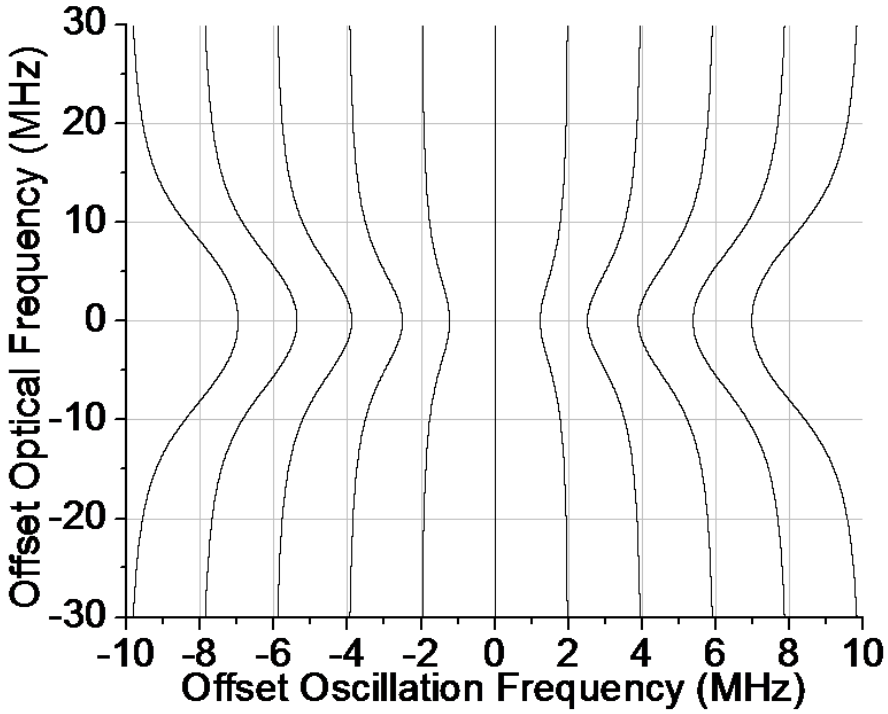

Figure 45: Dependence of the oscillation frequency of the oscillator on the optical frequency for eleven different round trip times. (The center frequency is equal to FSR).

Experimental Setup and Results

A schematic of the OEO with the Fabry-Perot etalon is shown in Fig. 46. A 1550 nm CW laser is used as the light source. The optical frequency of the CW laser can be tuned by applying an external voltage. The output of the CW laser is amplified and sent to the electro-optic modulator (EOM) which is biased at quadrature. A 1000 finesse curved-curved Fabry-Perot etalon with 10.287 GHz free spectral range (FSR) is used as the mode selector. The etalon's stability is very critical as it becomes the frequency reference in the OEO. The etalon is made of ultralow

expansion quartz and is sealed, so it is less susceptible to environmental changes, such as temperature or air pressure. The full width half maximum (FWHM) of the etalon resonance is 10 MHz. The fiber to fiber insertion loss of the etalon is only 0.8 dB. A total optical delay of 10 meters is employed in order to achieve sufficient electrical supermode suppression. The photodiode has 16 GHz bandwidth with 0.8 A/W responsivity, and is followed by a 40 dB gain RF amplifier, after an RF phase shifter. A 10 dB output coupler is used to extract the RF power and the remaining power is fed back to the EOM.

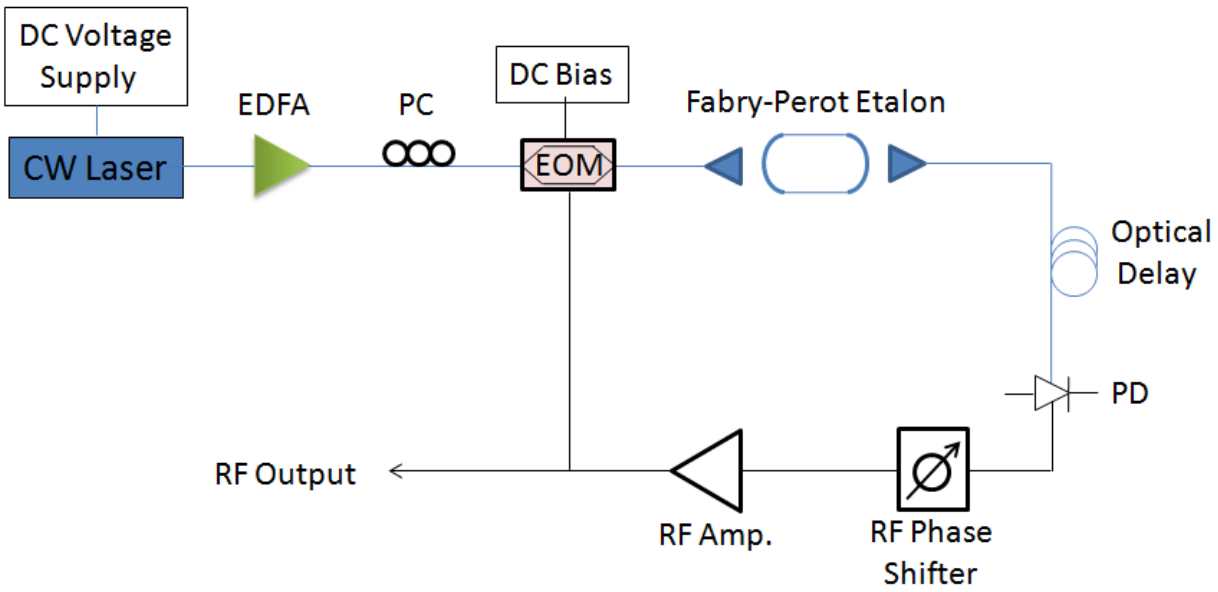

Figure 46: A schematic of the OEO with Fabry-Perot etalon setup. EDFA: Erbium Doped Fiber Amplifier, PC: polarization controller, EOM: electro-optic modulator, PD: photodiode, RF. Amp.: RF. Amplifier.

The optical frequency dependency of RF oscillation is first investigated by changing the total round trip time(τ) with the RF phase shifter for three different cases: $f_{osc} < FSR$, $f_{osc} = FSR$

and $f_{osc} > FSR$. As the optical frequency is tuned across the resonance window, the RF frequency is recorded as a spectrogram as shown in Fig. 47. The results are consistent with numerical simulations shown in Fig. 45.

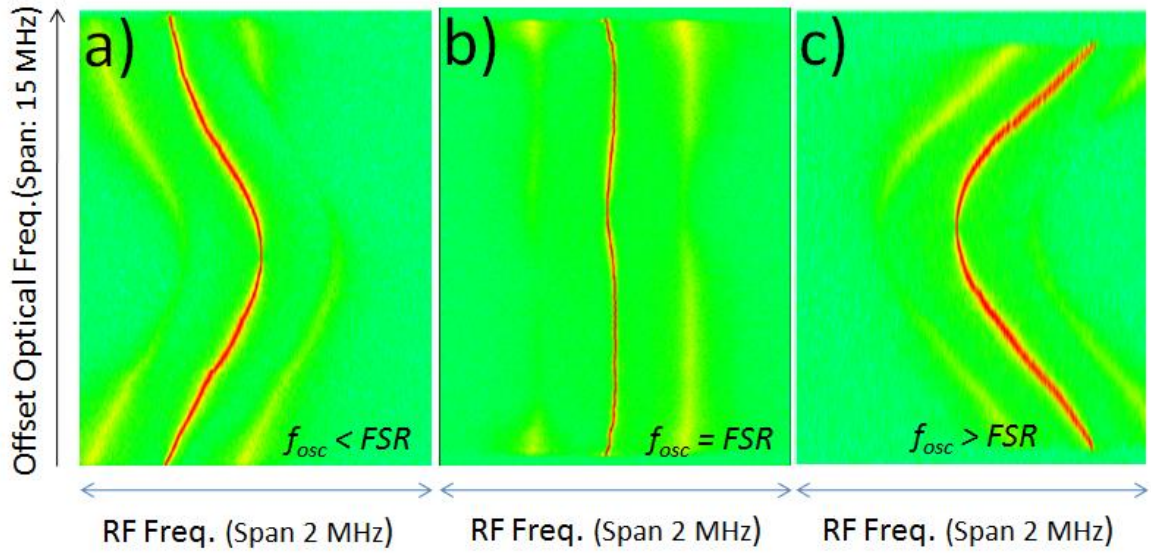

Figure 47: Spectrogram of oscillation frequency change with optical frequency. a) for $f_{osc} < FSR$, b) $f_{osc} < FSR$ and c) $f_{osc} > FSR$.

It must be noted that no optical to RF frequency mapping is observed when the oscillation frequency is equal to the FSR. Also, the phase noise is observed to drop when the optical frequency is at the peak of the etalon resonance.

The RF spectrum of the OEO is shown in Fig. 48. The RF power of the tone centered at 10.287 GHz is ~+12 dBm. No mode hopping is observed during the experiment.

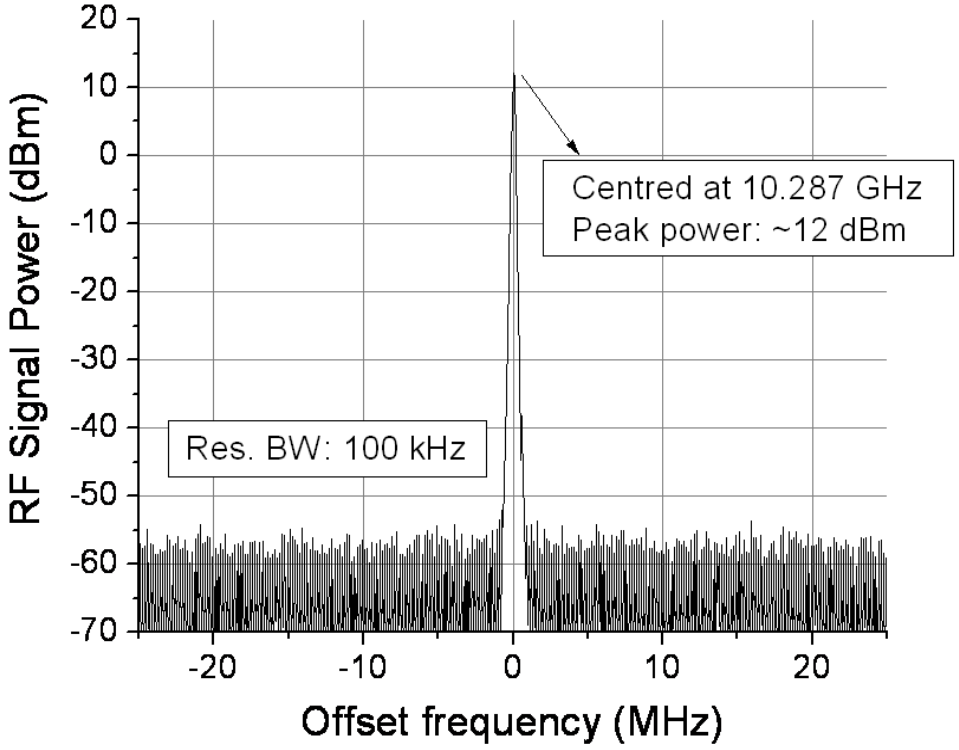

Figure 48: RF spectrum of OEO tone centered at 10.287 GHz.

The phase noise and RF frequency stability of the OEO are also measured and compared with the standard OEO. In the standard OEO, the Fabry-Perot etalon is replaced by an RF filter while keeping all other components and parameters constant. The RF filter used in the experiment has a 3 dB bandwidth of 13 MHz, centered at 10.287 GHz and has an insertion loss of ~5 dB. The total optical delay is kept constant by adding an appropriate amount of fiber to the cavity.

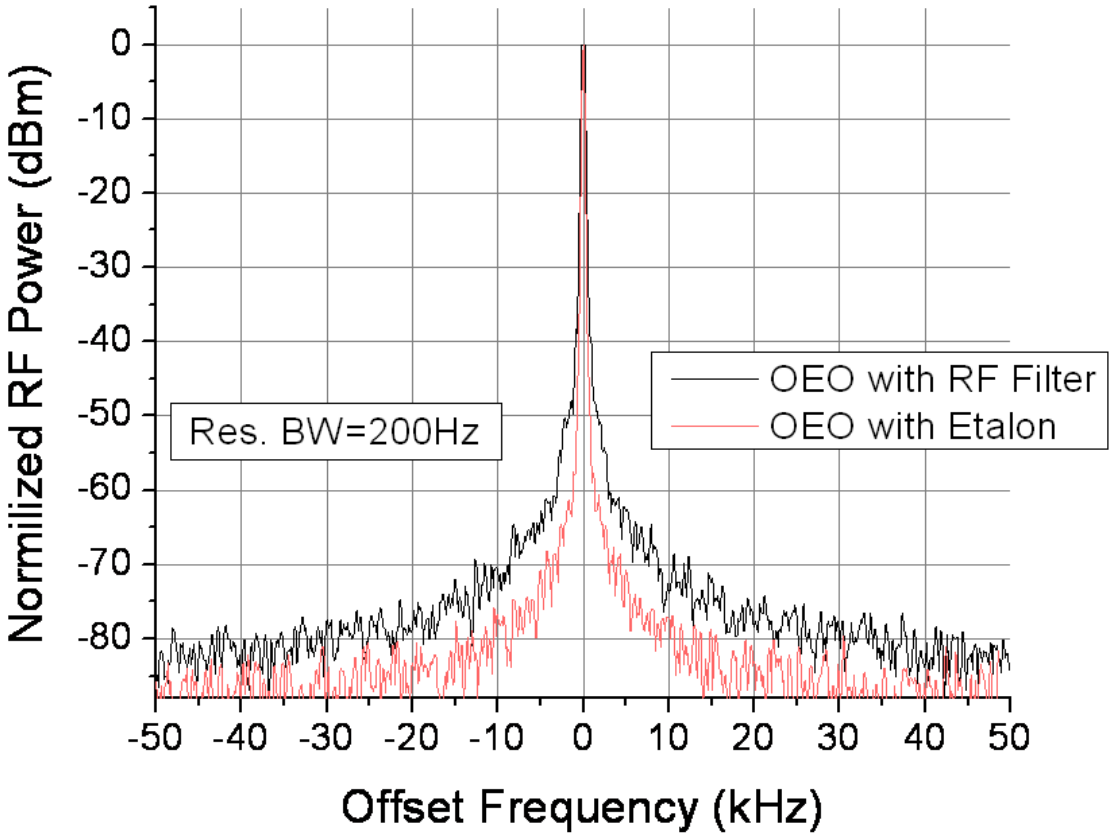

Figure 49: Comparison of phase noise of the OEO with RF filter and with etalon (Normalized power).

A comparison of the phase noise of an OEO with an RF filter, and an OEO with an etalon is shown in Fig. 49. At close offset frequencies, the OEO with the RF filter has 5-10 dB lower signal-to-noise ratio (SNR) than the OEO with Fabry-Perot etalon. The SNR at 10 kHz offset from the carrier for the OEO with Fabry-Perot etalon is 100 dBc/Hz.

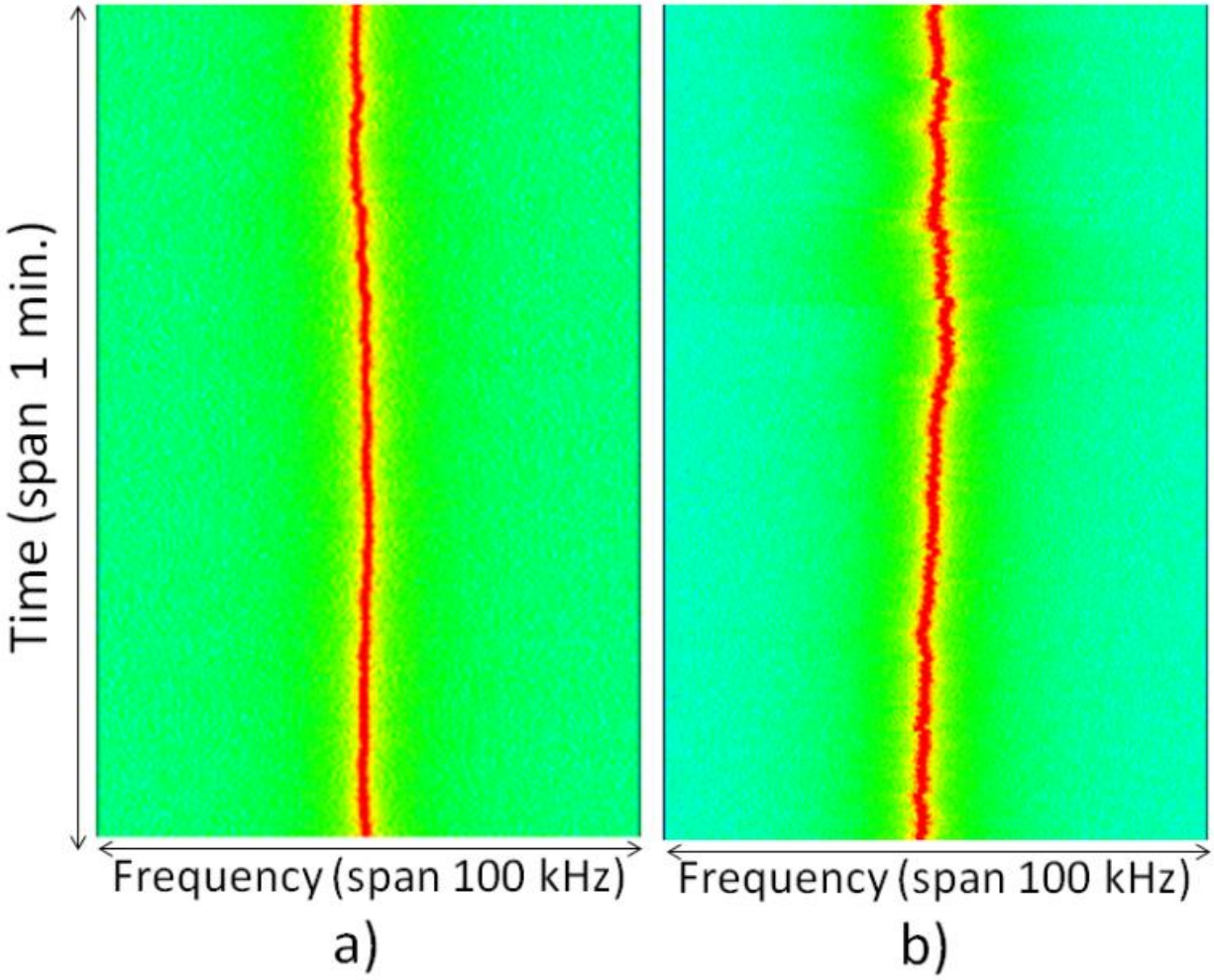

Figure 50: Spectrogram of the RF traces over 1 min. of OEO with Fabry-Perot etalon (a) and with RF filter (b).

The RF stability of the oscillation frequency is also measured using a real time RF spectrum analyzer in the spectrogram mode and compared for the two OEO designs (Fig. 50). The RF frequency stability over 1 min for the OEO with the Fabry-Perot etalon is 2.6 kHz whereas the stability for the standard OEO is 5.75 kHz. Fig. 50 clearly shows the improved stability due to the ultra-stable Fabry-Perot etalon used as the filter.

Low Noise Optically Tunable OEO

When the total round trip time is set such that the oscillation frequency is mismatched the FSR range, the oscillation frequency can be fine-tuned by the optical frequency. But the noise of the OEO is high when the optical frequency is away from the resonance peak, which makes it impractical to tune the oscillation frequency. In the previous section a standard Mach-Zehnder modulator is used which creates double side bands and hence two different RF signals with different phases. When the optical frequency does not match the resonance peak, two RF tones with different phases inside the cavity create instabilities and also decrease the RF tone power which results in a higher phase noise. To decrease the phase noise and to make the OEO tunable (in terms of its optical frequency), single side band modulation of the optical signal is implemented.

Different methods can be used to generate single side bands [55]. In our experiment a 10 GHz FSK (Frequency Shift Keying) modulator is used. The modulator has two parallel Mach-Zehnder intensity modulators in each arm and also one additional phase modulator in the upper arm as shown in Fig. 51 (a). In order to generate single bands, the input RF signal is divided into two with one signal sent to the intensity modulator in the lower arm and the other signal sent t o the phase modulator on the upper arm. The modulation creates side bands with a separation of input RF frequency as shown in Fig. 51 (b). The signal coming from the phase modulation has two side bands with a phase difference of π whereas the signal coming from the lower arm (intensity modulation) has side bands with the same phase. When signals from the upper and lower arms combine the resulting is a single side band modulated signal, as shown in Fig. 51 (b).

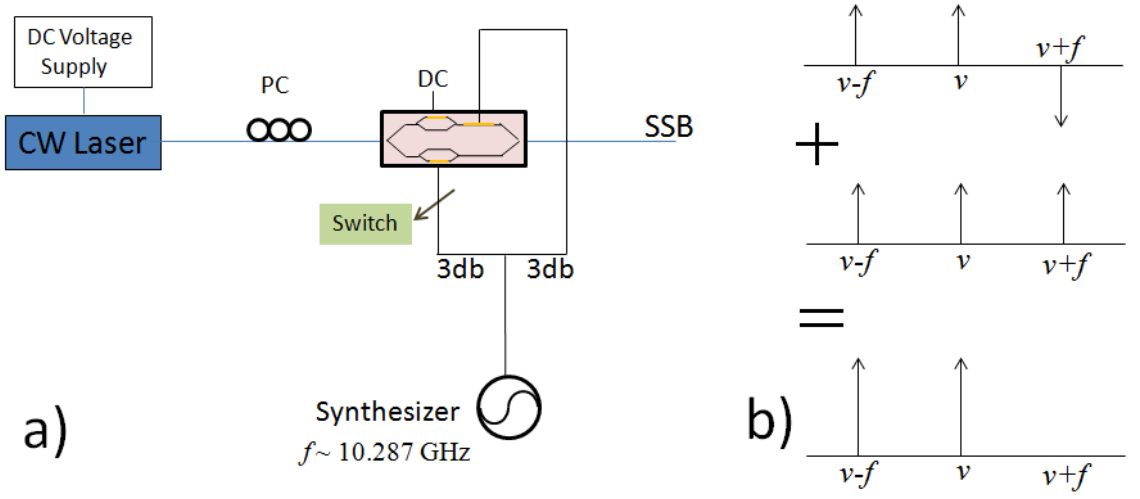

Figure 51: a) Setup for single side band generation. b) Mechanism for single side band generation.

The system is aligned for single optical side band generation using a synthesizer. A switch is also added in the setup to easily switch from single side band modulation mode to double side band modulation.

For the case of an OEO with single side band modulation, Eq. 24 simplifies to:

$$E_{RF}(t,\nu) = E_{RF}\cos\left(2\pi f_{osc}(\nu,\tau)t + \phi(\nu)\right) \tag{26}$$

where $\phi(\nu) = \psi(\nu) - \psi\left(\nu - f_{osc}(\nu,\tau)\right)$. The power cancellation factor vanishes from the equation as there is only one RF tone inside the cavity. Also Eq. 25 simplifies to:

$$f_{osc}(\nu,\tau) = \frac{2\pi N + \psi(\nu) - \psi\left(\nu - f_{osc}(\nu,\tau)\right)}{2\pi\tau} \tag{27}$$

The single side band generation scheme is applied to the etalon based OEO as shown in Fig. 52.

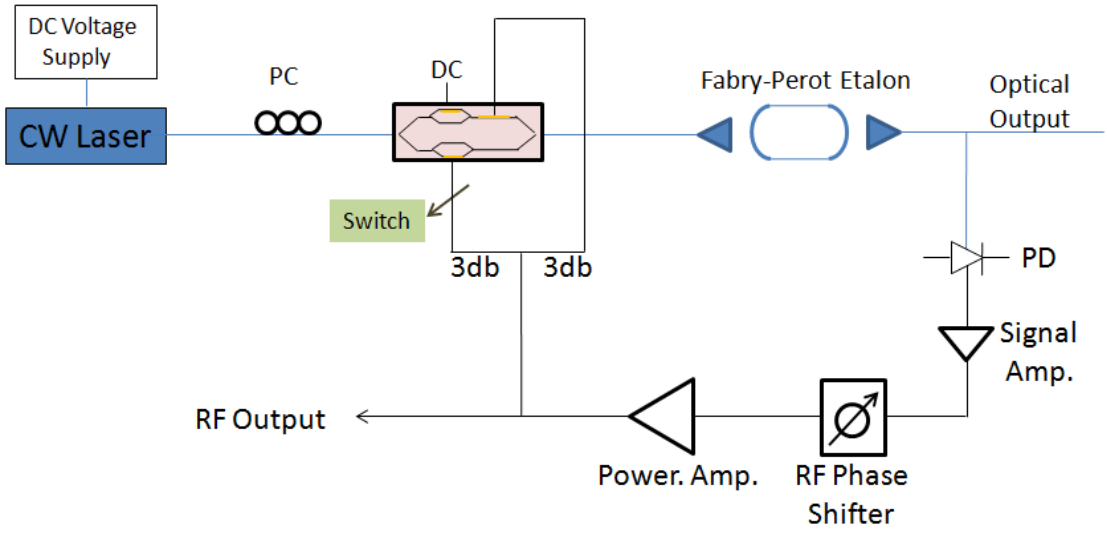

Figure 52: The schematic of the optical single side band OEO with Fabry-Perot etalon. PC: polarization controller, PD: photodiode, Signal Amp.: Signal Amplifier, RF. Amp.: RF. Amplifier.

The FSK modulator has a maximum input power limit of 10 mW and has a 10 dB insertion loss during single side band generation. Therefore, a signal amplifier with 18 dB gain is added to the setup as the gain of the power amplifier is not sufficient to start the oscillation.

The oscillation frequency is chosen to be ~10.291 GHz, which is off by ~4 MHz from the free spectral range of the cavity, while the optical frequency is ~4 - 5 MHz off from the resonance peak. The OEO is initially driven in the dual optical side band modulation mode. The optical spectrum and the corresponding RF spectrum are shown in Fig. 53 and Fig. 54.

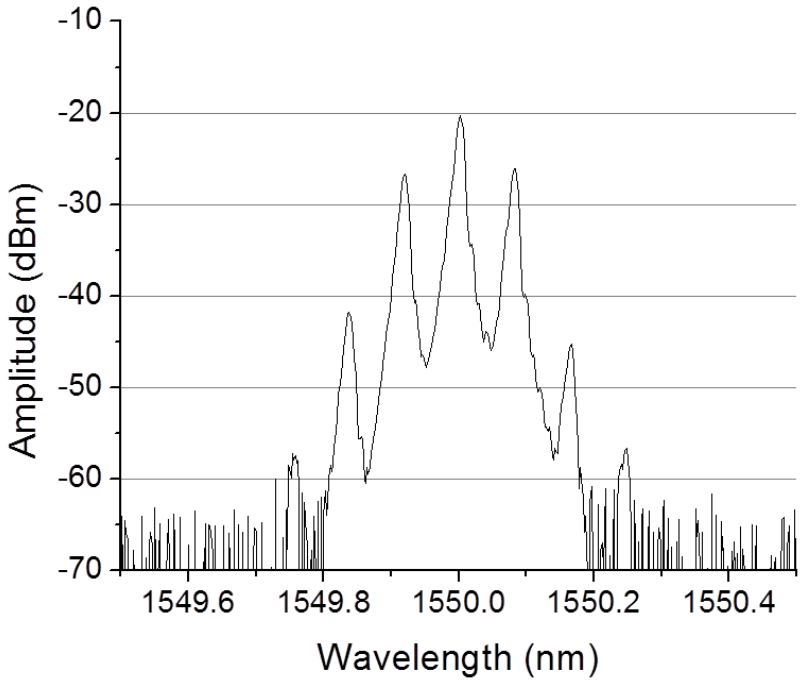

Figure 53: The dual side band optical spectrum of the OEO. and (b) the RF spectrum of the OEO.

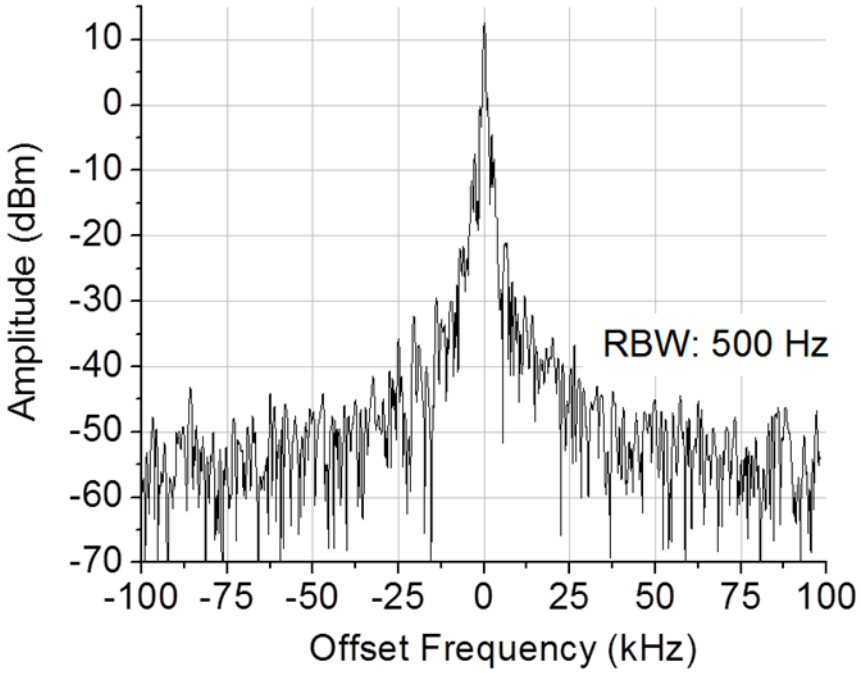

Figure 54: The RF spectrum of the OEO with the dual side band operation

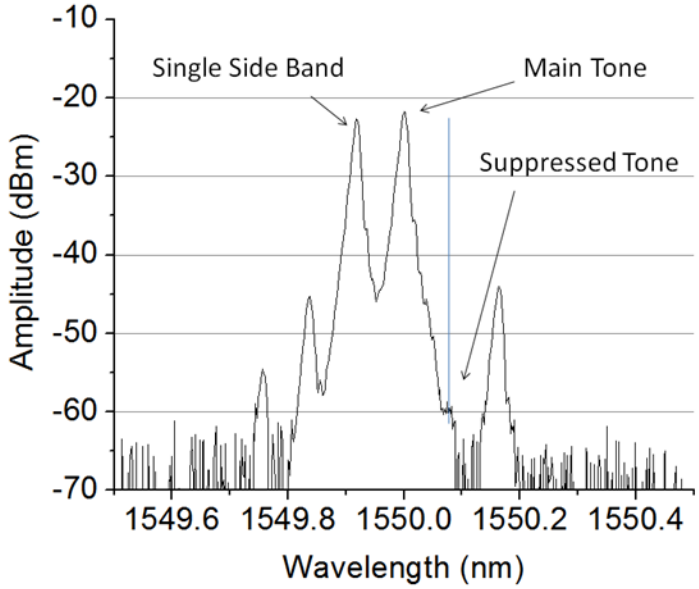

Figure 55: The single side band optical spectrum of the OEO.

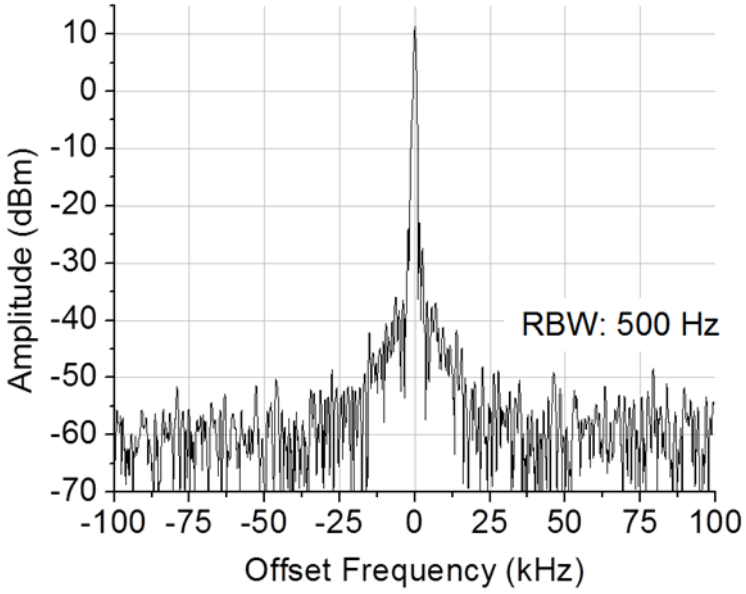

Figure 56: The RF spectrum of the OEO with the single side band operation.

Fig. 53 shows the typical optical dual side band spectrum with side bands separated by the oscillation frequency and Fig. 54 shows the RF spectrum of the oscillation tone, centered at 10.291GHz.

When the OEO is operated with single optical side band modulation, the optical spectrum shows a ~ 38 dB suppression of the first harmonic from the main tone (Fig. 55). The RF spectrum analyzer trace is shown in Fig. 56. A 10 – 20 dB decrease in noise is achieved with the optical signal side band generation.

For lowest noise performance, the OEO should be run at the FSR frequency but a low noise optically tunable OEO can also be achieved by using optical single side band generation and tuning the oscillation frequency slightly from the FSR by using an RF phase shifter.

Conclusion

In this work, a new optoelectronic oscillator (OEO) scheme is introduced which uses an ultra-stable 1000 finesse Fabry-Perot etalon as the oscillator mode selector. The selection of the modes is performed in the optical domain by the use of the periodic etalon transfer function. The OEO oscillation frequency is defined by the free spectral range of the etalon. The dependency of the RF frequency on the input optical frequency is analyzed theoretically and is demonstrated experimentally. The performance of the new OEO with Fabry Perot etalon is compared with the standard OEO design that uses an RF filter. When all other parameters are kept constant except the mode selector, the OEO with the Fabry-Perot etalon results in better phase noise performance and higher RF frequency stability. An optically tunable OEO can also be implemented by simply tuning the oscillation frequency slightly from the FSR by using an RF phase shifter. When the

oscillation frequency is detuned from the FSR of the etalon, the noise increases with a standard optical dual side band generator intensity modulation. However, a single side band modulation technique has been experimentally implemented to achieve low noise operation with optical frequency tunability.

The resonance bandwidth of the etalon can be narrowed easily by using a higher finesse etalon which will allow longer optical fiber delays with higher Q to be used in the OEO. When higher finesse etalons are used, a CW laser frequency locking system such as Pound-Drever-Hall (PDH) method [23] may be required to lock the laser frequency to the etalon resonance peak. Also optical single side band generation can be used in any OEO in order to overcome the chromatic-dispersion effects if the total dispersion is high.

CHAPTER 7: HIGH RESOLUTION OPTICAL FREQUENCY STABILITY MEASUREMENT REFERENCED TO AN ULTRA-STABLE ETALON

The measurement of the optical frequency stability of a laser can provide useful information about the light source performance. Optical spectrum analyzers can be used for this purpose, but they cannot simultaneously offer high resolution measurements with fast scan rates. Therefore, the photodetected heterodyne mixing of two independent laser sources is generally used to study the optical frequency stability of one laser with respect to the other on an RF spectrum analyzer. The heterodyne beat tone is equal to the difference in optical frequencies of the two laser sources. However, as the instability of the beat tone can be due to the drift or fluctuations of any of the two light sources, hence reliable measurements cannot be obtained unless the reference laser is significantly more stable than the laser under test [54,56]. In the past, lasers with high optical frequency stability have been demonstrated by stabilizing the optical beam to a high finesse etalon via the Pound-Drever-Hall technique [23], by locking the optical frequency to an atomic resonance [57], or by locking the carrier envelope offset frequency of a mode-locked laser [58].

The generation of low noise RF tones by using optoelectronic oscillators (OEOs) with different architectures has been reported in [59-63]. The standard OEO consists of a seed laser source followed by a modulator. The modulated signal is photodetected, amplified, and filtered by an RF filter and then sent back to the modulator to complete the loop. A refractive index measurement method by using an OEO was also proposed and shown experimentally in [64]. Recently, another OEO setup which uses a Fabry-Perot etalon as the mode selector instead of an RF filter was introduced [65]. The etalon based OEO architecture has great potential in

generating ultra-low noise RF tones because the etalons can have ultra-high stability and narrow resonance width. For example an etalon with 5 kHz resonance width and 63 mHz/s linear drift was reported recently [66].

In this paper, a method for directly mapping the drift and fluctuations in the optical frequency of a laser to the RF domain is demonstrated using an etalon based optoelectronic oscillator. The etalon introduces an additional phase to the optical tones, depending on the input CW light frequency, which causes a change in the accumulated RF frequency phase and thus the RF oscillation frequency. The drift and fluctuation of the input light frequency can be measured with high precision from the offset RF frequency. Moreover, since the Fabry Perot Etalon is sealed and made of ultralow expansion quartz, it is stable and measurements are accurate and repeatable. By using this technique, the optical frequency stability of a CW laser is measured with ~3.5 kHz optical frequency resolution at update rates of 90 Hz.

Theory

In the etalon based OEO architecture [65], the periodic transmission function of the etalon only allows the optical frequencies which are separated by the free spectral range (FSR) to oscillate, and eliminates the frequencies that lie outside the resonance width. In this technique, the microwave oscillation frequency is determined by the FSR of the etalon. In Fig. 57(a) and (b), $\Delta\nu$ represents the optical mode separation and ω is the FSR of the etalon. Since the RF domain signal results from the beating of the optical modes which are separated by ω, only one microwave oscillation mode is allowed in the RF domain as seen in Fig. 57(c).

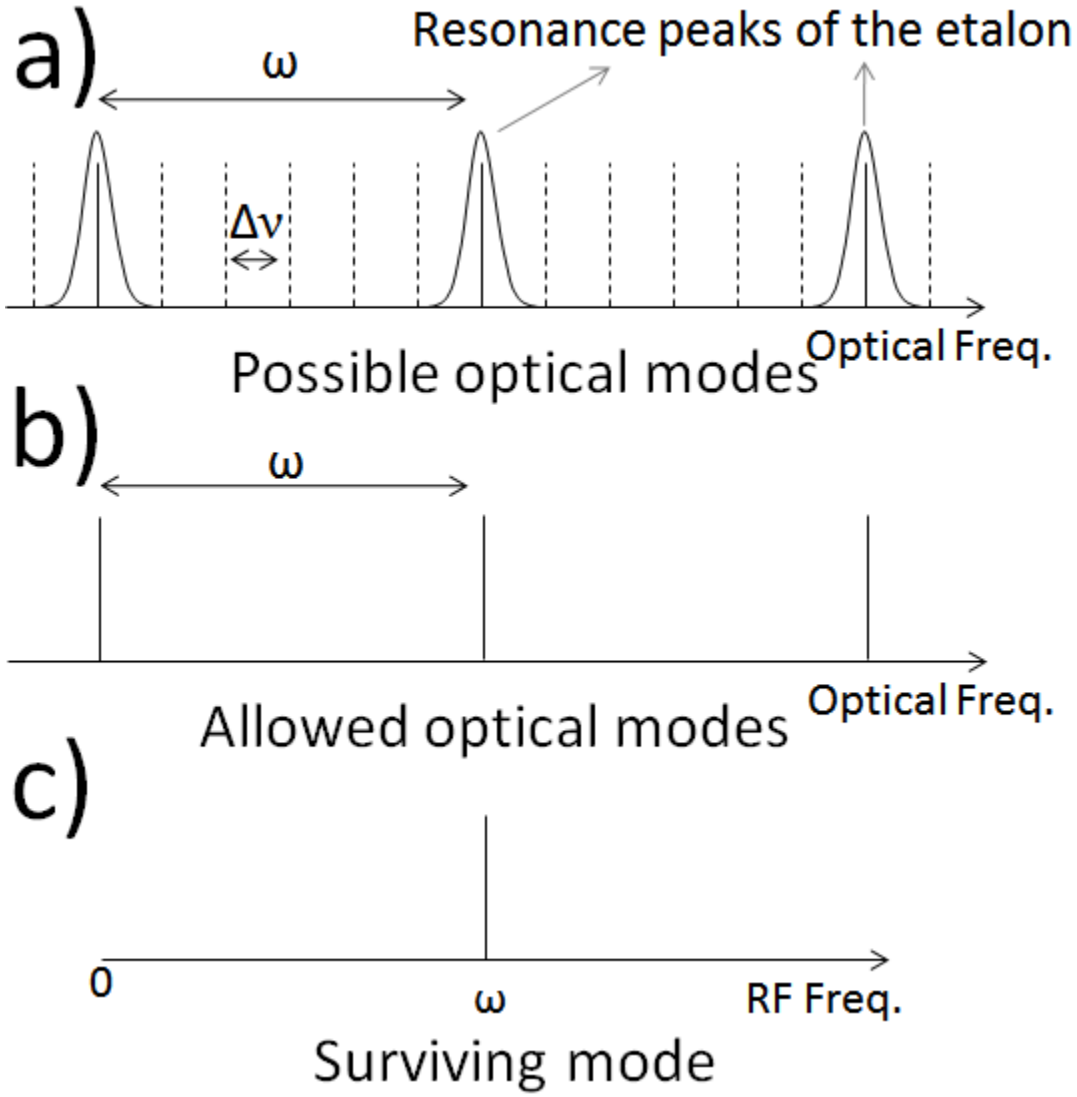

Figure 57: (a) Filtering of the optical modes with the etalon transmission function, (Δν is the cavity fundamental frequency), (b) after filtering, only the modes inside the resonance width survive. (c) beat tone of the optical modes separated by ω or free spectral range (FSR) of the etalon.

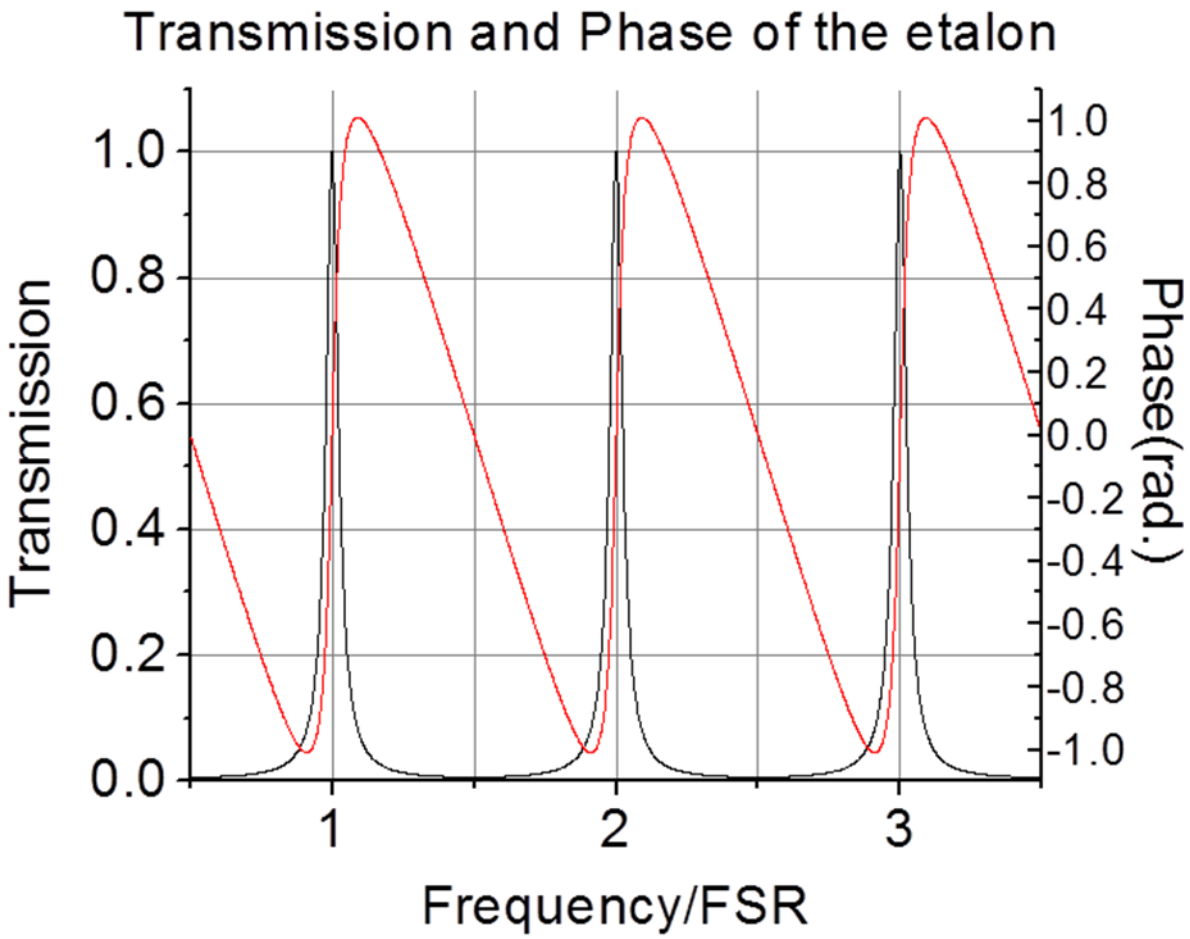

Figure 58: Etalon transmission function and transmitted light phase properties.

With the classical OEO setup, the oscillation frequency is independent of optical frequency and can be written as:

$$2\pi N = 2\pi f_{osc}(\tau)\tau \tag{28}$$

Where f_{osc} is the oscillation frequency, τ is the round trip time and N is an integer. In the etalon based OEO there is an additional RF phase term because of the etalon. The new phase relation can be written as:

$$2\pi N = 2\pi f_{osc}(\tau,\nu)\tau + \varphi(\nu) \tag{29}$$

where, $\varphi(\nu)$ is the additional RF phase term due to the etalon.

After the intensity modulator the total electric field can be written as (assuming weak modulation):

$$E(t) = E_{-1}\cos(2\pi\nu_{-1}t) + E_0\cos(2\pi\nu_0 t) + E_{+1}\cos(2\pi\nu_{+1}t) \tag{30}$$

where, E_{-1},E_0 and E_{+1} are the amplitudes of the optical tones and $\nu_{-1}= \nu_0-f_{osc}$ and $\nu_{+1}= \nu_0+ f_{osc}$ are the frequencies of generated optical tones. The input laser frequency, ν_0, lies within one of the resonance windows and as the f_{osc} is close to the FSR other optical tones are also inside resonance windows. When an optical tone pass through the resonance it experiences an additional phase as shown in Fig. 58 which is given by:

$$\psi(\nu) = \frac{\delta(\nu)}{2} + \arctan\left(\frac{r^2\sin(\delta(\nu))}{1-r^2\cos(\delta(\nu))}\right) \tag{31}$$

where $\delta(\nu)$ is the round trip phase shift inside the etalon, and r is the amplitude reflection coefficient. The total electric field after passing through the etalon can be expressed as:

$$E'(t) = E'_{-1}\cos(2\pi\nu_{-1}t + \psi(\nu_{-1})) + E'_0\cos(2\pi\nu_0 t + \psi(\nu_0)) + E'_{+1}\cos(2\pi\nu_{+1}t + \psi(\nu_{+1})) \tag{32}$$

This will yield an RF tone, given by:

$$E_{RF}(t) = E_{RF}\cos\left(2\pi f_{osc}(\tau,\nu)t + \varphi(\nu)\right)\cos\left(\theta(\nu)\right) \tag{33}$$

where, $\varphi(\nu)$ is the additional phase shift due to the etalon ($\varphi(\nu)=(\psi(\nu_{+1})-\psi(\nu_{-1}))/2$) and $\theta(\nu)= \psi(\nu_0)-(\psi(\nu_{+1})-\psi(\nu_{-1}))/2$. By using the additional phase the oscillation frequency can be written as:

$$f_{osc}(\tau,\nu) = \frac{N}{\tau} + \frac{\psi(\nu - f_{osc}(\tau,\nu)) - \psi(\nu + f_{osc}(\tau,\nu))}{4\pi\tau} \tag{34}$$

Note that, without the etalon, the oscillation frequency is independent of the optical frequency and only depends on the total round trip time as shown in Eq.28. However, when the etalon is inserted into the system, the oscillation frequency of the OEO depends on both, the total round trip time and the optical frequency as shown in Eq. 34. By adjusting the optical frequency and total round trip time, a linear regime between optical frequency of the seed laser and the generated RF tone can be realized. Therefore one can use this effect to characterize frequency

fluctuations of the seed laser by measuring the frequency fluctuation of the RF tone generated by the OEO.

Experiment

To experimentally demonstrate the above concept, a narrow linewidth (<1 kHz) CW laser is used in the setup shown in Fig.59. By tuning the frequency control voltage, the optical frequency of the laser is shifted to a transmission resonance window of the etalon. The output of the CW laser is passed through an acousto-optic modulator and directed to the electro-optic modulator (EOM) which is biased at quadrature. The Fabry-Perot etalon (Advance Thin Films) has two curved mirrors with 50 cm radius, a free spectral range of 10.287 GHz, and finesse of 1000 which corresponds to a resonance width of 10 MHz. The fiber-to-fiber insertion loss of the etalon is 0.8 dB. The etalon is sealed to increase the stability. It is made of ultra-low expansion (ULE) quartz with an expansion coefficient of 30 ppb K^{-1}. With temperature stabilization and under vacuum, ULE Fabry Perot etalons can reach exceptional stability [66]. The photodiode has a bandwidth of 16 GHz and a responsivity of 0.8 A/W. It is followed by an RF phase shifter and a 40 dB gain RF amplifier. A 10 dB output coupler is used to extract the RF signal and is analyzed using a real time RF spectrum analyzer (RT-RFSA); the remaining 90% of the RF power is fed back to the EOM. The overall cavity length of the OEO is ~10 meters.

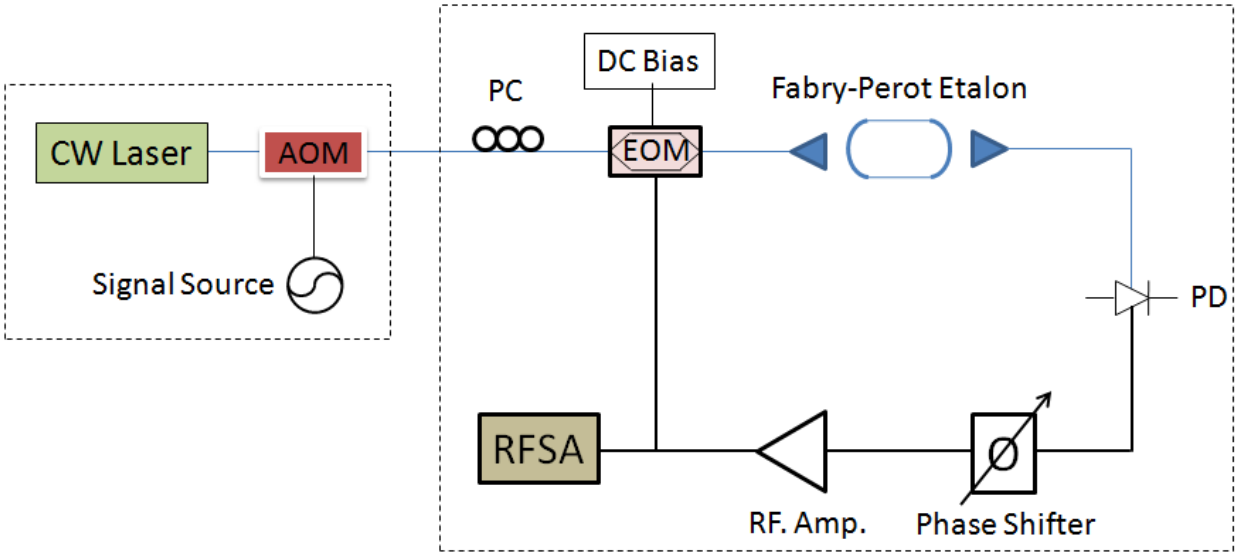

Figure 59: Experimental setup. The first part consists of the laser under test and calibration and the second part is the measurement setup. AOM: acousto-optic modulator, PC: polarization controller, EOM: electro-optic modulator, PD: photo-detector, RF. Amp: RF amplifier, RFSA: radio frequency spectrum analyzer.

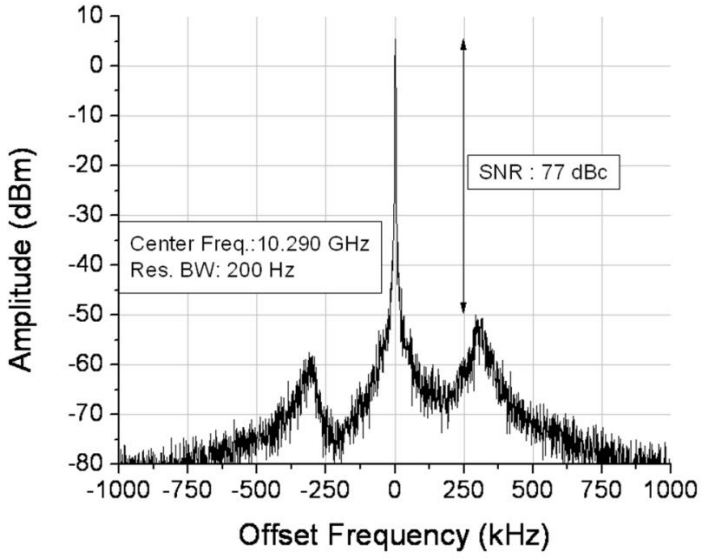

Figure 60: The RF tone of the detuned optoelectronic loop.

When the oscillation frequency is set to the etalon FSR using the RF phase shifter, the optical side bands generated by the intensity modulation are symmetrical with respect to the resonances and experience the same additional etalon optical phase shift, and thus the optical frequency shift does not map to the RF domain. In order to break the symmetry, the total RF phase is detuned using the phase shifter, resulting in a shift in the center RF oscillation frequency from 10.287 GHz to 10.290 GHz.

Fig. 60 shows a typical RF spectrum of the oscillator with detuning. In order to observe the mapping of the optical domain to the RF domain, the optical frequency is linearly swept through the resonance. The simulation and experimental results are given in Fig. 61(a) and (b), respectively. The measurement range is limited by the linear-like regime which is ~ 5 MHz as shown in Fig. 61(a) and 61(b). The mapping of the optical frequency change to the RF domain is shown by modulating the optical frequency using an acousto-optic modulator driven by a linearly swept RF frequency, Fig.62.

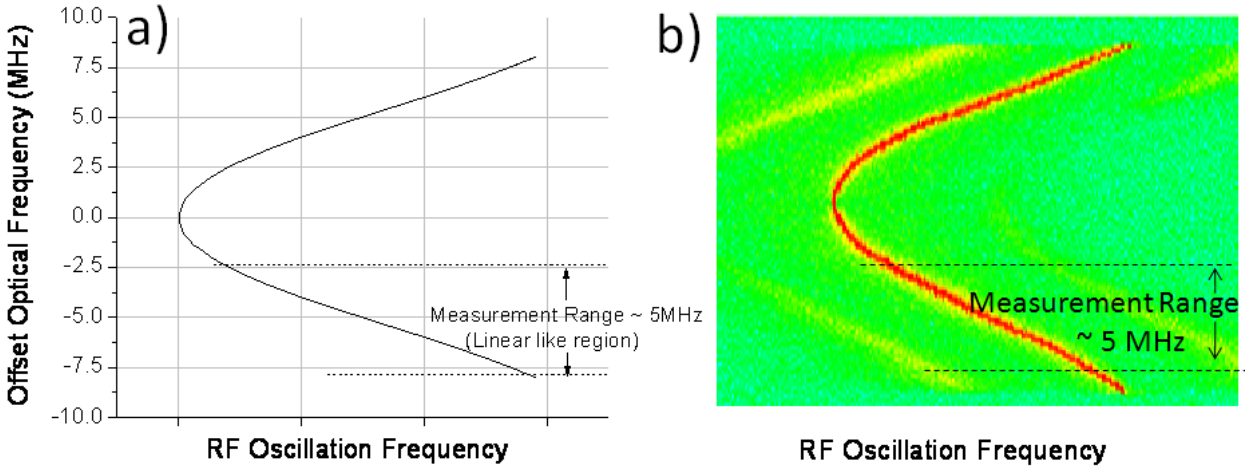

Figure 61: Simulation results for mapping the optical frequency change to the RF domain and (b) experimental results.

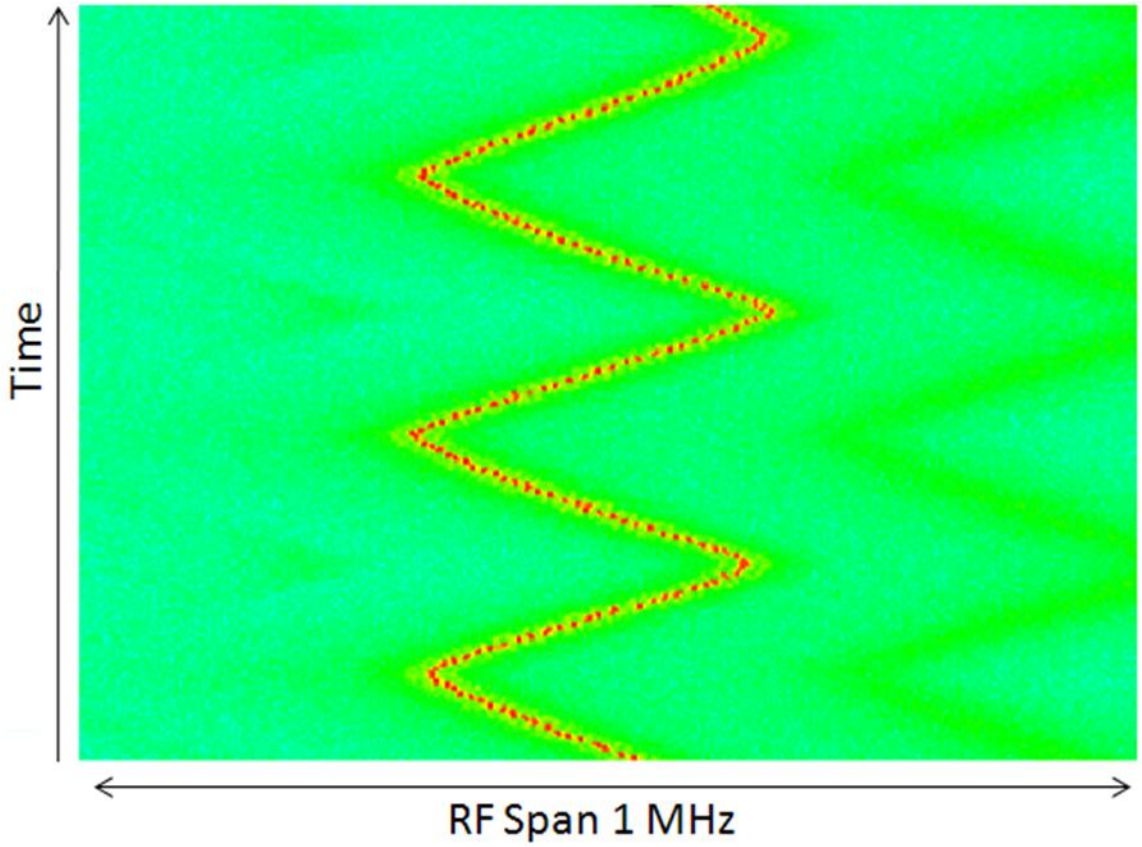

Figure 62: Spectrogram of the RF tone when the laser frequency is varied using an acousto-optic modulator.

The performance of the CW laser is analyzed during the warm up time and also after warm up. Fig. 63 (a) shows the frequency drift during the warm up process and a sudden change in the optical frequency is observed. The short term frequency fluctuations of the laser are also measured after warm up. A calibration is necessary in order to get the correct conversion from the RF domain to the optical domain. For this purpose, the optical frequency is shifted by 5 MHz using the acousto-optic modulator and the corresponding RF frequency shift is measured and

found to be 0.7 MHz, shown in Fig. 63 (b). This results in a conversion factor of $\Delta v/\Delta f$=7.14, where Δv is the optical frequency shift and Δf represents the corresponding shift in the RF frequency. The conversion factor also represents the *sensitivity* of the measurement system; the smaller the conversion factor, the larger the sensitivity of the system to optical frequency changes.

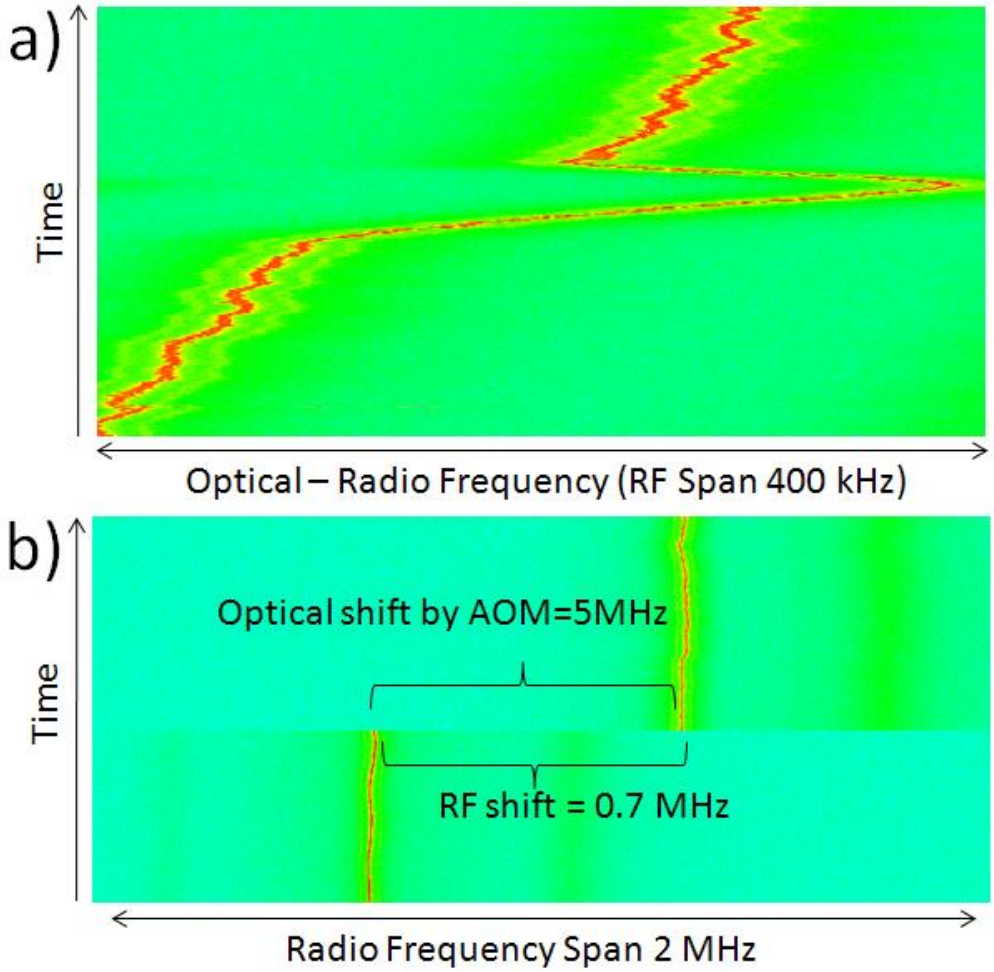

Figure 63: (a) Optical frequency spectrogram during the warm up of the CW laser, (b) Calibration of the measurement system using an acousto-optic modulator.

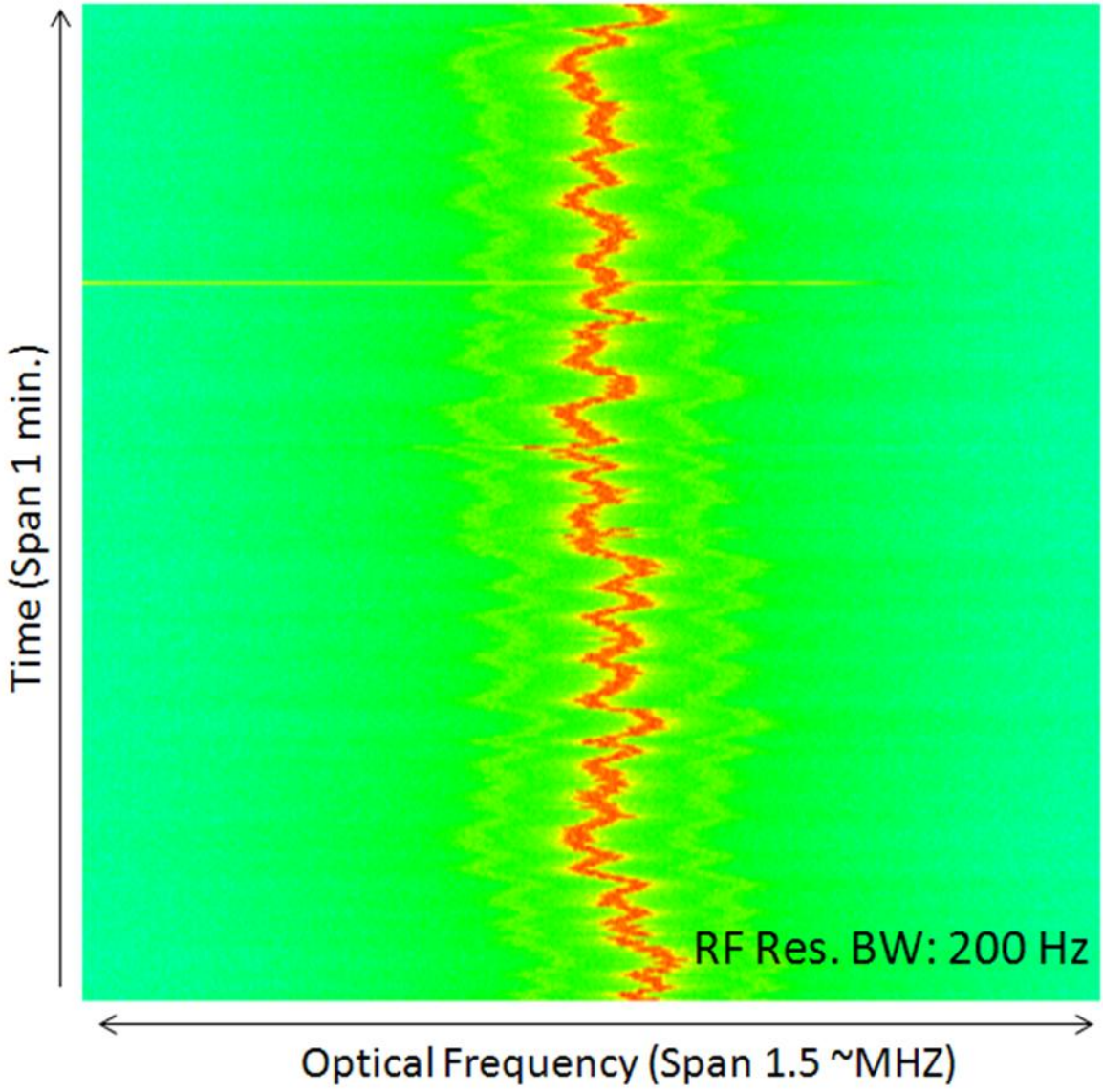

Figure 64: Optical frequency fluctuation measurement of the CW laser.

By using the conversion factor the maximum frequency deviation of the laser is measured (after warm up) with respect to the ultra-stable etalon, and found to be 198 kHz over a duration of 1 min, as shown in Fig. 64. The measurement range is limited to half of the resonance width of the etalon, i.e. 5 MHz. The 3 dB electrical bandwidth of the signal is measured as ~0.5 kHz which

corresponds to an optical frequency resolution of ~3.5 kHz after multiplying by the conversion factor. The update rate of the measurement was ~90 Hz, which corresponds to the 11 ms sweep time. The resolution and update rate are inversely proportional to each other.

Theoretical Analysis and Discussion

The range and the sensitivity of the system can be changed by using two variables: the finesse of the etalon and the length of the cavity. If a CW laser with large frequency instability is to be measured, a lower finesse etalon can be used to increase the measurement range. However, a lower finesse etalon will offer lower sensitivity. Fig. 65 and 66 show the dependency of measurement range and sensitivity to the finesse for a fixed cavity length.

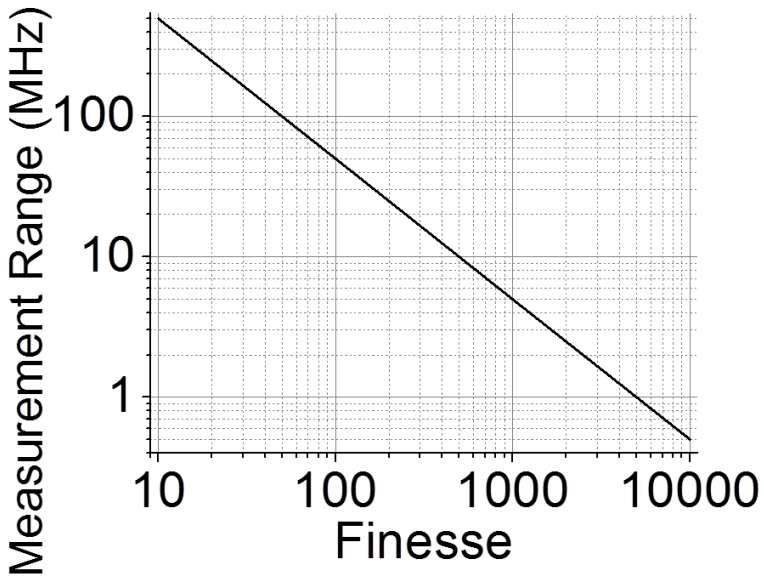

Figure 65: Measurement range vs. the Finesse of the etalon.

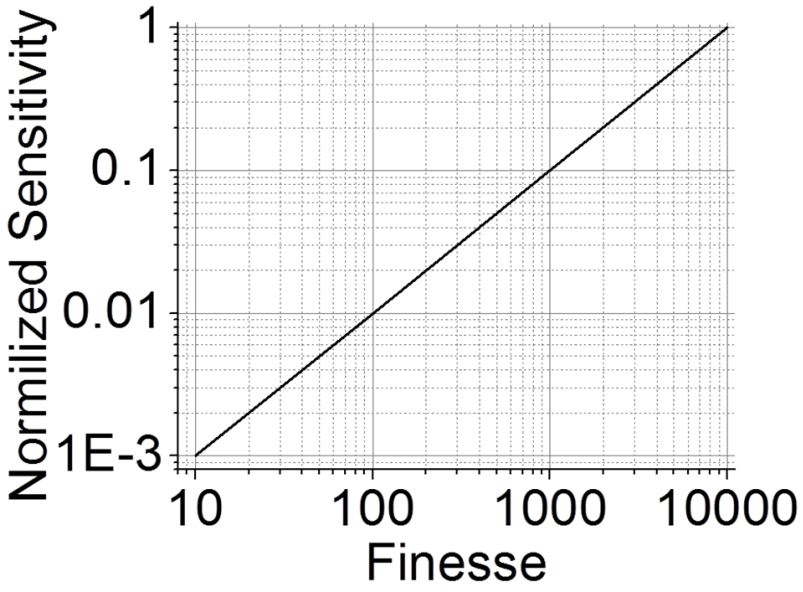

Figure 66: Measurement sensitivity with different Finesse values (for a fixed cavity length).

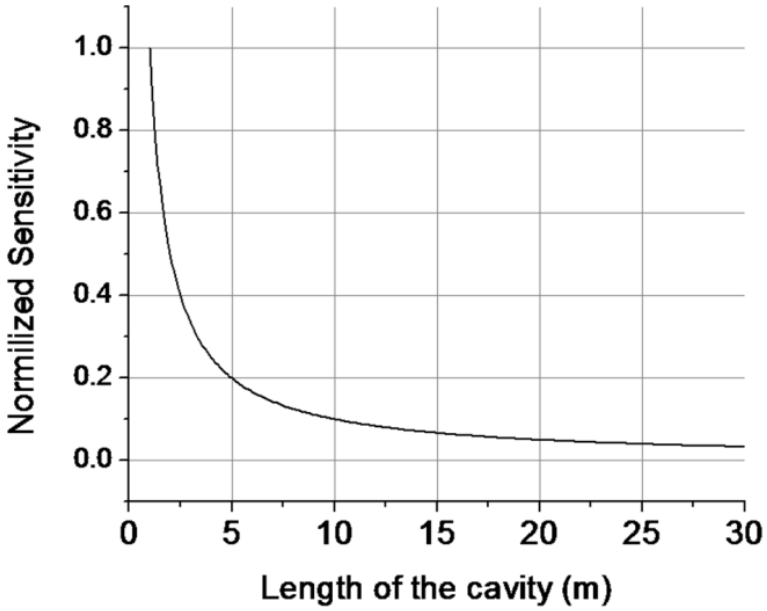

Figure 67: The change of sensitivity for different cavity lengths (fixed finesse). The sensitivity is normalized for a cavity length of 1m. Note that during the experiment the length of the cavity was ~10m.

Another method to increase the sensitivity of the measurement method is to decrease the total cavity length. For a fixed finesse, the dependency (or sensitivity) is inversely proportional to the cavity round trip time or cavity length (second part of Eq. 7). Fig. 67 shows how the sensitivity changes as the length of the cavity changes.

Conclusion

A novel technique for the measurement of the optical frequency stability of a CW laser is presented. The resonance transmission window of a 1000 finesse Fabry-Perot etalon is used as a reference, and is utilized for mapping the optical frequency fluctuations of a CW laser to the RF domain. This technique does not require an independent reference laser source and results in measurements with high resolution (~3.5 kHz) at fast update rates (90 Hz). Measurements performed on a stable CW laser revealed a maximum drift of 198 kHz over a duration of 1 min. The measurement range is limited to half of the resonance width of the etalon, and can be increased by using an etalon with lower finesse or higher FSR. The sensitivity of the new measurement method can be increased by a factor of 10 by simply making the cavity 10 times shorter (~ 1 m.). Moreover, by using an etalon with ultra-high finesse [66] the precision of the proposed method can be increased to sub-Hz level.

CHAPTER 8: CONCLUSION AND FUTURE WORK

In this work, the developments and novel methods for generating stable and narrow linewidth optical frequency combs and ultralow noise RF tone generation for photonic analog to digital conversion, coherent communication, arbitrary waveform generation and optical clock distribution are presented.

In my PhD research, first I have improved the precision of PDH based free spectral range measurement of a Fabry-Perot etalon by dynamically changing the static modulation and averaging electronically during data acquisition. The modified PDH based etalon free spectral range measurement resulted in 2 order of magnitude increase in the measurement precision which means 1 part in 10^6. The modified PDH based FSR measurement is used for building a 10 GHz mode-locked laser with 1000 finesse etalon. The MLL have a timing jitter integrated over 1Hz-100MHz is measured to be 3 fs, the extrapolated timing jitter up to Nyquist is only 14 fs. The integrated amplitude noise of the MLL over 1Hz-100MHz is 0.023%. Optical frequency fluctuations are less than 150 kHz and the optical comb linewidth is measured as < 1 kHz.

When the frequency noise of an etalon based mode-locked laser is measured referenced to the ULE etalon, a frequency noise of 10 Hz/√Hz at 10 Hz offset is obtained. In order to find out the absolute frequency noise of the MLL, the optical frequencies of two independent MLL are compared. Whereas both lasers has excellent frequency noise properties (~10 Hz/√Hz at 10 Hz offset) referenced to the etalons, the RF tone which results from the beating of two independent lasers has larger noise. This implies that the lasers are following the ULE etalons pretty well but the etalon resonance window frequencies are fluctuating slight due to the thermal noise and air pressure changes. In order to get rid of this problem a vacuumed and temperature stabilized

etalon should be incorporated with the system. Also an increase of the etalon finesse would results in a higher Q and hence to a narrower linewidth and lower noise.

Depending on the application, there can be tight restrictions on the weight and size of the mode-locked laser. To make the mode-locked laser much more smaller, compact and light weighted fiberized etalons can be used [67]. However, the Pound-Drever-Hall technique could not be applied to these lasers because of the polarization mode dispersion of the fiberized etalon.

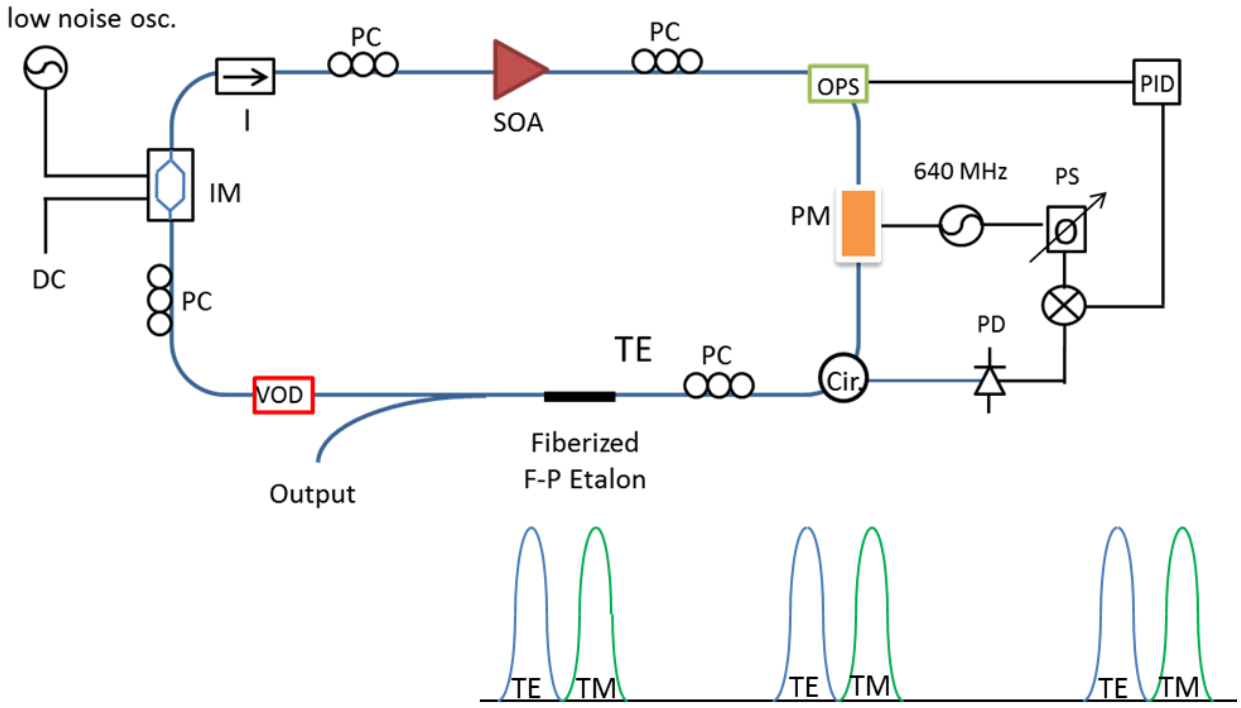

Figure 68: Setup for mode-locked laser with intracavity fiberized etalon with PDH locking. I: isolator, SOA: semiconductor optical amplifier, OPS: Optical phase shifter, PD: photodetectorPC: polarization controller, IM: intensity modulator, PID: PID controller, PM: phase modulator, Cir : optical circulator, OPS: Optical Phase Shifter, VOD: Variable Optical Delay

The polarization mode dispersion results in two different resonance windows with an offset frequency for two orthogonal polarization light state. If the standard PDH locking technique applies to the etalon which uses two orthogonal polarization states, the error signal will not be obtained and hence no locking will be achieved. To overcome this problem the PDH system is included inside the laser cavity which does not need two orthogonal polarization states. With the new method the intra-cavity phase modulator is used for obtaining the PDH error signal and the mode-locking is obtained by the loss modulation via an intensity modulator. The new method allows the PDH locking technique to be used with the fiberized etalons.

In this thesis, a novel method for low noise RF tone generation is introduced, which uses an etalon as the mode-selector instead of an RF filter. This method had advantages over the standard method such as higher stability, lower loss and narrower linewidth. One drawback of this method is the CW laser stability requirements. As the etalon resonance windows has a 10 MHz FWHM, the stability of the CW laser must be < 10 MHz. In order to solve this problem a PDH method can be added to the system as shown in Fig. 69.

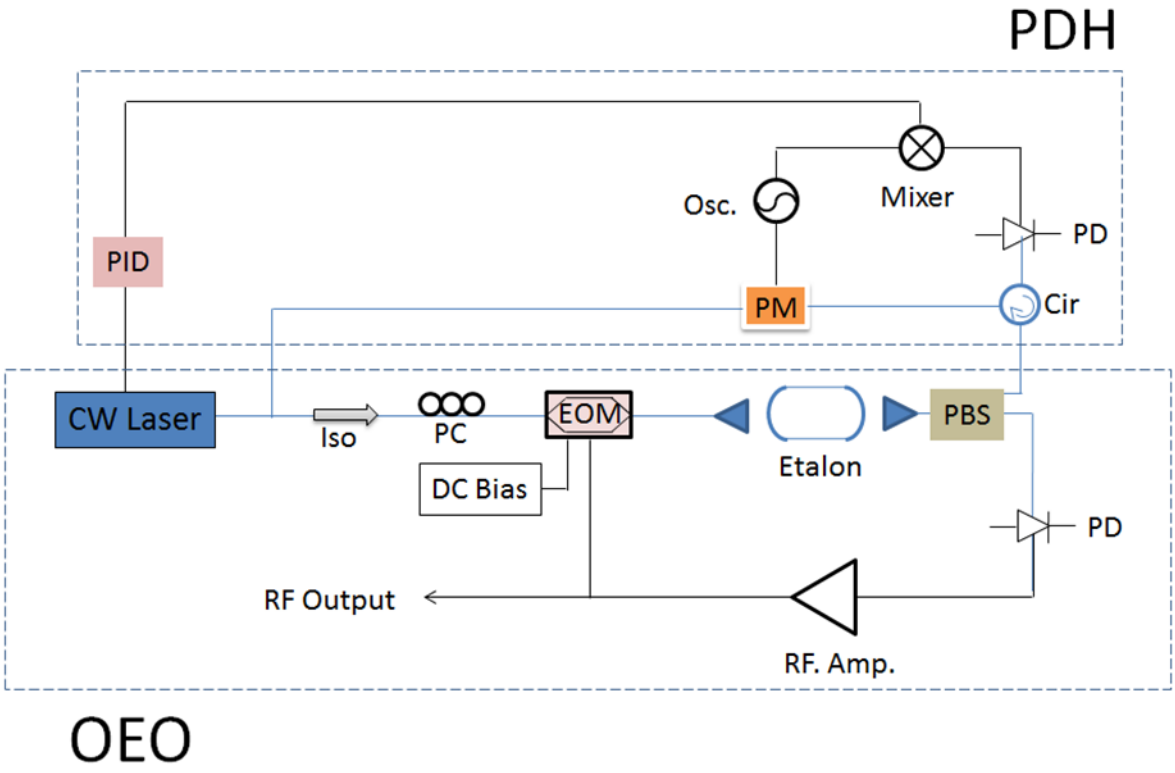

Figure 69: Opto-electronic oscillator scheme with PDH locking.

In this system, part of the CW light will be phase modulated and then sent back to the etalon from the back side via a polarization beam splitter. After reflecting from the etalon the beam will be directed to the PDH system without interfering with the OEO cavity. After photodetection and mixing with the local oscillator the error signal can be sent to the CW laser via a PID controller. This will lock the optical frequency to the etalon resonance window, and hence long term stability will be obtained.

APPENDIX A: MATLAB CODE FOR OPTICAL AND RF PHASE RELATION OF ETALON BASED OEO

```
clear;
n=1.5;                          % index of fiber
L=10;                           % length of optical delay in meters
c=3*10^8;                       % speed of light
nustart=192009000000;           % start frequency in kHz
nuspan=3000000;                 % 1 kHz
nuend=nustart+nuspan;           % finish frequency
r=0.9984429;                    % reflectiviy of the etalon mirrors
FSR=10000000;                   % FSR of the etalon

nu=linspace(nustart,nuend,nuspan);
spphase=pi*nu/FSR;
tr=(1-r^2)./(1-r^2*exp(1i.*2*spphase));
T=tr.*conj(tr);
ephase=imag(log(tr));
amplitude=real(tr);

RF1=zeros(1,nuspan);
RF2=zeros(1,nuspan);
RFT=zeros(1,nuspan);
```

```
RFphase1=zeros(1,nuspan);
RFamp1=zeros(1,nuspan);
RFphase2=zeros(1,nuspan);
RFamp2=zeros(1,nuspan);
RFphasetotal=zeros(1,nuspan);
RFpower=zeros(1,nuspan);
fmod1=zeros(1,nuspan);
fmod2=zeros(1,nuspan);
fmodd=zeros(1,nuspan);
fmodabs1=zeros(1,nuspan);
fmodabs2=zeros(1,nuspan);
deltaf1=zeros(1,nuspan);
deltaf2=zeros(1,nuspan);

detuning=4000;
deltaf(1999)=detuning;


%%%%%%%%%%%%%%%%%%%%%%%%%%%%%%%%
%%%%%%%%%%%%%%%%%%%%%%%%%%%%%%%%


N=2^20;
```

```
fc=100;
fm=0.01;
t=linspace(0,1000,N);
A1=exp(1i*2*pi*fc*t);
A2=exp(1i*2*pi*(fc+fm)*t+1i*0.9);
A3=exp(1i*2*pi*(fc+fm)*t-1i*0.9);
Arf1=cos(2*pi*fm*t+0.9);
Arf2=cos(2*pi*fm*t-0.9);
A=Arf1+Arf2;



for i=20000:1990000;
    RFphase1(i)=ephase(i)-ephase(i-detuning);
    RFamp1(i)=amplitude(i-detuning)*amplitude(i);
    RFphase2(i)=ephase(i+detuning)-ephase(i-detuning);
    RFamp2(i)=amplitude(i)*amplitude(i+detuning);
    RFphasetotal(i)=RFphase1(i)+RFphase2(i);
    RFpower(i)=cos((RFphase1(i)-RFphase2(i))/2);
     fmod1(i)=(RF(i)+1000*pi)*c/(L*index*2*pi)/1000;
     fmodabs(i)=round(fmod1(i));
     deltaf(i)=10000000-detuning-fmodabs(i);
end
```

```
subplot(3,2,1),plot(t,real(Arf1));
subplot(3,2,2),plot(t,real(Arf2));
subplot(3,2,3),plot(t,real(A));
subplot(3,2,4),plot(i,RFphase1);
subplot(3,2,5),plot(RFphase2);
subplot(3,2,6),plot(RFphasetotal/2);

figure(1);
plot(RFpower.^2)%;hold on; plot(RFphase2,'r'); hold on; plot(RFphasetotal/2,'black');
xlim([980000 1020000]);

figure(2);
plot(RFphase1); hold on; plot(RFphase2/2); %hold on; plot(RFphasetotal/2);
xlim([980000 1020000]);

%%%%%%%%%%%%%%%%%%%%%%%%%%%%%%%%%%%%
%%%%%%%%%%%%%%%%%%%%%%%%%%%%%%%%%%%%

for i=20000:1990000;
    RFT(i)=((ephase(i+deltaf1(i-1))-ephase(i))+(ephase(i)-ephase(i-deltaf1(i-1))))/2;
    fmod1(i)=(RFT(i)+1000*pi)*c/(L*index*2*pi)/1000;
    fmodabs1(i)=round(fmod1(i));
    deltaf1(i)=10000000+detuning-fmodabs1(i);
```

```
end

for i=20000:1990000;
    RF1(i)=(ephase(i+deltaf1(i-1))-ephase(i));%+(ephase(i)-ephase(i-deltaf1(i-1)))))/2;
    fmodd(i)=(RF1(i)+1000*pi)*c/(L*index*2*pi)/1000;
    fmodabs1(i)=round(fmodd(i));
    deltaf1(i)=10000000+detuning-fmodabs1(i);
end
%fmod1=fmod;

for i=20000:1990000;
    RF2(i)=ephase(i)-ephase(i-deltaf2(i-1));
    fmod2(i)=(RF2(i)+1000*pi)*c/(L*index*2*pi)/1000;
    fmodabs2(i)=round(fmod2(i));
    deltaf2(i)=10000000+detuning-fmodabs2(i);
end
RFpower=(cos(((RF1-RF2))/2)).^2;

%%%%%%%%%%%%%%%%%%%%%%%%%%%%%%%%%%%%%%
%%%%%%%%%%%%%%%%%%%%%%%%%%%%%%%%%%%%%%

figure(1);
plot(fmod1);
```

```
xlim([970000 1030000]);


plot(fmod)
tt=linspace((-nuspan/2),(nuspan/2),2^n);


figure(1);
plot(fmod1);%hold on; plot(RF2,'r'); hold on; plot((RF1+RF2)/2,'black');
xlim([980000 1020000]);


figure(2);
subplot(3,1,1),plot(RF1);
xlim([980000 1020000]);
subplot(3,1,2),plot(RF2);
xlim([980000 1020000]);
subplot(3,1,3),plot(fmod1);
xlim([980000 1020000]);
```

REFERENCES

[1] A. S. Bhushan, F. Coppinger, and B. Jalali, “Time-stretched analog to-digital conversion,” *IEE Electronics Letters*, vol. 34, no. 9, pp. 839-840, 1998

[2] J. A. Bell, M. C. Hamilton, D. A. Leep, T. D. Moran, H. F. Taylor, and Y. H. Lee, "Extension of electronic A/D converters to multi-gigahertz sampling rates using optical sampling and demultiplexing techniques," *Signals, Systems and Computers, 1989. Twenty-Third Asilomar Conference on*, vol.1, pp. 289- 293, 1989.

[3] A. Leven, Y. Yang, R. Kopf, A. Tate, T. C. Hu, J. Frackoviak, R. Reyes, N. G. Weimann, Y.K. Chen, R. DeSalvo, G. Burdge, G. Deibner, F. Quinlan, S.Gee, P. Delfyett, “High Sped Arbitrary Waveform Generation and Processing using a Photonic Digital-to-Analog Converter,” *LEOS Summer Topicals Meeting 2007*, paper TuC2.1

[4] T. Yilmaz, C. M. DePriest, T. Turpin, J.H. Abeles, P.J. Delfyett, “Toward a photonic arbitrary waveform generator using a modelocked external cavity semiconductor laser” *Photonics Technology Letters, IEEE*, vol. 14, no. 11, pp. 1608- 1610, 2002

[5] P. J. Delfyett, S. Gee, M. Choi, H. Izadpanah, W. Lee, S. Ozharar, F. Quinlan, T. Yilmaz “Optical Frequency Combs from Semiconductor Lasers and Applications in Ultra-wideband Signal Processing and Communications,” *Lightwave Technology, Journal of*, 7, 2701-2719, 2006

[6] R. Wu, V. R. Supradeepa, C. M. Long, D. E. Leaird, and A. M. Weiner, "Generation of very flat optical frequency combs from continuous-wave lasers using cascaded intensity and

phase modulators driven by tailored radio frequency waveforms," Opt. Lett. **35**, 3234-3236 (2010)

[7] S. Ozharar, F. Quinlan, I. Ozdur, S. Gee, and P. J. Delfyett, "Ultraflat Optical Comb Generation by Phase-Only", *Photonics Technology Letters, IEEE* vol. 20, no. 1, 2008

[8] P. Del'Haye, A. Schliesser, O. Arcizet, T. Wilken, R. Holzwarth & T. J. Kippenberg, "Optical frequency comb generation from a monolithic microresonator", *Nature* **450**, 1214-1217, December 2007

[9] S. T. Cundiff, & J. Ye, "Colloquium: Femtosecond optical frequency combs.", *Rev. Mod. Phys.* **75**, 325–342 (2003)

[10] T. Udem, R. Holzwarth, & T. W. Hänsch, "Optical frequency metrology.", *Nature* **416**, 233–237 (2002)

[11] M. T. Murphy, Th. Udem, R. Holzwarth, A. Sizmann, L. Pasquini, C. Araujo-Hauck, H. Dekker, S. D'Odorico, M. Fischer, T. W. Hänsch, A. Manescau, "High-precision wavelength calibration of astronomical spectrographs with laser frequency combs," *Mon. Not. R. Astron. Soc*., **380,** 839-847, 2007

[12] S. T. Cundiff, "Phase stabilization of ultrashort optical pulses," *J. Phys. D.*, vol. 35, pp. R43–R59, 2002

[13] S. Gee, F. Quinlan, S. Ozharar, P. J. Delfyett, "Simultaneous Optical Comb Frequency Stabilization and Super-Mode Noise Suppression of Harmonically Mode-Locked Semiconductor Ring Laser Using an Intracavity Etalon," *Photonics Technology Letters, IEEE,* vol.17, no.1, pp.199-201, Jan. 2005

[14] T. Yilmaz, C. M. Depriest, A. Braun, J. Abeles, P. J. Delfyett, "Noise in Fundamental and Harmonic Modelocked Semiconductor Lasers: Experiments and Simulations," *Quantum Electronics, IEEE Journal of,* vol.39, no.7, pp. 838- 849, July 2003

[15] C. Williams, F. Quinlan, and P. J. Delfyett, " Injection-Locked Mode-Locked Laser With Long-Term Stabilization and High Power-per-Combline" *Photonics Technology Letters, IEEE,* vol. 21, no. 2, pp.94-96, Jan.15, 2009

[16] F. Quinlan, G. Sangyoun, S. Ozharar, P.J. Delfyett, "Frequency Stabilized Low Timing Jitter Mode-Locked Laser with an Intracavity Etalon", *Conference on Lasers and Electro-Optics, CLEO 2007,* CThHH6

[17] F. Quinlan, G. Sangyoun, S. Ozharar, P.J. Delfyett, "Semiconductor based, high repetition rate mode-locked lasers for time and frequency based coherent communications and signal processing applications", *Proc. of SPIE* Vol. 6572 (2007)

[18] D. von der Linde, "Characterization of the noise in continuously operating modelocked lasers," *Appl. Phys. B,* **39**, 201-217, 1986

[19] F. Quinlan, S. Gee, S. Ozharar, P. J. Delfyett, "Ultralow-jitter and –amplitude noise semiconductor-based modelocked laser," *Opt. Lett.,* **31**, 2870-2872, 2006

[20] Jager, H., Musso, M., Neureiter, C., and Windholz, L.: 'Optical measurement of the free spectral range and spacing of plane and confocal Fabry-Perot interferometers', *Opt. Eng.,* 1990, 29, (1), pp. 42–46

[21] Kinght, P.D., Cruz-Cabrera, A., and Bergner, B.C.: 'High-resolution measurement of the free spectral range of an etalon', *Proc. SPIE, 2002,* 4772, pp. 114–117

[22] Williamson, R., and Terpstra, C.: 'Precise free spectral range measurement of telecom etalon', *Proc. SPIE, 2003*, 5180, pp. 274–282

[23] Drever, R.W.P., Hall, J.L., Kowalski, F.V., Hough, J., Ford, G.M., Munley, A.J., and Ward, H.: 'Laser phase and frequency stabilization using an optical resonator', *Appl. Phys. B*, 1983, 31, (2), pp. 97–105

[24] Gee, S., Ozharar, S., Quinlan F., and Delfyett, P. J.: 'High-precision measurement of free spectral range of etalon', *IEE Electronics Letters*, vol. 42, no. 12 June 2006

[25] P. J. Delfyett, S. Gee, M. Choi, H. Izadpanah, W. Lee, S. Ozharar, F. Quinlan, T. Yilmaz "Optical Frequency Combs from Semiconductor Lasers and Applications in Ultra-wideband Signal Processing and Communications," *Lightwave Technology, Journal of*, 7, 2701-2719, (2006)

[26] X. Yao and L. Maleki, "Dual microwave and optical oscillator," *Opt.Lett.*, vol. 22, no. 24, pp. 1867–1869, 1997.

[27] T. Yilmaz, C.M. DePriest CM, Delfyett PJ, "Complete noise characterisation of external cavity semiconductor laser hybridly modelocked at 10 GHz", *IEE Electronics Letters*, vol. 37, no.22, pp. 1338-1339, Oct. 2001.

[28] S. Gee, F. Quinlan, S. Ozharar, and P. J. Delfyett, "Simultaneous optical comb frequency stabilization and super mode noise suppression of harmonically modelocked semiconductor ring laser using an intracavity etalon", *Photonics Technology Letters, IEEE*, vol. 17, no. 1, (2005)

[29] F. Quinlan, S. Gee, S. Ozharar, P. J. Delfyett," Frequency Stabilized Low Timing Jitter Mode-Locked Laser with an Intracavity Etalon" *Conference on Lasers and Electro-Optics, CLEO 2007*, CThHH6.

[30] K. Kim, S. Lee, and P. J. Delfyett, "eXtreme Chirped Pulse Amplification—Beyond the Fundamental Energy Storage Limit of Semiconductor Optical Amplifiers", *IEEE J. Sel. Topics Quantum Electronics*, vol. 12, no. 2, pp 245-254, (2006).

[31] S. Sartania, Z. Cheng, M. Lenzner, G. Tempea, Ch. Spielmann, and F. Krausz, " Generation of 0.1-TW 5-fs optical pulses at a 1-kHz repetition rate", *Opt. Lett.*, **22**, no. 20 October 15, 1997

[32] K. Kyungbum, L. Shinwook and P. J. Delfyett, "1.4kW high peak power generation from an all semiconductor mode-locked master oscillator power amplifier system based on eXtreme Chirped Pulse Amplification(X-CPA)", *Optics Express*, vol. 13, issue 12, pp. 4600-4606

[33] S. Kawanishi,"Ultrahigh-Speed Optical Time-Division-Multiplexed Transmission Technology Based on Optical Signal Processing", *Quantum Electronics, IEEE Journal of,* vol. 34, no. 11, 1998

[34] M. Nakazawa, H. Kubota, K. Suzuki, E. Yamada, and A. Sahara," Ultrahigh-Speed Long-Distance TDM and WDM Soliton Transmission Technologies", *IEEE Journal of Selected Topics in Quantum Electronics,* vol. 6, no. 2, 2000

[35] T. G. Ulmer, M. C. Gross, K. M. Patel, J. T. Simmons, P. W. Juodawlkis, B. R. Washburn, W. S. Astar, A. J. SpringThorpe, R. P. Kenan, C. M. Verber, and S. E. Ralph, "160-Gb/s Optically Time-Division Multiplexed Link with All-Optical Demultiplexing", *Lightwave Technology, Journal of,* vol. 18, no. 12, Dec. 2000

[36] T. Kawanishi, T. Sakamoto, M. Tsuchiya, M. Izutsu, S. Mori and K. Higuma, "70dB extinction-ratio LiNbO3 optical intensitymodulator for two-tone lightwave generation", *OFC* pp-3, 5-10 March 2006

[37] K. Taira, Y. Fukuchi, R. Ohta, K. Katoh and K. Kikuchi, “Background-free intensity autocorrelator employing Si avalanche photodiode as two-photon absorber”, *IEE Electronics Letters*, 38, 1465-1466 (2002)

[38] T. Kawanishi, S. Sakamoto and M. Izutsu, “High-Speed Control of Lightwave Amplitude, Phase, and Frequency by Use of Electrooptic Effect” (Invited Paper), *IEEE Journal of Selected Topics in Quantum Electronics,* 13, 79-91 (2007), Section III.B

[39] J.-P. Ruske, E.A. Werner, B. Zeitner and A. Tünnermann, “Integrated optical ultrashort-pulse picker with high extinction ratio”, *IEE Electronics Letters,* 20, 1442- 1443 (2003).

[40] T. Yilmaz, C. M. DePriest, A. Braun, J. Abeles, P.J. Delfyett, “Noise in fundamental and harmonic modelocked semiconductor lasers: experiments and simulations*”, Quantum Electronics, IEEE Journal of,* vol.39, no.7, pp. 838- 849, July 2003

[41] F. Rana, H. L. T. Lee, R. J. Ram, M. E. Grein, L. A. Jiang, E. P. Ippen, and H. A. Haus, "Characterization of the noise and correlations in harmonically mode-locked lasers," *J. Opt. Soc. Am. B* 19, 2609-2621 (2002)

[42] A. Neyer and E. Voges, “High-frequency electro-optic oscillator using an integrated interferometer,” *Appl. Phys. Lett.*, vol. 40, pp. 6–8, 1982.

[43] M. F. Lewis, “Novel RF oscillator using optical components,” *IEE Electronics Letters,* vol. 28, pp. 31–32, 1992.

[44] X. S.Yao and L. Maleki, “Optoelectronic microwave oscillator,” *J. Opt.Soc. Amer. B,* vol. 13, no. 8, pp. 1725–1735, Aug. 1996.

[45] E. Salik, N. Yu, and L. Maleki, “An ultralow phase noise coupled optoelectronic oscillator,” *Photonics Technology Letters, IEEE,* vol. 19, no. 6, pp. 444–446, Mar. 2007.

[46] T. Davidson, P. Goldgeier, G. Eisenstein, and M. Orenstein, "High spectral purity CW oscillation and pulse generation in optoelectronic microwave oscillator," *IEE Electronics Letters*, vol. 35, no. 15, pp. 1260–1261, Jul. 1999.

[47] X. S. Yao and L. Maleki, "Multiloop optoelectronic oscillator," *Quantum Electronics, IEEE Journal of,* vol. 36, no. 1, pp. 79–84, Jan. 2000.

[48] E. Shumakher and G. Eisenstein, "A novel multiloop optoelectronic oscillator," *Photonics Technology Letters, IEEE,* vol. 20, no. 22, pp. 1881–1883, Nov. 2008.

[49] D. H. Chang, H. R. Fetterman, H. Erlig, H. Zhang, M. C. Oh, C. Zhang, and W. H. Steier, "39-GHz Optoelectronic Oscillator Using Broad-Band Polymer Electrooptic Modulator", *Photonics Technology Letters, IEEE,* vol. 14, no. 2, February 2002

[50] J. Lasri, P. Devgan, R. Tang, and P. Kumar," Self-starting optoelectronic oscillator for generating ultra-low-jitter high-rate (10GHz or higher) optical pulses", *Optics Express,* vol. 11, issue 12, pp. 1430-1435, June 2003.

[51] J. Yang, Y. Jin-Long, W. Yao-Tian, Z. Li-Tai, and Y. En-Ze, "An optical domain combined dual-loop optoelectronic oscillator," *Photonics Technology Letters, IEEE*, vol. 19, no. 11, pp. 807–809, Jun. 2007.

[52] D. Strekalov, D. Aveline, Y. Nan, R. Thompson, A. B. Matsko, and L. Maleki, "Stabilizing an optoelectronic microwave oscillator with photonic filters," *Lightwave Technology, Journal of,* vol. 21, no. 12, pp. 3052–3061, Dec. 2003.

[53] X. S. Yao, L. Davis, and L. Maleki, "Coupled optoelectronic oscillators for generating both RF signal and optical pulses," *Lightwave Technology, Journal of,* vol. 18, no. 1, pp. 73–78, Jan. 2000.

[54] F. Quinlan, S. Ozharar, S. Gee, and P. J. Delfyett," Harmonically mode-locked semiconductor-based lasers as high repetition rate ultralow noise pulse train and optical frequency comb sources", *J. Opt. A: Pure Appl. Opt.* **11,** 103001, August 2009

[55] M. Y. Frankel and R. D. Esman, "Optical Single-Sideband Suppressed-Carrier" *Lightwave Technology, Journal of*, vol. 16, no. 5, May 1998

[56] I. Ozdur, M. Akbulut, N. Hoghooghi, D. Mandridis, S. Ozharar, F. Quinlan, P. J. Delfyett, "A Semiconductor-Based 10-GHz Optical Comb Source With Sub 3-fs Shot-Noise-Limited Timing Jitter and ~500-Hz Comb Linewidth," *Photonics Technology Letters, IEEE* , vol.22, no.**6**, pp.431-433, March15, 2010

[57] K. L. Corwin, Z.-T. Lu, C. F. Hand, R. J. Epstein, and C. E. Wieman, "Frequency-stabilized diode laser with the Zeeman shift in an atomic vapor" *Applied Optics*, vol. 37, issue **15**, pp. 3295-3298, 1998

[58] D. J. Jones, S. A. Diddams, J. K. Ranka, A. Stentz, R. S. Windeler, J. L. Hall, S. T. Cundiff, "Carrier-Envelope Phase Control of Femtosecond Mode-Locked Lasers and Direct Optical Frequency Synthesis", *Science*, vol. 288. no. **5466**, pp. 635 – 639, 2000

[59] X. S. Yao and L. Maleki, "Optoelectronic microwave oscillator," *J. Opt.Soc. Amer. B*, vol. 13, no. **8**, pp. 1725–1735, 1996.

[60] E. Salik, N.Yu, and L.Maleki, "An ultralow phase noise coupled optoelectronic oscillator," *IEEE Photon. Technol. Lett.*, vol. 19, no**. 6**, pp. 444–446, Mar. 2007.

[61] T. Davidson, P. Goldgeier, G. Eisenstein, and M. Orenstein, "High spectral purity CW oscillation and pulse generation in optoelectronic microwave oscillator," *IEE Electron. Lett.*, vol. 35, no. **15**, pp. 1260–1261, July, 1999.

[62] J. Lasri, P. Devgan, R. Tang, and P. Kumar," Self-starting optoelectronic oscillator for generating ultra-low-jitter high-rate (10GHz or higher) optical pulses", Optics Express, Vol. 11, Issue **12**, pp. 1430-1435, June 2003.

[63] E. Shumakher and G. Eisenstein, "A novel multiloop optoelectronic oscillator," *IEEE Photon. Technol. Lett.*, vol. 20, no. **22**, pp. 1881–1883, Nov. 2008.

[64] L. D. Nguyen, K. Nakatani, B. Journet, "Refractive Index Measurement by Using an Optoelectronic Oscillator," *Photonics Technology Letters, IEEE*, vol.22, no.**12**, pp.857-859, June15, 2010

[65] I. Ozdur , M. Akbulut, N. Hoghooghi, D. Mandridis, M. U. Piracha, and P. J. Delfyett."Optoelectronic loop design with 1000 finesse Fabry–Perot etalon" *Optics Letters.* vol. 35, issue **6**, pp. 799–801 (2010)

[66] J. Alnis, A. Matveev, N. Kolachevsky, Th. Udem , and T. W. Hänsch. "Subhertz linewidth diode lasers by stabilization to vibrationally and thermally compensated ultralow-expansion glass Fabry-Pérot cavities" *Phys. Rev.* A **77**, 053809 (2008)

[67] J.E. Malowicki, et al., "Harmonically Mode-locked Glass Waveguide Laser with 21-fs Timing Jitter.", Photonics Technology Letters, IEEE, vol.17, no. 1, 2005